Strategies to modulate selectivity and improve stability in methanol to hydrocarbons catalysis over zeolites or zeotypes and their mechanistic origins

A DISSERTATION
SUBMITTED TO THE FACULTY OF THE
UNIVERSITY OF MINNESOTA
BY

Sukaran Singh Arora

IN PARTIAL FULFILLMENT OF THE REQUIREMENTS
FOR THE DEGREE OF
DOCTOR OF PHILOSOPHY

Advised by Professor Aditya Bhan

August 2019

Acknowledgements

I gratefully acknowledge my advisor, Prof. Aditya Bhan, who has been a constant source of inspiration, guidance and motivation due to his expertise in the field and strong work ethic. I thank all the present and past members of the Bhan group that I have interacted with over the duration of my study for their help and support both in and outside the lab; I especially acknowledge Zhichen Shi, whom I had the opportunity of collaborating with during my work, for her constant assistance and engagement in technical discussions. I thank my collaborators from Dow, Dr. Andrzej Malek, Dr. Davy Nieskens and Dr. Joseph DeWilde, for their technical insights throughout my work. I also thank Thomas Chen, Robert DeJaco, Truong Pham, and Matthew Quan for their close friendship; I especially acknowledge Thomas Chen for helping me acclimate to the new culture and for his invaluable participation in activities outside of the lab. Finally, I am very grateful to my parents, Prof. Parmjit Singh Arora and Mrs. Surjit Kaur Arora, and my siblings, Sargun Kaur Kohli and Taruntej Singh Arora, for the constant encouragement, emotional and moral support.

Abstract

The catalytic conversion of methanol-to-hydrocarbons (MTH) over Brønsted acid zeolites/zeotypes is now used to derive an increasing fraction of the annual 250 million metric tons production of light olefins, ethene and propene—feedstocks in plastics, pharmaceuticals, and chemicals manufacturing. Controlling the relative formation rates of ethene and propene, and mitigating deactivation rates of zeolites that necessitates energy-intensive regeneration cycles to restore catalytic activity are the two critical outstanding challenges. This work demonstrates the hitherto unknown role of trace quantities of aldehydes in distinct chemical events that dictate the selectivity ratio of ethene and propene, and the extent of catalyst deactivation during MTH. Specifically, it is shown that formaldehyde, formed in trace quantities by the loss of hydrogen from methanol, facilitates the propagation of reactions that promote ethene production, while simultaneously accelerating rates of chemical transformations that induce catalyst deactivation. This mechanistic understanding is exploited to demonstrate that in MTH, i) the selectivity ratio of propene-to-ethene can be notably varied ($1-25$ range) by controlling the inlet methanol pressure which directly affects formaldehyde production and consequently its involvement in reactions that produce ethene, and ii) catalyst lifetime can be considerably enhanced ($>70\times$) by co-processing high-pressure H_2 which results in the interception of formaldehyde-mediated condensation pathways deleterious to catalyst lifetime by selective hydrogenation of the unsaturated intermediates formed in these reactions.

Contents

List of Figures

List of Tables

List of Schemes

Chapter 1

Introduction to methanol to hydrocarbons catalysis on solid Brønsted acids

Methanol-to-hydrocarbons (MTH) process over zeolite and zeotype materials is the final step in upgrading gasifiable carbon-based feedstocks, such as coal, biomass and natural gas to light olefins ($C_2 - C_4$) and gasoline-range hydrocarbons (C_{4+} aliphatics and aromatics), and represents an alternative to their conventional production from oil-based processes [1, 2]. MTH over HSAPO-34 is now commercially deployed in China to produce ethene and propene with annual production capacity of ∼1 million metric tons [3], which has brought renewed interest in the mechanistic understanding of molecular events that govern selectivity and deactivation in MTH with the goal of rational process and material design to achieve selective and stable conversion of methanol to target hydrocarbons.

Zeolites are porous, crystalline silicoaluminate materials that are comprised of interconnected neutral SiO_4 and anionic AlO_4 tetrahedra assembled in a framework of cages and channels in three dimensions with pore openings on the order of a few angstroms [4]. Zeotypes, on the other hand, contain elements other than Si or Al in the tetrahedral framework sites, for instance, silicoaluminophosphates consist of P in addition to Si and Al, and thus primarily differ from their isostructural zeolite analogs in their chemical composition [5]. Brønsted acidity originates from the charge balancing protons localized on the bridging O atoms connecting neighboring Si and Al atoms, however, other metal cations can also be incorporated as charge-balancing counter ions which engenders Lewis acidity in these materials [4]. The versatility in the nature of counter-ions and the unique structural features—comprised of channels with varying connectivity that engender different confining environments and apertures of molecular dimensions that enable shape selectivity—are the two prolific characteristics that make these materials relevant for applications in the fields of separations and catalysis [4, 6–9]. The identity and distribution of hydrocarbons in MTH is largely determined by the topological features of the Brønsted acid zeolite or zeotype materials [10–19]. The small-pore zeolites/zeotypes characterized by 8-membered ring apertures on the order of ∼4 Å, such as HSSZ-13 and HSAPO-34, engender high selectivity of light hydrocarbons (>85 %C) due to size-exclusion of larger hydrocarbons that cannot

effuse through the narrow pore openings, while medium- and large-pore zeolites characterized by 10- and 12-membered ring apertures on the order of >5 Å, such as HZSM-5 and HBEA, allow effusion of the larger C_{4+} hydrocarbons. These innate differences in product composition depending on the zeolite topology, however, share the same mechanistic origins as detailed next.

Both experimental [20] and theoretical [21, 22] investigations have concluded that in the absence of a primordial hydrocarbon pool entrained in the zeolite pores, the C_1 species derived from methanol upon interaction with the Brønsted acid sites in zeolites are relatively inert towards hydrocarbon formation due to the high energy barriers (>200 kJ/mol) for direct C–C coupling. The hydrocarbon pool, which is comprised of both olefinic and aromatic species, likely originates from reactions of methanol with adventitious impurities in the influent gas stream or in the catalyst bed [23–27]. Following this initiation, product formation occurs in an autocatalytic manner wherein the hydrocarbon pool components act as co-catalytic centers for repeated methylation and cracking steps to produce a range of C_{2+} hydrocarbons [24, 28–30]. The dual—olefinic and aromatic—nature of the hydrocarbon pool has been validated by several researchers by isotopic labeling and cofeed studies [31–36]. This indirect mechanism of hydrocarbons production can be succinctly represented by a dual cycle schematic wherein the reactions of methylation and β-scission involving olefinic co-catalysts are referred as the *olefins cycle* while reactions of methylation and dealkylation involving aromatic co-catalysts are referred as the *aromatics cycle* (Scheme 1.1) [26, 37, 38]. The two cycles are interconnected by hydrogen transfer and cyclization steps that mediate the conversion of olefins to aromatics while resulting in the concomitant production of paraffins (Scheme 1.1). The propagation of the olefinic cycle predominantly results in the formation of C_3-C_{7+} aliphatics while the aromatic cycle primarily yields methyl-substituted benzenes and C_2-C_3 olefins. In particular, the mechanistic origin of ethene from the aromatics cycle via dealkylation has been evinced in isotopic labeling studies wherein the amount of ^{13}C incorporation in ethene and methyl-substituted benzenes is observed to be similar and distinct from that of C_{3+} olefins following the switch from ^{12}C-labeled methanol to its ^{13}C-labeled counterpart [39, 40]. In context of the hydrocarbon pool mechanism, the different product composition observed during methanol conversion can be rationalized as a consequence of the relative propagation extents of the olefinic and aromatic cycles, which is strongly influenced by the topological features of the zeolites/zeotypes. The large cages interconnected by small windows in small-pore zeolites compel the preferential propagation of the aromatics cycle while only permitting the effusion of light hydrocarbons (C_2-C_4) while the cavities and larger channels in medium- and large-pore zeolites allow the simultaneous propagation of the olefins and aromatics cycle, and permit the effusion of larger C_{4+} aliphatics and aromatics. In addition to the effect of zeolite topology, selectivity in MTH is also sensitively determined by the operating conditions (temperature [41], methanol pressure [42], space velocity [43]), identity of cofeeds (water [44], oxygenates

[45, 46], hydrocarbons [33, 34]), and zeolite properties (crystallite size [18, 47, 48], acid site density [49] and distribution [50, 51], presence of mesoporosity [52, 53], surface silylation [54], phosphorous modification [55]). All observed effects on selectivity can be visualized in context of the relative propagation extents of the olefinic and aromatic cycles as influenced by changes in the aforementioned operating and material parameters.

With reaction progress, however, the ability of active sites to turn over for hydrocarbons production from methanol declines due to the transformation of active hydrocarbon pool components to inactive polycyclics which accumulate inside the zeolite channel system [26, 27, 37]. Chromatographic analyses of the organics liberated from zeolites after methanol conversion, via dissolution of the zeolite framework with HCl/HF followed by extraction with CH_2Cl_2 [56], reveal that phenanthrenes and pyrenes are the main polycyclics entrained in the zeolites at complete deactivation [57–59]. Emerging research suggests that formaldehyde, formed from transfer dehydrogenation events involving methanol, facilitates these undesired transformations via involvement in electrophilic addition reactions with olefins and aromatics generating unsaturated intermediates which can further undergo a series of hydrogen transfer and cyclization steps to generate polycyclics [43, 60–63].

This dissertation focuses on the mechanistic elucidation of the role played by aldehydes in dictating selectivity and catalyst lifetime in MTH, and proffers strategies to regulate the extent of their formation and involvement in alkylation pathways during MTH that demonstratively enable selectivity control to target hydrocarbons (light olefins and aromatics) and elongate catalyst lifetime. Chapter 2 describes the prolific role of methanol pressure in dictating the relative amounts of ethene and propene production during MTH over HZSM-5, which stems from the direct effect of methanol pressure on the formation of formaldehyde that mediates the transformation of olefins to aromatics and in turn, influences the relative propagation of the olefins and aromatics cycles. Chapter 3 describes the promotional effect of high-pressure CO cofeeds on aromatics production during MTH over HZSM-5, and elucidates the prominent role of acetyls derived from co-reaction of CO and methanol-derived surface species as key intermediates that can generate aldehydes and ketones. These carbonyl compounds can undergo a network of aldol condensation, hydrogen transfer, cyclization, dehydration, and decarbonylation steps to promote aromatics production without the sacrificial formation of alkanes, as is the case in the conventional pathway for their production from olefins. Chapter 4 describes the beneficial effects of high-pressure H_2 cofeeds on catalyst lifetime during MTH over HSAPO-34 without compromise of the high light olefins selectivity characteristic of this small-pore zeotype. The observed effects of H_2 cofeeds are rationalized in context of the ability of acidic protons to facilitate direct hydrogenation of the unsaturated intermediates resulting from formaldehyde-mediated alkylation pathways with olefins and aromatics, thereby intercepting their transformation to polycyclics and resulting in longer catalyst lifetimes. Chapter 5 describes the effects of

cofeeding H_2 on lifetime and selectivity in MTH over several zeolites other than HSAPO-34 (small-pore HSSZ-13 and HSSZ-39, medium-pore HFER, and large-pore HBEA), demonstrating the general applicability of the strategy of high-pressure H_2 cofeeds to improve catalyst stability. The aforementioned proposal concerning the facile hydrogenation of unsaturated intermediates originating from formaldehyde-mediated alkylation of olefins and aromatics via direct hydrogen transfer from H_2 is corroborated by kinetic measurements of aliphatics and aromatics hydrogenation with H_2 over zeolites discussed in Chapters 5 and 6, respectively.

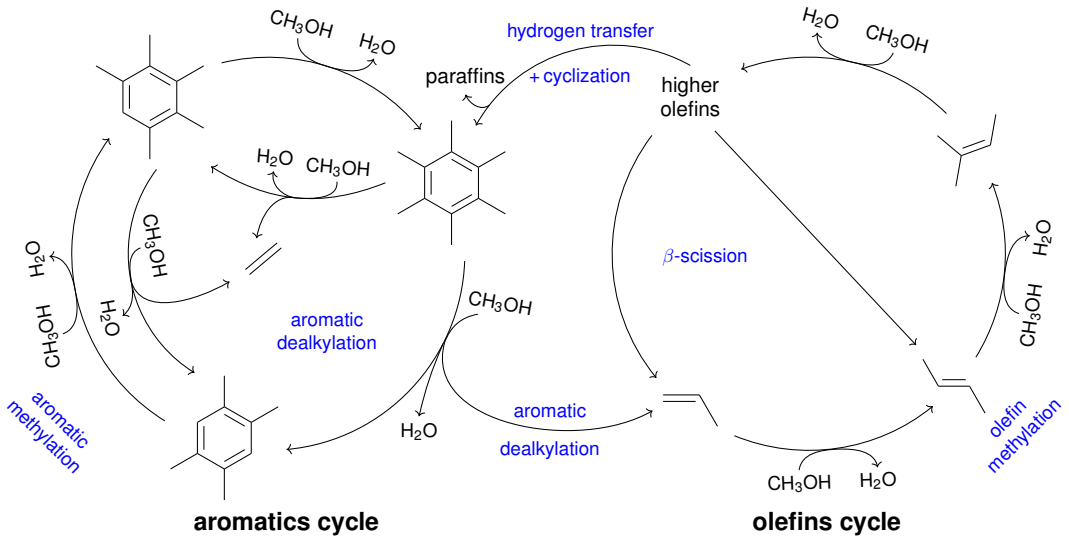

Scheme 1.1: Schematic illustrating the dual cycle description of the hydrocarbon pool mechanism that dictates hydrocarbon formation during methanol conversion over zeolites/zeotypes. Adapted from [38].

Chapter 2

The critical role of methanol pressure in controlling its transfer dehydrogenation and the corresponding effect on propene to ethene ratio during methanol to hydrocarbons catalysis on HZSM-5

*Reported from S. S. Arora, A. Bhan, *J. Catal.* 356 (2017) 300-306
(doi.org/10.1016/j.jcat.2017.10.014)

2.1 Abstract

A monotonic increase (2 – 18) in the effluent propene-to-ethene molar ratio as inlet methanol pressure is varied from 52.5 – 0.6 kPa during methanol-to-hydrocarbons catalysis (∼30 %C conversion) on HZSM-5 at 673 K reveals methanol pressure as a salient experimental parameter that allows control over the relative rates of propagation of the olefins- and aromatics-based methylation/cracking events. The effect of enhanced propagation of the olefins-based cycle over its aromatics-based counterpart and consequently, decoupling of the two catalytic cycles at low influent methanol pressures is observed to persist irrespective of the reaction temperature (623 – 773 K). Reactions involving formaldehyde cofeeds (3 – 20 Pa or 0.5 – 5 %C) with low-pressure (0.6 kPa) methanol at 623 K result in a monotonically decreasing trend in propene-to-ethene molar ratio from 24.7 in the absence of formaldehyde to 0.8 in the presence of 20 Pa formaldehyde implicating suppressed formaldehyde production from methanol transfer dehydrogenation events at low methanol pressures as the mechanistic basis for the observed effect of enhanced olefin cycle propagation. Co-reacting formaldehyde (11 Pa or 3 %C) with propene (0.1 kPa) on HZSM-5 at 623 K results in a 5.5-fold increase in aromatics selectivity suggesting Prins condensation reactions between formaldehyde and olefins are likely involved in aromatics production during methanol-to-hydrocarbons catalysis over HZSM-5.

2.2 Introduction

The dehydrative conversion of methanol-to-hydrocarbons (MTH) over zeolite or zeotype solid acids is industrially utilized for the selective production of ethene and propene[2, 3, 64–66]. Hydrocarbon and oxygenate cofeed, chemical transient, isotopic, and spectroscopic experimental studies [20, 23–25, 30, 31, 38, 67–73] and density functional theory (DFT) based computational studies [21, 22, 74, 75] note the stability and unreactive nature of methyl groups formed upon methanol dehydration in the absence of a primordial “hydrocarbon pool" comprised of olefins and aromatics contained within the microporous environment of the zeolite or zeotype catalyst. The hydrocarbon pool mechanism is summarized by a dual-cycle description where olefinic chemistries of methylation and β-scission (referred to as the olefins-based catalytic cycle) are interconnected with aromatic chemistries of methylation and dealkylation to form light olefins (referred to as the aromatics-based catalytic cycle) via hydrogen transfer and cyclization reactions [11, 26, 31, 32, 37, 39, 70, 76–79]. Isotopic switching experiments, where ^{12}C-methanol feed was switched with its ^{13}C-labeled counterpart during steady-state conversion on HZSM-5 at 623 K, showed ^{13}C content in ethene to closely match that of aromatics and disparate from that of C_{3+} olefins following the switch, thereby implicating aromatic-dealkylation as the predominant route for ethene production and evidencing that its production is mechanistically delinked from C_{3+} olefins [31, 39]. The description of propagation events during MTH based on separate but linked olefins- and aromatics-based methylation/cracking cycles has been exploited to modulate the molar ratio of propene and ethene (P/E) by changes in feed identity [33, 34, 45, 63, 80], operating conditions [41, 42, 81, 82], topology [10, 32, 64, 83–85], and textural properties [41, 47, 49, 53, 81, 86, 87] of the zeolite or zeotype catalyst formulations. Here, we report that methanol pressure is the salient experimental parameter in controlling P/E and establish methanol transfer dehydrogenation to produce formaldehyde and olefin-formaldehyde alkylation reactions as the mechanistic basis for this behavior.

The early and seminal work of Langner [11] noted that the addition of cyclic compounds to methanol feed resulted in an 18-fold reduction in the time required to achieve 50% methanol conversion and devoid of any description based on the hydrocarbon pool mechanism, postulated that methanol dehydrogenation produces formaldehyde which may be involved in Prins-type condensation reactions with olefins and aromatics during MTH. The observation of high methane selectivities concurrent with the initial hydrocarbon products in the effluent led researchers to postulate the existence of methanol disproportionation and dehydrogenation events [88–90] during MTH. This postulate is in agreement with theoretical treatments that followed these experimental demonstrations and mechanistic interpretations [91, 92]. The observation of longer catalyst lifetimes when using (i) dimethyl ether (DME) versus methanol as feedstock over different zeolite or zeotype catalysts [62, 63, 80], (ii) continuous stirred tank versus packed bed reactors for methanol conversion

on HZSM-5 [60], and (iii) low inlet methanol pressures or high contact times on CHA framework catalysts [43] can be rationalized as an effect of local methanol pressure on preferentially mediating methanol transfer dehydrogenation events in reference to methylation events involved in carbon chain-growth. Recent reports by Müller et al. [61], Hwang et al. [43], and Olsbye and co-workers [62, 63] have clearly explicated the role of formaldehyde, obtained from methanol dehydrogenation, in terminating propagation reaction sequences in MTH catalysis. The investigators purport formaldehyde to alkylate aromatics resulting in the transformation of active organic co-catalysts to inactive polycyclic species that occlude zeolite void spaces. Müller et al. [61] observed higher sensitivity of aromatic site-time yield to contact time at sub-complete versus complete methanol conversion, and higher aromatics selectivity utilizing methanol instead of DME as feedstock on HZSM-5 leading the authors to suggest methanol as a prolific hydride donor during MTH.

We demonstrate the critical role of formaldehyde in initiating the aromatics-based catalytic cycle, and in effect modulating P/E by noting a systematic increase in the selectivity of aromatics and ethene with increasing methanol concentration in the influent and in formaldehyde-methanol cofeed experiments. The likely involvement of Prins condensation reactions between formaldehyde and olefins at pressure and temperature conditions prevalent during MTH in forming aromatic co-catalysts is evidenced by the observation of a 5.5-fold increase in aromatics selectivity when co-processing formaldehyde (11 Pa or 3 %C) with propene (0.1 kPa) versus propene-only feed. We propose a revised version of the dual-cycle schematic describing MTH catalysis that includes formaldehyde-mediated C_1 chain-growth steps in addition to methylation.

2.3 Materials and Methods

2.3.1 Catalyst characterization

The ZSM-5 sample used in this study was obtained from Zeolyst Inc. (CBV8014) in ammonium form and converted to proton form by thermal treatment in flowing dry air ($1.67\,cm^3\,s^{-1}$; Minneapolis Oxygen) at 823 K ($0.018\,K\,s^{-1}$ ramp rate) for 4 h. The bulk Si/Al ratio (= 41.7) was ascertained from Scanning Electron Microscopy with Energy Dispersive X-ray Spectroscopy (SEM-EDS) measurements. The Si/Al ratio (= 42.7) in the near-surface region was obtained from X-ray Photoelectron spectroscopy (XPS) measurements and confirmed that Al is uniformly distributed in the lattice. X-ray diffraction (XRD) patterns were recorded using a Brüker micro-diffractometer with Cu-K_α (λ = 1.54 Å) as the radiation source to confirm its framework type as MFI. N_2 adsorption isotherms were obtained at 77 K using a Micromeritics surface area and porosity analyzer (ASAP 2020) after an initial degas (evacuation to $\leq$6 µmHg at 363 K) followed by thermal treatment in vacuo at 723 K ($0.0167\,K\,s^{-1}$ ramp rate) for 4 h and used to obtain the Brunauer-Emmett-Teller (BET) surface area ($386\,m^2\,g^{-1}$) and t-plot micropore volume ($0.12\,cm^3\,g^{-1}$) of the HZSM-5 sam-

ple. The Brønsted acid site density (0.20 mmol g^{-1}) was measured from NH_3 temperature programmed desorption performed by saturating ∼56 mg of HZSM-5 with flowing 500 ppm NH_3 (achieved by flowing a mixture of 0.083 $cm^3 s^{-1}$ 1.01% NH_3in balance He (Certified Standard, Praxair) and 1.58 $cm^3 s^{-1}$ He (99.997%, Minneapolis Oxygen)) at 323 K followed by a He purge (1.67 $cm^3 s^{-1}$; 99.997%, Minneapolis Oxygen) for 8 h at 323 K, and ramping the temperature at 0.083 K s^{-1} ramp rate to 823 K during which the effluent stream was monitored via mass spectrometry (MKS Cirrus) for signals corresponding to m/z = 16 (for NH_3) and 40 (for Ar (0.083 $cm^3 s^{-1}$; 99.9995%, Matheson) used as an internal standard) (Fig. 2.6).

2.3.2 Catalytic testing

Experiments were carried out in a borosilicate glass-lined stainless steel tube (SGE Analytical Science, 6.35 mm O.D. and 4 mm I.D.) reactor. 180 – 420 µm aggregates of HZSM-5 (∼3 – 30 mg) diluted with 150 – 420 µm particles of sand (Acros Organics; washed with 2 M HNO_3, rinsed with deionized water, and thermally treated in flowing dry air (1.67 $cm^3 s^{-1}$) at 1273 K for 16 h; $5 < wt_{diluent}/wt_{cat} < 30$) were packed between quartz wool plugs in the middle of reactor tube. The reactor was placed inside a resistively heated furnace (Model 3210, Applied Test Systems). The reaction temperature was measured using a K-type thermocouple (KMTXL-020U-12, Omega) wrapped around the reactor periphery with the tip placed near the axial-center and regulated with an electronic controller (Series 96, Watlow). The catalyst bed was thermally treated in flowing He (1.67 $cm^3 s^{-1}$; 99.997%, Minneapolis Oxygen) at 823 K (0.0167 K s^{-1} ramp rate) for 4 h prior to reaction. All liquid reagents including methanol (≥99.9%, Fluka), formaldehyde (16% w/v in water, Pierce), deionized water, or mixtures thereof were delivered using a syringe pump (KD Scientific), vaporized in heat traced lines (∼353 K), and swept by a flowing gas stream comprised of diluent (He) and internal standard (Ar). Propene (999.2 ppm balance Ar, Liquid Tech), He, and Ar flows were metered using mass flow controllers (Model 5850E, Brooks). The total gas-phase pressure during all experiments was ∼1 atm. Reactor influent and effluent stream compositions were quantified using a gas chromatograph (Model 7890A, Agilent) equipped with a dimethylpolysiloxane HP-1 column (50 m × 320 µm × 0.52 µm) connected in parallel to a flame ionization detector and a mass spectrometer (Model 5975C, Agilent) for detection of hydrocarbons and oxygenates, and a GS-GasPro column (60 m × 320 µm) connected to a thermal conductivity detector for detection of permanent gases (Ar and CO). DME, the dehydration product of methanol, in the effluent was considered as unconverted reactant, and the conversion was calculated as the total carbon atoms observed in the effluent hydrocarbon products as a fraction of the total carbon atoms in the effluent stream, including both methanol and DME. Selectivity was calculated based on the fractional amount of carbon atoms observed in a particular product group to the total amount of carbon atoms observed in all hydrocarbon products.

2.4 Results and Discussion

Trends in steady-state selectivity during MTH catalysis on HZSM-5 reflect trends in the relative propagation of the aromatics- versus olefins-based catalytic cycle. Larger ethene and aromatics selectivities reflect enhanced propagation of the aromatics-based cycle while larger propene and longer-chain aliphatic hydrocarbon selectivities reflect enhanced propagation of the olefins-based cycle [33, 34]. Moreover, kinetic studies of ethene and propene methylation with methanol or DME over HZSM-5 have shown ethene to be relatively inert towards methylation compared to propene, thereby rendering ethene as a termination product of the aromatics-based catalytic cycle during MTH [93–95]. Accordingly, Ilias et al. [96] proposed Ethene/2MBu—defined as the ratio of carbon selectivity of ethene and the combined selectivity of 2-methyl-2-butene and 2-methylbutane (collectively termed as '2MBu'; representative of products originating from the olefins-based catalytic cycle)—as a semi-quantitative indicator to assess the relative rates of propagation of aromatics- and olefins-based catalytic cycles during MTH on HZSM-5. The fact that ethene is produced exclusively from the aromatics-based cycle proffers a strategy to modulate the molar ratio of propene-to-ethene (P/E) by operating under conditions where propagation of this cycle is either suppressed or enhanced.

Fig. 2.1a presents selectivity trends observed with varying inlet methanol pressure (0.6 – 52.5 kPa) during methanol-to-hydrocarbons catalysis on HZSM-5 at 673 K and ∼1 atm total pressure, compared at iso-conversion (∼30 %C). Most notably, MBs (methyl-substituted benzenes or aromatics) and C_2 ($\geq$ 99% ethene) selectivities show a monotonically decreasing trend (5.9 – 0.1 %C and 9.8 – 1.5 %C, respectively) accompanied by a commensurate increasing trend in C_3 ($\geq$ 99% propene) selectivity (28.7 – 41.8 %C) and correspondingly, P/E (2 – 18) evidencing systematic suppression of aromatics-based methylation/dealkylation events and enhanced propagation of olefins-based methylation/cracking events with decreasing inlet methanol concentration. These observations are consistent with earlier reports by Chang et al. [42] and Dehertog et al. [81] which documented increasing propene yields at the expense of aromatics with decreasing inlet methanol pressure. The acquisition of product distribution data at complete conversion in the reports by Chang et al. [42] and Dehertog et al. [81], and the emergence of the dual-cycle description of MTH catalysis over zeolite or zeotype materials only in the past decade, however, precluded any mechanistic basis for the observed effects in the aforementioned reports. Ethene/2MBu exhibits a monotonically decreasing trend, as depicted in Fig. 2.1b, concurrent with the increasing trend observed in P/E with decreasing methanol concentration. The critical role of methanol pressure in influencing the relative rates of propagation of the two catalytic cycles is further corroborated by the monotonically decreasing trend observed in the relative molar selectivity of paraffins in the total amount of $C_1 - C_7$ hydrocarbons, termed as hydrogen transfer index (HTI), as shown in Fig. 2.1c. The decrease in paraffins selectivity

Table 2.1: C_2, aromatics and C_3 selectivities, and Ethene/2MBu, HTI and P/E versus inlet methanol pressure during MTH (∼30 %C conversion) on HZSM-5 at 673 K, 0.6 – 52.5 kPa CH_3OH, and 0.10 – 2.6 s $mol_{H^+} mol_C^{-1}$.

Inlet CH_3OH pressure / kPa	**0.6**	**2.5**	**13.2**	**52.5**
Selectivity / %C				
C_2 (≥ 99% ethene)	1.5	1.9	2.9	9.8
MBs	0.1	2.1	2.6	5.9
C_3 (≥ 99% propene)	41.8	38.2	35.4	28.7
Indicator				
Ethene/2MBu	0.25	0.32	0.42	1.02
HTI	0.06	0.07	0.09	0.15
P/E	18.0	14.4	8.2	2.0

accompanied by the decrease in aromatics selectivity is a stoichiometric requirement for hydrogen-redistribution pathways prevalent during hydrocarbons conversion mediated by zeolites with Brønsted acidity. Table 2.1 lists ethene, aromatics and propene selectivities, and Ethene/2MBu, HTI and P/E obtained for different inlet methanol pressures employed during the MTH study on HZSM-5. Figs. 2.2a and 2.2b demonstrate the steady nature of selectivity observed at 2.5 kPa methanol pressure and 673 K against variations in time on stream or contact time. Moreover, aromatics and ethene selectivities remain insignificant and exhibit indiscernible trends with increasing or decreasing temperature for methanol feed at a low pressure (0.6 kPa) and 673 K (Fig. 2.1d), thereby demonstrating methanol pressure as critical in influencing P/E irrespective of the reaction temperature.

The observed increase in selectivity of hydrogen transfer products (aromatics + paraffins) with increasing methanol pressure clearly suggests direct involvement of methanol in hydrogen redistribution pathways over a wide-range of temperatures relevant for MTH. This inference is consistent with the conclusion put forward by Müller et al. [61] regarding the predominant role played by methanol-induced hydrogen transfer pathways over olefins-induced hydrogen transfer pathways in aromatics synthesis under conditions resulting in sub-complete methanol conversion during MTH on HZSM-5. Transfer dehydrogenation of methanol with olefins or itself results in the formation of hydrogen-deficient formaldehyde and hydrogen-rich paraffins [11, 43, 61–63, 88, 91, 92]. Formaldehyde subsequently alkylates olefins in Prins condensation cascades producing polyunsaturated species mediating dehydrocyclization of olefins to aromatics [43, 62].

We corroborate the prevalence of formaldehyde-mediated aromatics production pathways by reacting methanol at low pressure (0.6 kPa) with increasing concentration (3 – 20 Pa or 0.5 – 5 %C) of formaldehyde cofeed on HZSM-5 at 623 K. Fig. 2.3a shows the effects of processing formaldehyde-methanol mixtures compared to methanol-only feed on selectivity

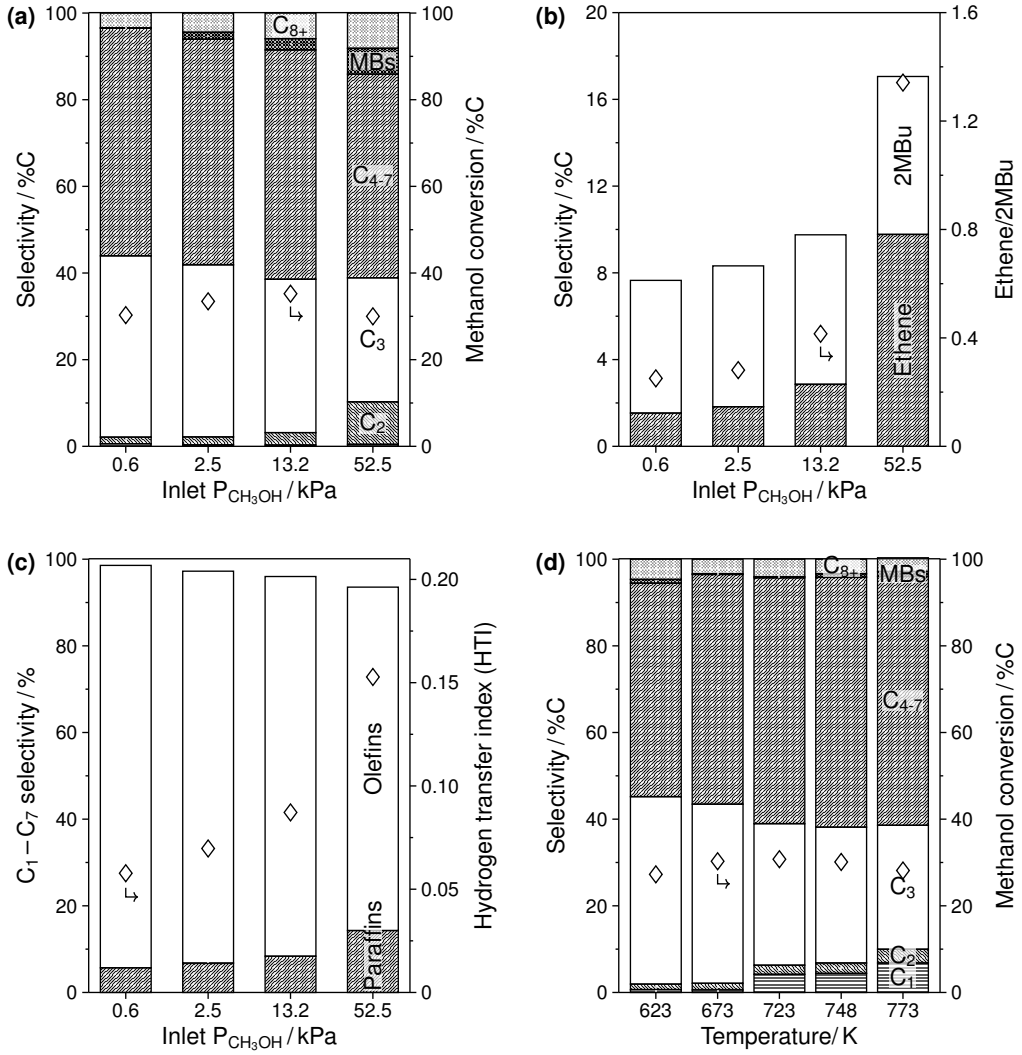

Fig. 2.1: (a) Selectivity (*left* ordinate) and methanol conversion (*right* ordinate, ◊), (b) Ethene and 2MBu (sum of 2-Methyl-2-butene and 2-Methylbutane) selectivities (*left* ordinate) and their ratio (*right* ordinate, ◊), and (c) molar selectivities of C_1-C_7 paraffins and C_2-C_7 olefins (*left* ordinate) and hydrogen transfer index (HTI) defined as the fractional molar content in paraffins to the total molar amount of C_1-C_7 hydrocarbons (*right* ordinate, ◊) versus inlet methanol pressure; (d) Selectivity (*left* ordinate) and methanol conversion (*right* ordinate, ◊) versus temperature during MTH on HZSM-5 at (a) – (c) 673 K, 0.6 – 52.5 kPa CH_3OH, and 0.10 – 2.60 s $mol_{H^+} mol_C^{-1}$; (d) 623 – 773 K, 0.6 kPa CH_3OH, and 1.73 – 17.3 s $mol_{H^+} mol_C^{-1}$.

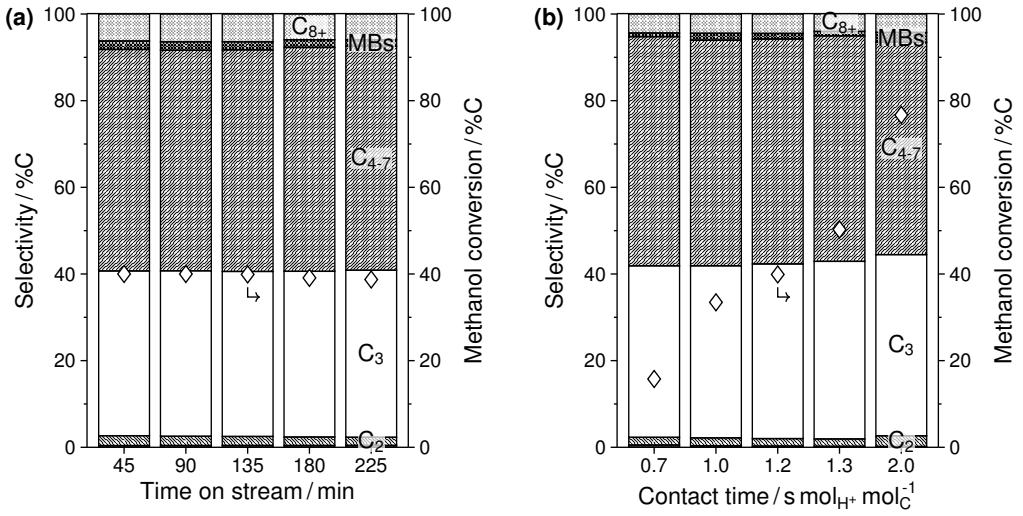

Fig. 2.2: Selectivity (*left* ordinate) and methanol conversion (*right* ordinate, ♢) versus (a) time on stream, and (b) contact time during MTH on HZSM-5 at 673 K, 2.5 kPa CH_3OH, and 1.2 s $mol_{H^+} mol_C^{-1}$ for (a).

and methanol conversion, and Fig. 2.3b shows the effect on ethene and 2MBu selectivities, and their ratio (comparison made at 45 min time on stream). Ethene and aromatic selectivities, and Ethene/2MBu exhibit a monotonically increasing trend accompanied by a concomitant decreasing trend in propene selectivity with increasing formaldehyde cofeed concentration indicating enhanced rates of propagation of the aromatics-based cycle over its olefins-based counterpart during MTH. Figs. 2.7a and 2.7b present time on stream profiles of conversion and aromatics selectivity during reactions involving formaldehyde cofeeds with methanol showing systematically increasing trends in aromatics selectivity and deactivation rates with increasing formaldehyde cofeed concentration in agreement with results reported in three other recent reports [43, 61, 63]. The increase in deactivation rates with formaldehyde cofeed is attributed to the involvement of formaldehyde in the transformation of active hydrocarbon pool species to inactive coke precursors [43, 61, 62]. Table 2.2 lists ethene, aromatics and propene selectivities, and Ethene/2MBu, HTI and P/E evidencing enhanced propagation of the aromatics-based catalytic cycle over its olefins-based counterpart as a result of increasing formaldehyde cofeed concentration in the methanol feed. We note that HTI does not increase significantly with increasing aromatics production resulting from increasing concentration of formaldehyde in the influent. This is in line with our postulate that formaldehyde-mediated dehydrative alkylation is the dominant pathway resulting in the transformation of olefins to aromatic precursors as opposed to olefins-based hydrogen transfer pathways which would result in significantly higher HTI alongside higher aromatics production during MTH.

We performed reactions of propene with and without formaldehyde cofeed on HZSM-5 to further evidence formaldehyde-mediated dehydrocyclization of olefins to produce aro-

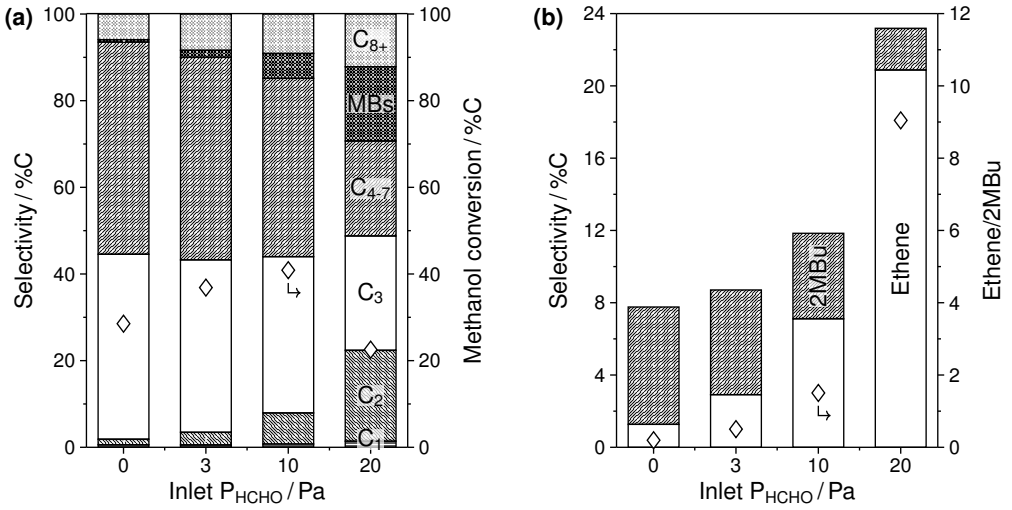

Fig. 2.3: (a) Selectivity (*left* ordinate) and methanol conversion (*right* ordinate, ◊), and (b) Ethene and 2MBu (sum of 2-Methyl-2-butene and 2-Methylbutane) selectivities (*left* ordinate) and their ratio (*right* ordinate, ◊) versus inlet formaldehyde cofeed pressure during reactions of formaldehyde-methanol mixtures on HZSM-5 at 623 K, 0.6 kPa CH_3OH, 3 – 20 Pa HCHO (+ 30 – 200 Pa H_2O), and 17.3 s $mol_{H^+}mol_C^{-1}$; 45 min time on stream (Fig. 2.7 shows the time on stream profiles of conversion and aromatics selectivity).

Table 2.2: C_2, MBs and C_3 selectivities, and Ethene/2MBu, HTI and P/E versus inlet HCHO cofeed pressures during methanol conversion on HZSM-5 at 623 K, 0.6 kPa CH_3OH, 3 – 20 Pa HCHO (+ 30 – 200 Pa H_2O), and 17.3 s $mol_{H^+}mol_C^{-1}$; 45 min time on stream.

Inlet HCHO cofeed pressure / Pa	**0**	**3**	**10**	**20**
Selectivity / %C				
C_2 ($\geq$ 99% ethene)	1.2	2.7	7.2	21.0
MBs	0.6	1.6	5.7	17.1
C_3 ($\geq$ 99% propene)	42.8	38.2	36.1	26.4
Indicator				
Ethene/2MBu	0.2	0.5	1.5	9.0
HTI	0.05	0.05	0.06	0.07
P/E	24.7	9.1	3.4	0.8

matics. Cofeeding small amounts of formaldehyde (11 Pa or 3 %C) with propene (0.1 kPa) resulted in a 1.6-fold increase in conversion and a 5.5-fold increase in aromatics selectivity (Fig. 2.4a; 2.4b shows the time on stream profiles of both conversion and aromatics selectivity, and indicates steady-state behavior) supporting the likely involvement of Prins condensation reactions between formaldehyde and olefins in forming aromatics. Aromatics (or MBs) produced on feeding only propene most likely arise from oligomerization and olefins-based hydrogen transfer pathways [97], however, cofeeding small amounts of formaldehyde is observed to accelerate the rate of transformation of (C_4 - C_7) species to aromatics (Fig. 2.4a). The marked increase in aromatics selectivity upon cofeeding formaldehyde with both

methanol and propene feeds supports a C_1 chain-growth mechanism mediated by formaldehyde as an alternative to olefin-based oligomerization and hydrogen transfer pathways for aromatics synthesis [97]. The implied relevance of Prins condensation mediated dehydrocyclization pathways in aromatics production leads us to propose a modified version of the dual-cycle schematic that describes propagation events during MTH (Scheme 2.1) which demonstrates a C_1 addition pathway involving alkylation with formaldehyde as a parallel chain-growth mechanism to methylation with methanol. Methanol can undergo transfer dehydrogenation with either itself or an olefin to form formaldehyde and paraffins (CH_4 and higher homologues). For instance, in the olefins-based catalytic cycle, propene can react with either methanol or formaldehyde to form butene or 1,3-butadiene, respectively after dehydration. In an analogous manner, butene and its next higher homologue, 2-methyl-2-butene, can undergo dehydrative alkylation with either methanol or formaldehyde to form higher olefins or polyunsaturated species, respectively. These species can subsequently undergo dehydrocyclization to form aromatics and paraffins, or β-scission to form light olefins. In the aromatics-based catalytic cycle, aromatics (or methyl-substituted benzenes) can undergo methylation events to form higher homologues and dealkylation with methanol to produce light olefins and smaller homologues.

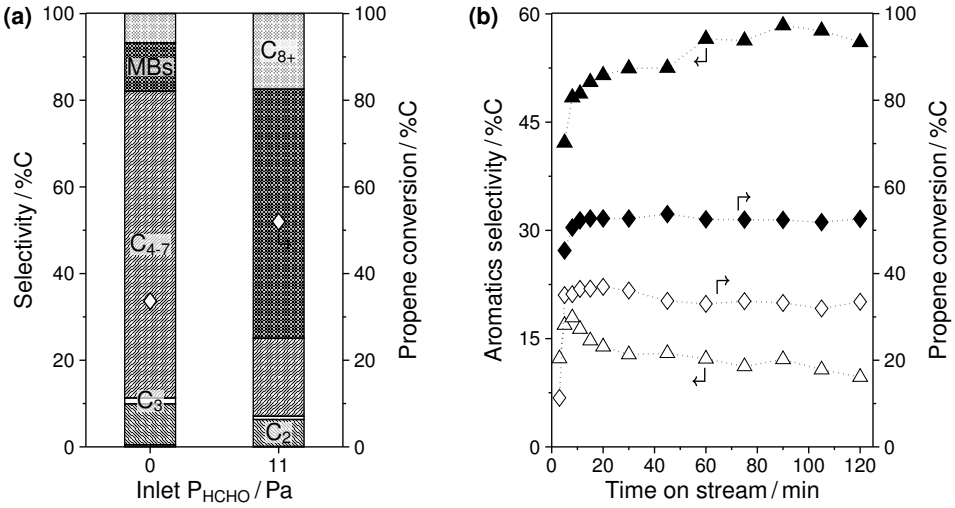

Fig. 2.4: (a) Selectivity (*left* ordinate) and propene conversion (*right* ordinate, ◊) versus inlet formaldehyde cofeed pressure, and (b) Aromatics selectivity (*left* ordinate, △) and propene conversion (*right* ordinate) versus time on stream during reactions of HCHO-propene mixtures (filled symbols) and propene-only (empty symbols) feeds over HZSM-5 at 623 K, 0.1 kPa $C_3^=$, 11 Pa HCHO, 13 kPa H_2O, and 1040.2 s $mol_{H^+} mol^{-1}_{C_3H_6}$.

These results demonstrate enhanced propagation of the aromatics-based cycle with increasing methanol pressure and/or formaldehyde cofeed concentration in the influent implicating the prevalence of formaldehyde-mediated dehydrocyclization of olefins to aromatics during steady-state MTH catalysis on HZSM-5. Methanol pressure, therefore, is paramount

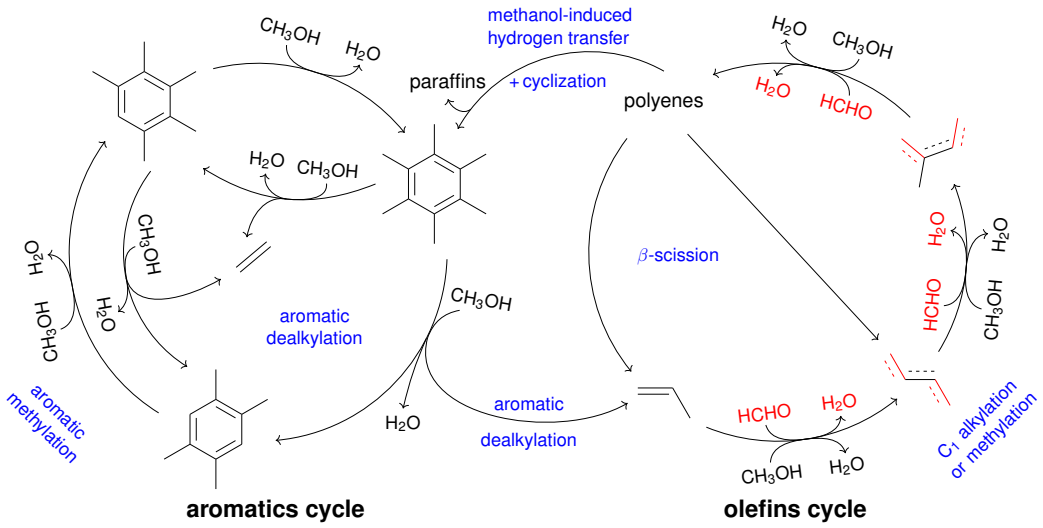

Scheme 2.1: Modified version of the dual-cycle schematic describing propagation events in MTH showing a supplementary C_1 chain-growth mechanism mediated by successive dehydrative addition of formaldehyde (derived from transfer dehydrogenation of methanol with either itself or an olefin) leading to the formation of polyunsaturated species which can dehydrocyclize to form aromatic co-catalysts. The original version was adapted from [38].

in exercising control over the relative rates of propagation of the two catalytic cycles and correspondingly propene-to-ethene molar ratio during methanol-to-hydrocarbons catalysis over zeolite materials.

2.5 Conclusions

Varying inlet methanol pressure from 0.6 – 52.5 kPa at 673 K engenders a 9-fold increase in the propene-to-ethene molar ratio from 2 – 18 during steady-state MTH catalysis on HZSM-5. This effect is observed to be persistent irrespective of variations in time on stream, contact time, and temperature implicating methanol pressure as critical in decoupling of the aromatics- and olefins-based catalytic cycles where low pressures of methanol result in enhanced propagation of the olefinic cycle over its aromatics counterpart irrespective of the other experimental parameters considered. Studies in which formaldehyde is co-fed with methanol in the reactor influent explicitly demonstrate the salient role played by formaldehyde in initiating the aromatics-based methylation/dealkylation events during MTH, inducing a 31-fold decrease in P/E from 24.7 in the case of 0.6 kPa methanol-only feed to 0.8 in the case of 20 Pa HCHO cofeed with methanol during MTH on HZSM-5 at 623 K. Reactions involving formaldehyde cofeed (11 Pa or 3 %C) with propene (0.1 kPa) result in a 5.5-fold increase in aromatics selectivity compared to a propene-only feed corroborating the likely involvement of Prins condensation chemistry between formaldehyde and olefins in the formation of polyunsaturated intermediates which can dehydrocyclize to produce aromatics under MTH conditions.

Acknowledgments

We acknowledge (i) Dow through the University Partnership Initiative and the National Science Foundation (CBET 1701534) for financial support, (ii) Dr. Seema Thakral and Dr. Bing Luo from the Characterization Facility, University of Minnesota, which receives partial support from the National Science Foundation through the Materials Research Science and Engineering Centers program, for providing the X-ray diffraction and X-ray photoelectron spectroscopy data, respectively, (iii) Mr. Andrew Hwang from the University of Minnesota for collecting the ammonia temperature programmed desorption measurements of the HZSM-5 sample, and (iv) Mr. Brandon Foley from the University of Minnesota for insightful discussions.

2.6 Supplementary Information

2.6.1 X-ray diffraction

The XRD patterns of the HZSM-5 sample used in the study and of a reference MFI framework sample obtained from IZA [98] are shown in Fig. 2.5.

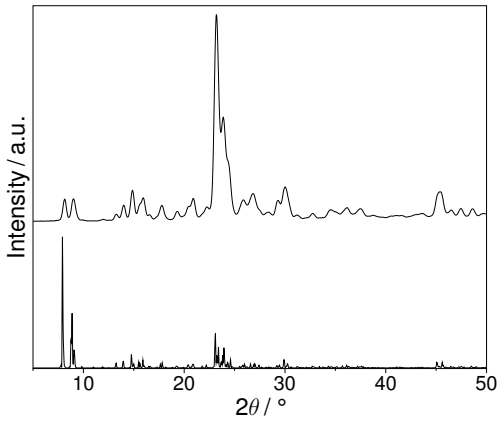

Fig. 2.5: XRD patterns of the HZSM-5 sample used in the study (*top*) along with the reference spectra of a MFI sample obtained from IZA [98] (*bottom*).

2.6.2 NH_3 temperature programmed desorption

The temperature programmed desorption profile of ammonia observed for the HZSM-5 sample used in the study is shown in Fig. 2.6. The area under the high-temperature curve (centered at around 623 K, blue-colored) was enumerated as the Brønsted acid site density ($0.20\,\mathrm{mmol\,g^{-1}}$), assuming a 1:1 stoichiometry between desorbed NH_3 and Brønsted acid site.

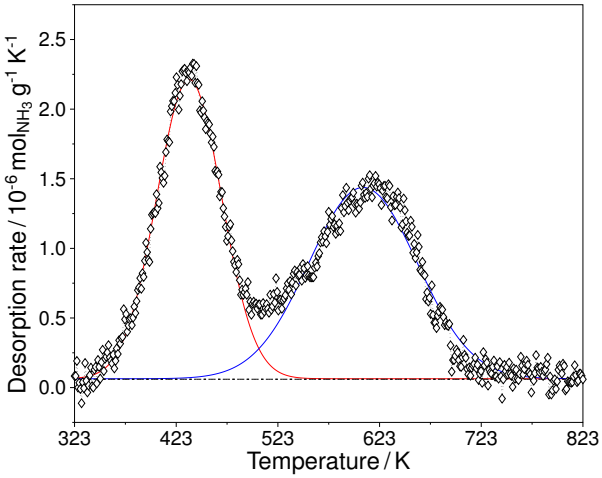

Fig. 2.6: NH_3 ($m/z = 16$) desorption rate observed during temperature ramp at 0.083 K s^{-1} to 823 K in combined He and Ar flow following saturation of HZSM-5 with NH_3 at 323 K. The deconvoluted gaussian fitted curves characterized by a low-temperature peak (centered around ~423 K) and a high-temperature peak (centered around ~623 K) are shown as red- and blue-colored lines, respectively.

2.6.3 Conversion and aromatics selectivity profiles during methanol conversion with formaldehyde cofeeds on HZSM-5

Transient profiles showing a monotonically increasing trend in aromatics selectivity (Fig. 2.7a) accompanied by a monotonic deleterious effect on catalyst stability (Fig. 2.7b) with increasing HCHO cofeed concentrations (0 – 20 Pa) in methanol (0.6 kPa) feed.

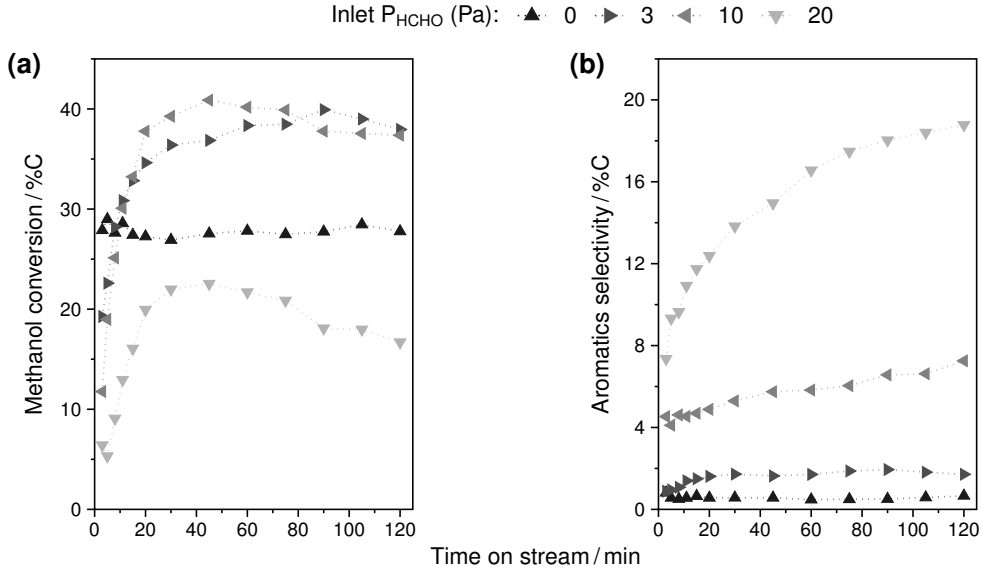

Fig. 2.7: (a) Methanol conversion and (b) aromatics selectivity profiles with increasing HCHO cofeed concentrations (0 – 20 Pa) during MTH on HZSM-5 at 623 K, 0.6 kPa CH_3OH, and 17.3 s $mol_{H^+} mol_C^{-1}$.

Chapter 3

Effects of CO cofeeds on methanol to hydrocarbons catalysis over HZSM-5 and its mechanistic basis

3.1 Abstract

Methanol feeds with excess CO (CO/CH_3OH >100) compared to He at 673 K result in enhanced aromatics and ethene production at the expense of $C_3 - C_7$ olefins at early turnovers indicating enhanced propagation of aromatics cycle over its olefinic counterpart. The ratio of alkanes-to-aromatics is also lower in the case of methanol/CO feeds compared to methanol/He feeds. The catalyst lifetime is, however, short with CO cofeeds and as the conversion decreases with increasing turnovers, the combined selectivity of oxygenates (methyl acetate, CH_3COOCH_3, and acetic acid, CH_3COOH) increases simultaneously. These observations can be rationalized as a consequence of CO incorporation into the hydrocarbon pool via carbonylation of methanol-derived surface species to form acetyl intermediates that can desorb into the gas-phase either via involvement in hydrogen transfer reactions to form the corresponding aldehydes, or via hydrolysis or methanolysis to form the corresponding carboxylic acids or esters which can ketonize via coupling reactions. The resulting aldehydes and ketones can undergo aldol-condensation to form higher unsaturated homologues which can form aromatics via a network of hydrogen transfer, decarbonylation, cyclization, and dehydration steps. Aromatics production was significantly enhanced (∼5×) during methanol/acetic acid feeds compared to methanol-only feeds at iso-conversion levels (∼2.3 %C), and no carbonyl compounds or selectivity changes were detected during reactions of propene/CO/H_2O mixtures compared to propene/He/H_2O feeds. These observations lend credence to the proposal that the intermediate formation of acetyl species from co-reaction of methanol and CO followed by the formation of aldehydes and ketones likely underlies the observed selectivity changes during methanol conversion with high-pressure CO cofeeds over HZSM-5.

3.2 Introduction

The dehydrative conversion of methanol to hydrocarbons (MTH) over solid acid zeolite or zeotype catalysts propagates via a hydrocarbon pool mechanism wherein organic co-catalysts entrained within the zeolite pores act as scaffolds for repeated methylation and dealkylation steps [26, 37, 38]. The reactions of methylation and β-scission involving olefinic co-catalysts are referred as the 'olefins cycle' while methylation and dealkylation reactions involving aromatic co-catalysts are referred as the 'aromatics cycle'. The two cycles are interconnected by hydrogen transfer and cyclization reactions which mediate the transformation of olefins to aromatics while resulting in the concomitant formation of alkanes [61, 99]. Ethene is considered to be derived predominantly from the aromatics cycle via dealkylation, as evidenced from isotopic switching experiments which show that the amount of ^{13}C incorporation in ethene and aromatics matches closely and is distinct from that observed in C_{3+} olefins after ^{12}C-methanol is switched to ^{13}C-methanol feed [31, 39].

The direct incorporation of carbon atoms from carbon monoxide to promote aromatics production during methanol conversion was recently reported by Cheng et al. [100] and Chen et al. [46]. Cheng et al. [100] noted that at complete methanol conversion, the aromatics selectivity increased to ~34 – 75%C during methanol (0.09 – 1.8 bar) feeds with CO (0.9 – 18 bar) cofeeds relative to ~18%C observed during methanol (0.09 bar) feed with N_2 (0.9 bar) cofeed on a bifunctional catalyst formulation of Zn-ZrO_2/HZSM-5 at 703 K and 20 h time on stream. This increase in aromatics production were observed without an increase in $C_2 - C_4$ alkanes selectivity which remained ~21%C irrespective of the CO cofeed concentrations. Cofeeding CO (0.9 bar) in place of N_2 with methanol (0.09 bar) on HZSM-5 alone, however, did not result in any enhancement of aromatics selectivity (~21 %C), which led the authors to propose that the metal functionality is important and that CO molecules chemisorbed on Zn-ZrO_2 nanoparticles could act as hydrogen acceptors to form CH_3OH while resulting in increased aromatics production from methanol conversion without the simultaneous increase in alkanes formation. This proposal was supported by the enhancement in aromatics selectivity (~14 – 82 %C) observed as the intimacy of the two components (Zn-ZrO_2 and HZSM-5) was increased from dual-bed (Zn-ZrO_2 bed upstream of HZSM-5 separated by quartz wool) to dispersed (Zn-ZrO_2 nanoparticles dispersed on micrometer-sized HZSM-5 crystals) configurations. The $C_2 - C_4$ alkanes selectivity, on the other hand, decreased from ~38 %C to ~13 %C with increasing intimacy of the two catalytic components. In a review article on hydrogen spillover, Prins [101] argued that the migration of H atoms from an insulating non-reducible surface (for instance, zeolite) to that of the metal would have large enthalpic barriers (>260 kJ/mol) and therefore, the proposal of H migration from the zeolite surface to the CO molecules adsorbed on Zn-ZrO_2 seems unlikely. In a later study, Chen et al. [46] showed that the metal component (for instance, Zn-ZrO_2) is not necessary for the promotional effect of CO cofeeds on aromatics production by demon-

strating that at complete methanol conversion, ∼80 %C initial aromatics selectivity can be achieved with high-pressure (∼40 bar) CO cofeeds compared to ∼40 %C observed in the case of N_2 cofeeds with methanol (0.35 bar) on HZSM-5 alone at 673 K. The $C_2 - C_4$ alkanes selectivity in the case of CO cofeeds was only ∼20 %C compared to ∼53 %C observed in the case of N_2 cofeeds. Based on the observations of (i) low reactivity of propane/CO, CO-only and CO/H_2 (2:1) feeds, and (ii) detection of carbonyl compounds (acetic acid, CH_3COOH and methyl acetate, CH_3COOCH_3) at the beginning of deactivation during methanol conversion with CO cofeeds on the HZSM-5 sample at 673 K, the authors proposed that these carbonyl compounds generated from coupling of CO and CH_3OH via Koch-type reactions [102] act as key intermediates which can produce methyl-cyclopentenones (MCPOs) via reaction with olefins, and the MCPOs can further transform to aromatics. MCPOs were not observed in the effluent stream during methanol conversion with N_2/CO cofeeds but were only detected during analysis of the organic extracts obtained from dissolution-extraction experiments performed on the HZSM-5 sample post methanol feed with somewhat higher amounts in the case of CO versus N_2 cofeeds. No mechanistic details pertaining to the formation of methyl-cyclopentenones via reactions of olefins and aforementioned carbonyl compounds, and their further transformation to aromatics via elimination of water were discussed.

In this study, we report that at both sub-complete and complete methanol conversion, co-feeding CO results in increased aromatics (and ethene) production at the expense of $C_3 - C_7$ olefins indicating preponderance of the aromatics cycle compared to its olefinic counterpart. The enhancements are, however, observed with accelerated rates of catalyst deactivation and alike the observations reported by Chen et al. [46], acetic acid and methyl acetate are detected in the effluent with reaction progress. We suggest, based on independent experiments involving methanol/acetic acid mixtures and propene/CO/H_2O mixtures, that the noted enhancements in aromatics selectivity during methanol conversion with CO cofeeds can likely be rationalized based on the formation of aldehydes and ketones from the acetyl intermediates generated by carbonylation of the methanol-derived surface species.

3.3 Materials and Methods

3.3.1 Catalyst characterization

The ZSM-5 samples (CBV2314, Si/Al = 11.5, and CBV8014, Si/Al = 41.7) used in this study were obtained from Zeolyst in ammonium form and converted to proton form by thermal treatment in flowing dry air (1.67 $cm^3\,s^{-1}$; Zero Grade, Matheson) at 823 K (0.0167 $K\,s^{-1}$ ramp rate from RT) for 4 h. The characterization details of the CBV8014 sample have been reported in Chapter 2. Briefly, the bulk Si/Al ratio (= 41.7) was obtained from Scanning Electron Microscopy with Energy Dispersive X-ray spectroscopy (SEM-EDS) measurements. The Si/Al ratio (= 42.7) in the near-surface region was obtained from X-ray

Photoelectron spectroscopy (XPS) measurements and confirmed that Al is uniformly distributed in the lattice. The Brunauer-Emmett-Teller (BET) surface area and t-plot micropore volume are $386\,m^2\,g^{-1}$ and $0.12\,cm^3\,g^{-1}$, respectively, as ascertained from N_2 adsorption measurements at 77 K. The Brønsted acid site density ($0.20\,mmol\,g^{-1}$) was enumerated from NH_3 temperature programmed desorption measurements.

3.3.2 Catalytic testing

All experiments were performed in a borosilicate glass-lined stainless steel reactor tube (6.35 mm outer diameter and 4 mm inner diameter; Scientific Glass Engineering). The proton-form zeolite sample was subject to pelletization, crushing, and sieving to retain 180-250 µm (60-80 mesh) aggregates which were physically mixed with aggregates of sand (Acros Organics; subjected prior to an overnight wash in 2 M HNO_3 solution followed by deionized water rinse until pH ∼7, and a final thermal treatment in flowing dry air ($1.67\,cm^3\,s^{-1}$) at 1273 K ($0.083\,K\,s^{-1}$ ramp rate from RT) for 16 h; $10 < wt_{diluent}/wt_{cat} < 15$) and packed in the middle of the reactor tube between quartz wool (Technical Glass Products) plugs. The tubular reactor was placed inside a resistively heated furnace (Model 3210, Applied Test Systems), and the reaction temperature was measured using a K-type thermocouple (TJ36-CAXL-020U-12, Omega) wrapped around the reactor periphery with the tip placed near the axial-center and regulated with an electronic controller (Series 96, Watlow). The free volume above and below the catalyst bed was occupied by quartz rods (3 mm O.D.; Technical Glass Products) to prevent any vertical displacement of the catalyst bed. Prior to catalytic measurements, the catalyst bed was pretreated in flowing dry air ($1.67\,cm^3\,s^{-1}$) at 823 K ($0.0167\,K\,s^{-1}$ ramp rate from RT) for 4 h before being allowed to cool down to 673 K and being subject to a He ($1.67\,cm^3\,s^{-1}$; 99.997%, Matheson) purge at 673 K for ≥2 h. All gas flows including CO (99.999%, Matheson), H_2 (99.9999%, Matheson), propene (999.2 ppm balance Ar, Liquid Tech), He, and Ar (99.9995%, Matheson) were metered using mass flow controllers (Model 5850E, Brooks). A carbonyl and sulfur trap (a 3:1 v/v mixture of activated carbon (GCN48, Norit) placed upstream and Cu-Zn oxide (PuriStar R3-12, BASF) placed downstream packed in a stainless steel tube (6.35 mm outer diameter and 4 mm inner diameter)) was placed downstream of the CO cylinder and upstream of the mass flow controller. All liquid flows including methanol (≥99.9%, Fluka), acetic acid (≥99.0%, ReagentPlus®, Sigma), or mixtures thereof were delivered using a syringe pump (Legato 100, KD Scientific), vaporized in heat traced lines (∼358 K), and swept by the flowing gas stream. The total gas-phase pressure was measured using a pressure transducer (0 – 6890 kPag; PX32B1-1KGV, Omega) placed upstream of the reactor tube, and controlled using a back-pressure regulator (0 – 3440 kPag; 44-2300 series, Tescom) placed downstream. The composition of the reactant and product streams were quantified using a gas chromatograph (Model 7890A, Agilent) equipped with a dimethylpolysiloxane HP-1 column (50 m × 320 µm × 0.52 µm) connected to a flame ionization detector and a mass spectrometer

(Model 5975C, Agilent) for detection of hydrocarbons, and a GS-GasPro column (60 m × 320 µm) connected to a thermal conductivity detector for detecting permanent gases (H_2, CO, CO_2, and Ar). Dimethyl ether (DME), the dehydration product of methanol, in the effluent was considered as unconverted reactant along with methanol, and conversion was defined as the ratio of the total carbon flow rate of effluent hydrocarbons to the total carbon flow rate of effluent hydrocarbons and unconverted reactants. Cumulative turnovers, defined as the cumulative amount of methanol/DME-derived carbon atoms normalized by the total acid sites in the catalyst bed observed in effluent hydrocarbons at a certain time on stream, was used to assess reaction progress.

3.4 Results and Discussion

3.4.1 CO cofeeds with CH_3OH

Cofeeding excess CO (CO/CH_3OH >100) with methanol results in an increase in the initial aromatics and ethene selectivity compared to the case of methanol feed with He both at sub-complete (11.8 and 12.3 %C versus 7.8 and 9.5 %C at sub-complete methanol conversion, Fig. 3.1) and complete methanol conversion (27.3 and 18.1 %C versus 12.9 and 11.3 %C at complete methanol conversion, Fig. 3.2) over HZSM-5 at 673 K. In context of the hydrocarbon pool mechanism, these selectivity changes reflect enhanced propagation of the aromatics cycle over its olefinic counterpart during methanol conversion with CO cofeeds. On the other hand, the initial alkanes-to-aromatics molar ratios are observed to be lower with CO cofeeds due to suppressed formation of alkanes alongside higher aromatics production. These beneficial effects of increased aromatics production without the concomitant increase in alkanes formation are, however, transient in nature and the catalyst deactivates rapidly with reaction progress. The selectivity of hydrocarbon products decreases with the simultaneous increase in the selectivity of carbonyl compounds, methyl acetate and acetic acid, as methanol conversion decreases, indicating their relevance to the enhanced aromatics production observed at early turnovers. Small cumulative amounts of formaldehyde and acetone (3.4 %C and 1.5 %C, respectively, with 0.6 bar CO cofeeds and 0.006 bar CH_3OH; and 3.5 %C and 6.0 %C, respectively, with 8 bar CO cofeeds and 0.01 bar CH_3OH) were also observed in the effluent.

The formation of aforementioned carbonyl compounds can be explained by zeolites-catalyzed Koch-type reactions wherein CO insertion to dehydrated methanol-derived surface species results in the formation of acetyls that can undergo hydrolysis (path (i) in Scheme 3.1) or methanolysis (path (ii) in Scheme 3.1) to form acetic acid or methyl acetate, respectively [103, 104]. Acetic acid and methyl acetate can further undergo ketonization via coupling reactions to generate acetone with the concomitant production of CO_2 and methanol/dimethyl ether (path (iv) in Scheme 3.1) [105]. Apart from hydrolysis or methanolysis, the acetyls can also undergo transfer hydrogenation with methanol to gener-

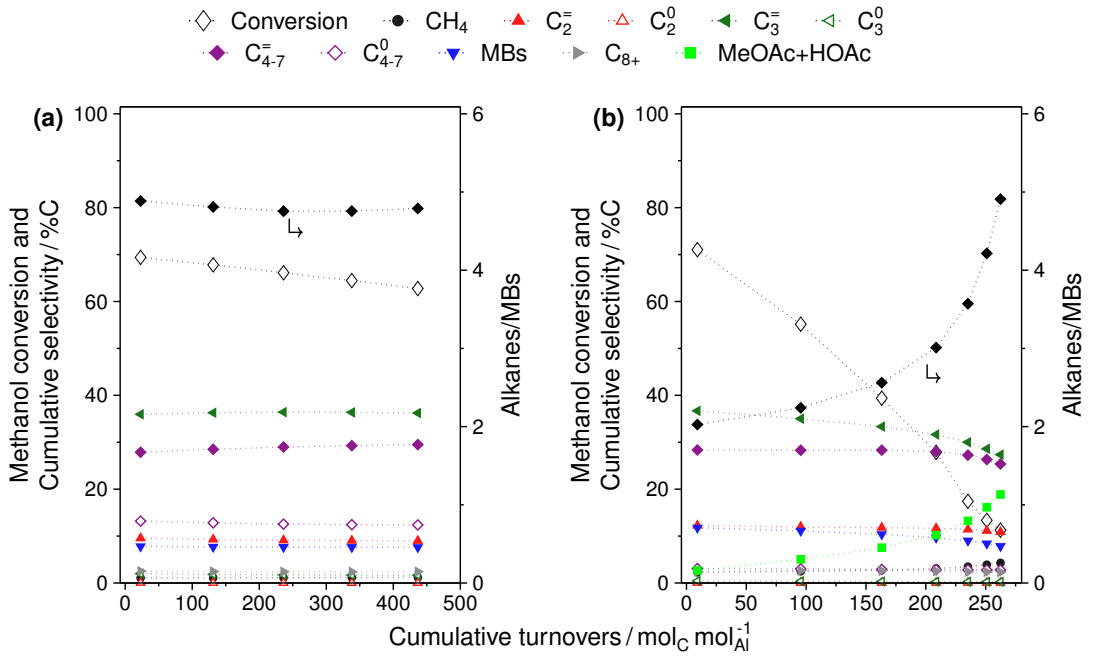

Fig. 3.1: Methanol conversion and cumulative selectivity (*left* ordinate), and alkanes/mbs molar ratio (*right* ordinate, ◆) versus cumulative turnovers during reactions of 0.006 bar methanol with (a) 1.2 bar He and (b) 0.6 bar CO cofeeds on 3.8 mg HZSM-5 (Zeolyst CBV2314) at 673 K and 68.7 mol_{CH_3OH} $(mol_{Al} \cdot ks)^{-1}$. The superscripts '=' and '0' in the legend represent olefinic and paraffinic fractions of the particular carbon group; 'MBs' and 'MeOAc+HOAc' represent methyl-substituted benzenes, and combined sum of methyl acetate and acetic acid, respectively.

ate acetaldehyde and formaldehyde (path (iii) in Scheme 3.1). This pathway is suggested based on the known role of methanol as a hydrogen donor during methanol conversion over zeolites [61, 62, 99, 106]. The generated aldehydes and ketones can then undergo aldol condensation reactions to generate higher unsaturated homologues that can participate in a network of hydrogen transfer, decarbonylation, cyclization, and dehydration steps to generate aromatics, as evidenced in previous experimental reports on acetaldehyde and acetone conversion on zeolites [45, 107, 108]. The suggested role of acetyls as hydrogen acceptors provides a basis for the suppressed formation of paraffins alongside the increased aromatics production noted at early turnovers.

3.4.2 CH_3COOH cofeeds with CH_3OH

We carried out acetic acid cofeed experiments to corroborate its involvement in aromatics production during methanol conversion via the proposed ketonization pathway. The primary product (~99.3 %C selectivity) resulting from acetic acid conversion (~90 %C) was methyl acetate which is likely produced from the esterification reaction of acetic acid and methanol. However, in terms of the effluent hydrocarbon composition, co-feeding acetic

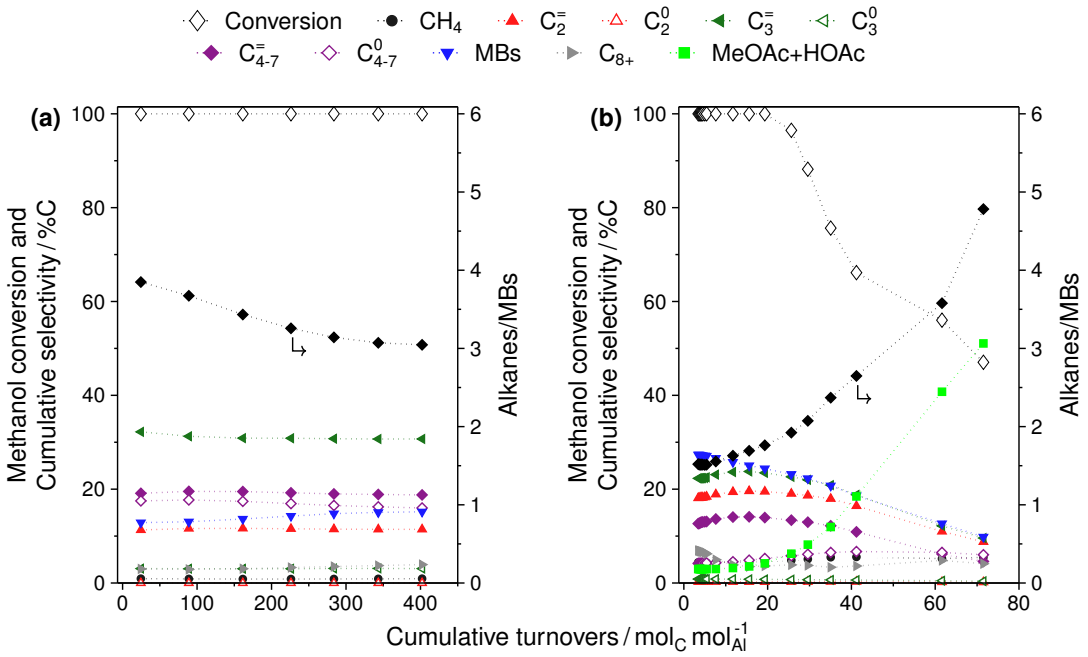

Fig. 3.2: Methanol conversion and cumulative selectivity (*left* ordinate), and alkanes/mbs molar ratio (*right* ordinate, ◆) versus cumulative turnovers during reactions of 0.01 bar methanol with (a) 1 bar He and (b) 8 bar CO cofeeds on 3.8 mg HZSM-5 (Zeolyst CBV2314) at 673 K and 27.5 mol_{CH_3OH} $(mol_{Al}{\cdot}ks)^{-1}$.

acid (1:10 mol/mol) with methanol results in a significant enhancement (∼5×) in aromatics selectivity at iso-conversion levels (∼2.3 %C) (Fig. 3.3). The aromatics distribution (Table 3.1) reflects a notable increment in the combined selectivity of tri- and tetramethylbenzenes (∼45.2 %C versus ∼31.2 %C) as a consequence of acetic acid cofeeds, consistent with self-condensation of acetone that results in the formation of trimethylbenzenes [107, 109] which can get methylated to tetramethylbenzenes under MTH conditions. Acetone and CO_2 (∼0.7 %C combined selectivity) were also observed in a <1 molar ratio (∼0.5) while considering acetic acid conversion, which further validates the occurrence of acetic acid ketonization via coupling reactions followed by self-condensation of acetone resulting in the formation of aromatics.

Table 3.1: Aromatics distribution (in %C) during reactions of 0.028 bar CH_3OH (a) without and (b) with 0.0028 bar CH_3COOH cofeed on 1.7 mg HZSM-5 (Zeolyst CBV8014) at 623 K and 1023.2 mol_{CH_3OH} $(mol_{H^+}{\cdot}ks)^{-1}$.

	Toluene	Xylenes	TriMBs	TetraMBs
CH_3OH-only	10.5	58.3	31.2	0
CH_3OH + Acetic acid	8.5	46.3	36.5	8.7

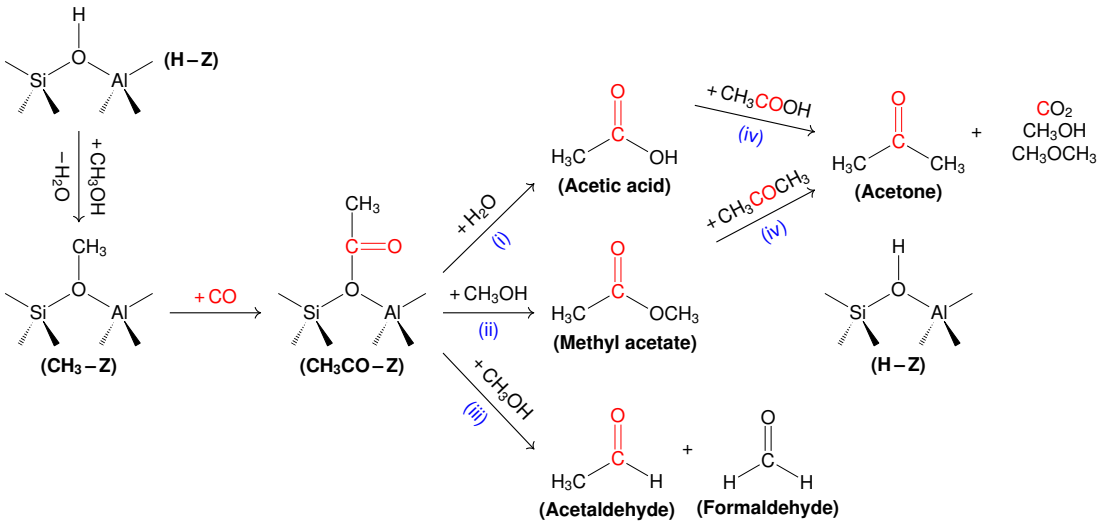

Scheme 3.1: Schematic illustrating reactions of acetyls (CH_3CO-Z) that are formed by CO insertion to surface methyls (CH_3-Z) derived from dehydration of methanol on Brønsted acid sites (H–Z). Reactions of acetyls with water [path (i)] and with methanol [path (ii)] result in the formation of acetic acid and methyl acetate, respectively, while their involvement in hydrogen transfer with methanol [path (iii)] result in the formation of acetaldehyde and formaldehyde while regenerating the acid site. Acetic acid and methyl acetate can also undergo coupling reactions to produce acetone and CO_2 alongside methanol in the case of acetic acid and dimethyl ether in the case of methyl acetate [path (iv)].

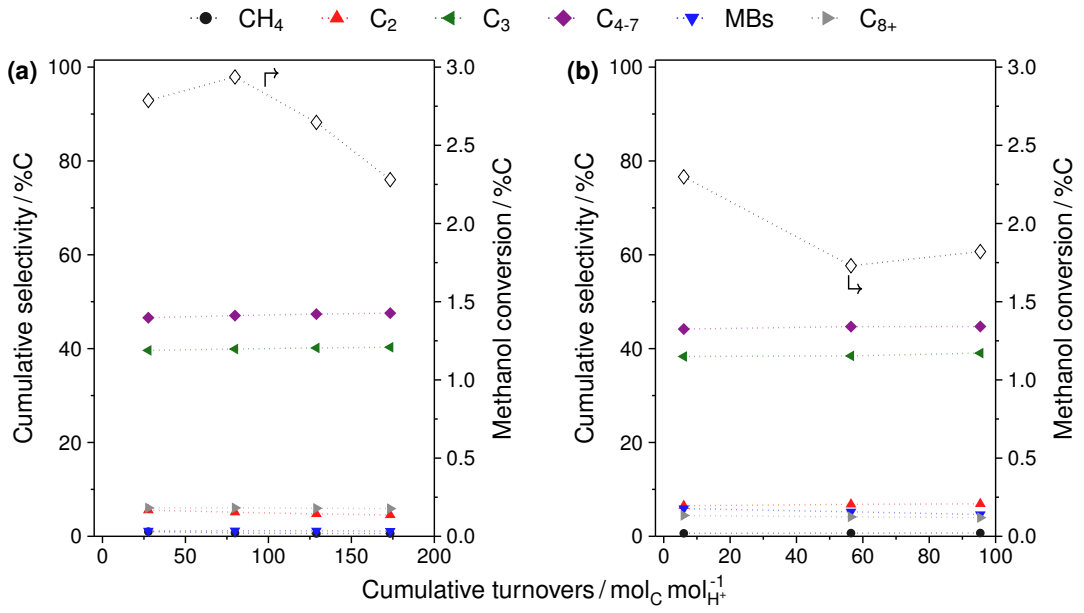

Fig. 3.3: Cumulative selectivity (*left* ordinate) and methanol conversion (*right* ordinate, ◊) versus cumulative turnovers during reactions of 0.028 bar CH_3OH (a) without and (b) with 0.0028 bar CH_3COOH cofeed on 1.7 mg HZSM-5 (Zeolyst CBV8014) at 623 K and 1023.2 mol_{CH_3OH} $(mol_{H^+} \cdot ks)^{-1}$.

3.4.3 CO and H_2O cofeeds with C_3H_6

Lastly, we also carried out independent experiments involving reactions of CO and H_2O cofeeds with propene in order to explore the possibility of Koch-type reactions involving CO insertion to olefins-derived surface species under MTH-relevant conditions. Figs. 3.4a and b show that cofeeding CO (2 bar) with propene (0.001 bar) results in no significant changes in the selectivity of C_4-C_7 olefins and aromatics compared to the case of He cofeeds at equivalent concentrations. Furthermore, the presence of excess H_2O (H_2O/C_3H_6 ~130) also did not result in any detectable formation of carboxylic acids as would be expected from hydrolysis of any acetyl species formed on the zeolite surface from co-reaction of CO and C_3H_6. These results evince that under MTH conditions, olefins likely do not undergo any direct attack by CO.

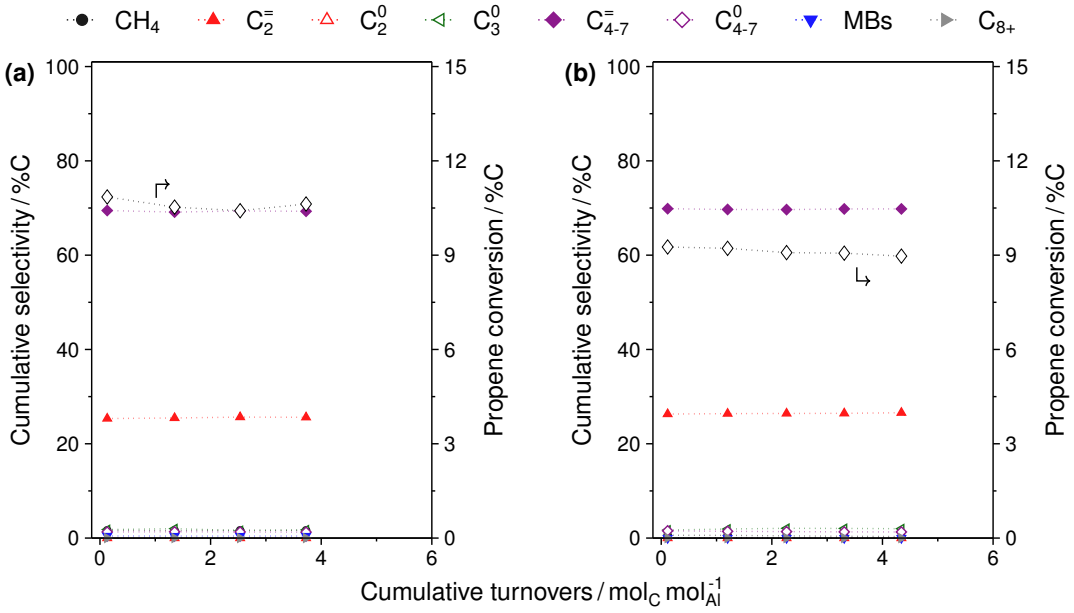

Fig. 3.4: Cumulative selectivity (*left* ordinate) and propene conversion (*right* ordinate, ◊) versus cumulative turnovers during reactions of 0.001 bar C_3H_6 and 0.013 bar H_2O with (a) 2 bar He and (b) 2 bar CO cofeeds on 5.1 mg HZSM-5 (Zeolyst CBV2314) at 673 K and 2.0 $mol_{C_3H_6}$ $(mol_{Al}\cdot ks)^{-1}$.

3.5 Conclusions

Cofeeding CO with methanol results in significant enhancements in aromatics (and ethylene) selectivity without the concomitant increase in alkanes production as expected from conventional hydrogen transfer pathways during methanol conversion. These effects are, however, short-lived and the catalyst deactivates rapidly. The addition of CO to methanol-derived surface intermediates followed by a combination of hydrogen transfer, hydrolysis, methanolysis, and ketonization steps would result in the production of aldehydes and ketones. These

carbonyl compounds can then undergo aldol condensation to generate unsaturated higher homologues that can transform to produce aromatics. Cofeeding CO with propene results in no significant effect on aromatics selectivity while cofeeding acetic acid with methanol results in a substantial increase in the aromatics selectivity, thereby providing evidence for the prolific role of acetyls derived from co-reaction of methanol and CO as key intermediates to promote aromatics production during methanol conversion with high-pressure CO cofeeds over HZSM-5, or in general, during reactions of syngas mixtures over bifunctional catalyst formulations of mixed metal oxides and zeolites.

Acknowledgements

We acknowledge (i) Dow through the University Partnership Initiative and the National Science Foundation (CBET 1701534) for financial support, and (ii) Dr. Andrzej Malek, Dr. Davy L. S. Nieskens, and Dr. Joseph DeWilde from Dow for helpful technical discussions.

Chapter 4

Lifetime improvement in methanol to olefins catalysis over chabazite materials by high pressure H_2 cofeeds

*Reported from S. S. Arora, D. L. S. Nieskens, A. Malek, A. Bhan, *Nat. Catal.* **1** (2018) 666-672 (doi.org/10.1038/s41929-018-0125-2)

4.1 Abstract

We demonstrate that catalyst lifetime in methanol-to-olefins catalysis over HSAPO-34 at sub-complete methanol conversion, as determined by the cumulative turnover capacity per Brønsted acid site towards hydrocarbon products in the effluent before complete catalyst deactivation (<15 %C final conversion), can be enhanced with increasing efficacy (∼2.8× to >70×) by cofeeding H_2 at increasing partial pressures (400 to 3000 kPa) in the influent with methanol as compared to cofeeding He at equivalent pressures. The lifetime improvement in the presence of high-pressure H_2 cofeeds is observed to be more prominent at complete methanol conversion than at sub-complete conversion. The improvements in catalyst lifetime by cofeeding H_2 are rendered without any deleterious effects on C_2-C_4 olefins selectivity which remains ∼85 %C irrespective of the inlet H_2 pressure. These observations can be rationalized based on the participation of H_2 in hydrogen transfer reactions, and in effect, interception of pathways that promote the formation of deactivation-inducing polycyclic species.

4.2 Introduction

Methanol-to-olefins (MTO) catalysis over the proton-form chabazite (CHA)-type zeotype material, HSAPO-34, is commercially deployed as a non-oil based alternative for the production of light olefins, ethene and propene [2, 3, 66, 110]. The CHA topology (with large ellipsoidal cages, 10 Å × 6.7 Å, interconnected via narrow 8-MR apertures, 3.8 Å × 3.8 Å) [98] of this silico-aluminophosphate material only allows effusion of small-chain linear molecules

[24, 25, 30, 71, 72] enabling high C_2-C_4 olefins selectivity (>85 %C) during methanol-to-olefins conversion [84, 111], however, this characteristic also renders this material susceptible to deactivation by accumulation of unreactive polycyclic aromatic compounds inside the large cages with reaction progress [15, 26, 90]. The mechanistic origins of light olefins in auto-catalytic MTO chemistry are described by the hydrocarbon pool mechanism involving olefins and aromatics as organic co-catalytic centers that act as scaffolds for C–C bond formation and scission [20, 24–26, 72]. Formaldehyde production in methanol transfer dehydrogenation events and the resulting alkylation of olefin and aromatic chain carriers by formaldehyde has been implicated in recent reports to play a critical role in initiation and termination sequences in MTO [43, 61, 63, 99, 106]. We surmise that H_2 acts as a hydrogen transfer reagent at high-pressures on zeolites/zeotypes (also reported by Meusinger and Corma [112]) and thereby, mitigates the transformation of active olefin and monocyclic aromatic organic co-catalysts in MTO to polycyclic species responsible for catalyst deactivation [26, 113, 114].

We report that cofeeding H_2 at high partial pressures (400 – 3000 kPa) with CH_3OH (13 kPa) results in orders of magnitude (∼2.8× to >70×) improvement in catalyst lifetime relative to He cofeeds at identical pressures under sub-complete conversion conditions. These improvements are afforded while maintaining the high C_2-C_4 olefins selectivity (∼85 %C) attribute of HSAPO-34, irrespective of the H_2 partial pressure in the feed with methanol. Further, varying the inlet concentration of H_2 enables selectivity control over the light olefins distribution in MTO wherein ethene-to-propene molar ratio in the effluent is noted to systematically decrease with increasing H_2 partial pressure. Cofeeding H_2 at complete methanol conversion conditions (lower space velocities) exhibits an even more pronounced effect on the cumulative turnover capacity of HSAPO-34 for MTO than at sub-complete conversion conditions. Co-processing H_2 (400 kPa and 1600 kPa) with CH_3OH over HSSZ-13—silicoaluminate analog of HSAPO-34—and HZSM-5—silicoaluminate zeolite with MFI topology—also results in improved catalyst lifetimes (∼4.5× and ∼3×, respectively) demonstrating that the beneficial effects of co-processing H_2 during MTO are prevalent regardless of the zeolite or zeotype material employed. The observed improvements in catalyst lifetime by cofeeding H_2 can be rationalized by the direct involvement of H_2 in hydrogen transfer reactions in MTO with increasing efficacy as the inlet partial pressure of H_2 increases. Specifically, we demonstrate in experiments that involve co-processing H_2 with methanol/formaldehyde mixtures that a role of H_2 is to intercept formaldehyde-mediated deactivation pathways, which consequently manifests in longer catalyst lifetimes for MTO conversion.

4.3 Methods

4.3.1 Catalyst preparation

The templated form of SAPO-34 was formulated by stirring together 8.2 g of aluminum isopropoxide ($Al(OC_3H_7)_3$) with a solution of 3.9 g of 85 wt% orthophosphoric acid in 8.4 g of deionized (DI) H_2O. Subsequently, 1.2 g of an aqueous solution of 30 wt% SiO_2 (Ludox AS-30) and 0.5 g of DI H_2O were stirred into the mixture until a homogeneous consistency was achieved. Finally, 16.8 g of an aqueous solution of 35 wt% tetraethylammonium hydroxide (TEAOH) was added to form the reaction mixture. Once formulated, the reaction mixture was placed in a stainless steel stirred Parr reactor and heated to 473 K at 0.0083 $K\,s^{-1}$. The temperature was maintained for 120 h under autogenous pressure while stirring at 60 rpm. The product was recovered by centrifugation, washed with DI H_2O, and dried at 363 K overnight.

4.3.2 Catalyst characterization

The framework type of the synthesized material was confirmed as CHA by powder X-ray Diffraction (XRD) (Fig. 4.9). The overall $(Al + P)/Si = 9.7$ atomic ratio was determined from the bulk composition obtained using X-ray Fluorescence (XRF) (Table 4.3). Measurements obtained from Inductively Coupled Plasma Atomic Emission Spectroscopy (ICP-AES) and Neutron Activation Analysis (NAA) indicated absence of any major metallic impurities in the sample (Table 4.3). The $(Al + P)/Si = 8.1$ atomic ratio in the near-surface region was determined from X-ray Photoelectron Spectroscopy (XPS) and suggests that Si is homogeneously distributed in the lattice (Fig. 4.10 for the spectra and Table 4.4 for the atomic composition). The cubic morphology and average crystallite size (∼1 µm) were characterized by Scanning Electron Microscopy (SEM) (Fig. 4.11). The Brunauer-Emmett-Teller (BET) surface area (∼554 $m^2\,g^{-1}$), and t-plot micropore volume (∼0.28 $c^3m\,g^{-1}$) were determined from N_2 adsorption-desorption at 77 K (Fig. 4.12 and Table 4.5). ^{27}Al, ^{29}Si, and ^{31}P Magic-Angle Spinning Nuclear Magnetic Resonance (MAS NMR) spectra (Table 4.6 for the experimental conditions and Fig. 4.13 for the spectra) evidenced that i) a majority of Al and P atoms were tetrahedrally coordinated in framework positions and located at sites of identical chemical environment, and ii) a majority of Si atoms were incorporated as isolated sites with tetrahedral coordination to Al atoms in framework positions. The Brønsted acid site density (∼1.1 mmol g^{-1}) was enumerated from NH_3 Temperature Programmed Desorption (TPD) (Fig. 4.14 and Table 4.7). Further characterization details are provided in Sections 4.6.6 – 4.6.12.

4.3.3 Catalytic testing

All experiments were performed in a borosilicate glass-lined stainless steel reactor tube (6.35 mm outer diameter and 4 mm inner diameter; Scientific Glass Engineering). The tubular reactor was placed inside a resistively heated furnace (Applied Test Systems, Model 3210), and the reaction temperature was measured using a K-type thermocouple (KMTXL-020U, Omega) wrapped around the reactor periphery with the tip placed near the axial-center and regulated with an electronic controller (Series 96, Watlow). The as-synthesized uncalcined SAPO-34 sieve fractions (180 – 420 µm) diluted with sand (Acros Organics) sieve fractions (150 – 420 µm; subject to a prior wash in 2 M HNO_3, deionized water rinse, and treatment in flowing dry air at 1273 K for 12 h; $\leq 0.15\,g_{cat}\,g_{sand}^{-1}$) were packed into the middle heated zone of the reactor between quartz wool plugs prior to the reactor being placed in the furnace. To avoid displacement of the catalyst under high-pressure gas flows, the remaining reactor volume was filled with quartz rods (3 mm outer diameter). Prior to every experiment, the starting catalyst material was converted to its proton form by in-situ thermal treatment in flowing dry air ($1.67\,cm^3\,s^{-1}$; Minneapolis Oxygen) at 823 K ($0.0167\,K\,s^{-1}$ ramp rate) for 6 h before being allowed to cool down to 673 K and being subject to a He ($1.67\,cm^3\,s^{-1}$; 99.997%, Minneapolis Oxygen) purge at 673 K for $\geq$ 2 h. The total gas-phase pressure during experiments was measured using a pressure transducer (0 – 6890 kPag, PX32B1-1KGV, Omega; connected to a digital reader (DP25B-E, Omega)) placed upstream of the reactor, and controlled using a back-pressure regulator (0 – 3440 kPag, 44-2300 series, Tescom) placed downstream. All gas flows including H_2 (99.999%, Matheson), He, C_3H_6 (5% in balance He, Certified Standard, Praxair), and Ar (99.9995%, Matheson) were metered using mass flow controllers (Model 5850E, Brooks). Depending on the operating conditions, liquid reagents including CH_3OH ($\geq$ 99.9%, Fluka), HCHO (16% w/v in H_2O, Pierce), deionized (DI) H_2O, or mixtures thereof were delivered either using a stainless steel syringe (Harvard Apparatus) or a glass syringe (Scientific Glass Engineering) which were driven by a PHD ULTRA™ XF syringe pump (Harvard Apparatus) or a Legato 100 syringe pump (KD Scientific), respectively. The liquids were fed and evaporated in heat traced lines (353 K), and swept by the flowing gas stream. Reactor effluent stream compositions were quantified using a gas chromatograph (Model 7890A, Agilent) equipped with a dimethylpolysiloxane HP-1 column (50 m × 320 µm × 0.52 µm) connected in parallel to a flame ionization detector and a mass spectrometer (Model 5975C, Agilent) for detecting hydrocarbons and oxygenates, and a GS-GasPro column (60 m × 320 µm) connected to a thermal conductivity detector for detecting permanent gases (H_2, Ar, and CO). The partial pressure of methanol in the feed was kept fixed at 13 kPa by feeding methanol at a constant flow rate of $0.033\,cm^3\,s^{-1}$ (gas-phase) while varying the inlet flow rate of the diluent (He or H_2) from 1 to $8\,cm^3\,s^{-1}$ and the total gas-phase pressure of the combined feed from 435 to 3035 kPa in order to achieve the desired partial pressures of the diluent (400 to 3000 kPa); Ar was used as the internal standard and its flow rate was also kept fixed at $0.056\,cm^3\,s^{-1}$

corresponding to a partial pressure of 22 kPa under the employed operating conditions for the high-pressure studies.

4.4 Results and Discussion

4.4.1 Effects of H_2 on lifetime and selectivity in MTO on HSAPO-34.

Cofeeding H_2 at increasing inlet partial pressures (400 – 3000 kPa) with CH_3OH (13 kPa) feed at sub-complete methanol conversion (calculated based on the effluent hydrocarbon products excluding dimethyl ether [DME]) results in a monotonic increase (∼2.8× to >70×) in the cumulative turnover capacity (<15 %C final conversion) of HSAPO-34 for MTO catalysis (Fig. 4.1a). The catalyst exhibits far superior performance at the highest partial pressure (3000 kPa) of H_2 cofeed employed in the study compared to lower influent H_2 concentrations and is only partially deactivated even after 130 hours on-stream. The lifetime enhancement factors calculated based on the cumulative turnovers attained when final methanol conversion levels drop below ∼50 %C and ∼15 %C with varying H_2 pressures are tabulated in Table 4.2. Contrary to the effects observed with high-pressure H_2 cofeeds, cofeeding high-pressure He at equivalent pressures is observed to have no influence on the lifetime of HSAPO-34 for methanol conversion (Fig. 4.1a) demonstrating unambiguously that the presence of H_2 is paramount for improved catalyst lifetimes in MTO. We note that any effects on the maximum conversion levels (Fig. 4.1a) owing to potential catalyst bypass at the high diluent feed rates (1 – 8 $cm^3\,s^{-1}$) relative to methanol (0.033 $cm^3\,s^{-1}$) required to achieve the desired partial pressures of the respective reagents trend in the same direction irrespective of the diluent identity, He or H_2 (Fig. 4.5); the observed decrease in maximum conversion levels with increasing H_2 pressures is therefore unrelated to catalyst lifetime.

Figs. 4.1b and 4.1c present the effects of varying the inlet partial pressures of He versus H_2 cofeeds, respectively, on the cumulative selectivity of different hydrocarbon products observed in the effluent stream during MTO over HSAPO-34. Cumulative selectivity represents the fractional amount of methanol/DME derived carbon atoms observed in a particular product to the total amount observed in all effluent products ($C_1 - C_{6+}$) over the catalyst lifetime. With the exception of the study involving 3000 kPa H_2 cofeed, C_2 selectivity is observed to monotonically decrease (31.9 %C to 27.4 %C) while the combined selectivity of C_3 and C_4 is observed to monotonically increase (62.3 %C to 66.3 %C) with increasing influent H_2 partial pressure (0 – 1600 kPa); C_{5+} selectivity is observed to exhibit no discernible trend and remains invariant (∼5 %C) with H_2 partial pressure. The lower combined selectivity to $C_3 - C_4$ fractions and higher C_{5+} selectivity in the study with 3000 kPa H_2 cofeed relative to lower partial pressures of H_2 can be rationalized as a consequence of lower extent of olefin interconversion reactions at the high conversion levels noted over the entire span of reaction progress. Further, cumulative CH_4 selectivity is observed to monotonically increase (0.49 %C to 1.57 %C) with increasing P_{H_2} (0 – 3000 kPa), however, the cumulative C_1 selec-

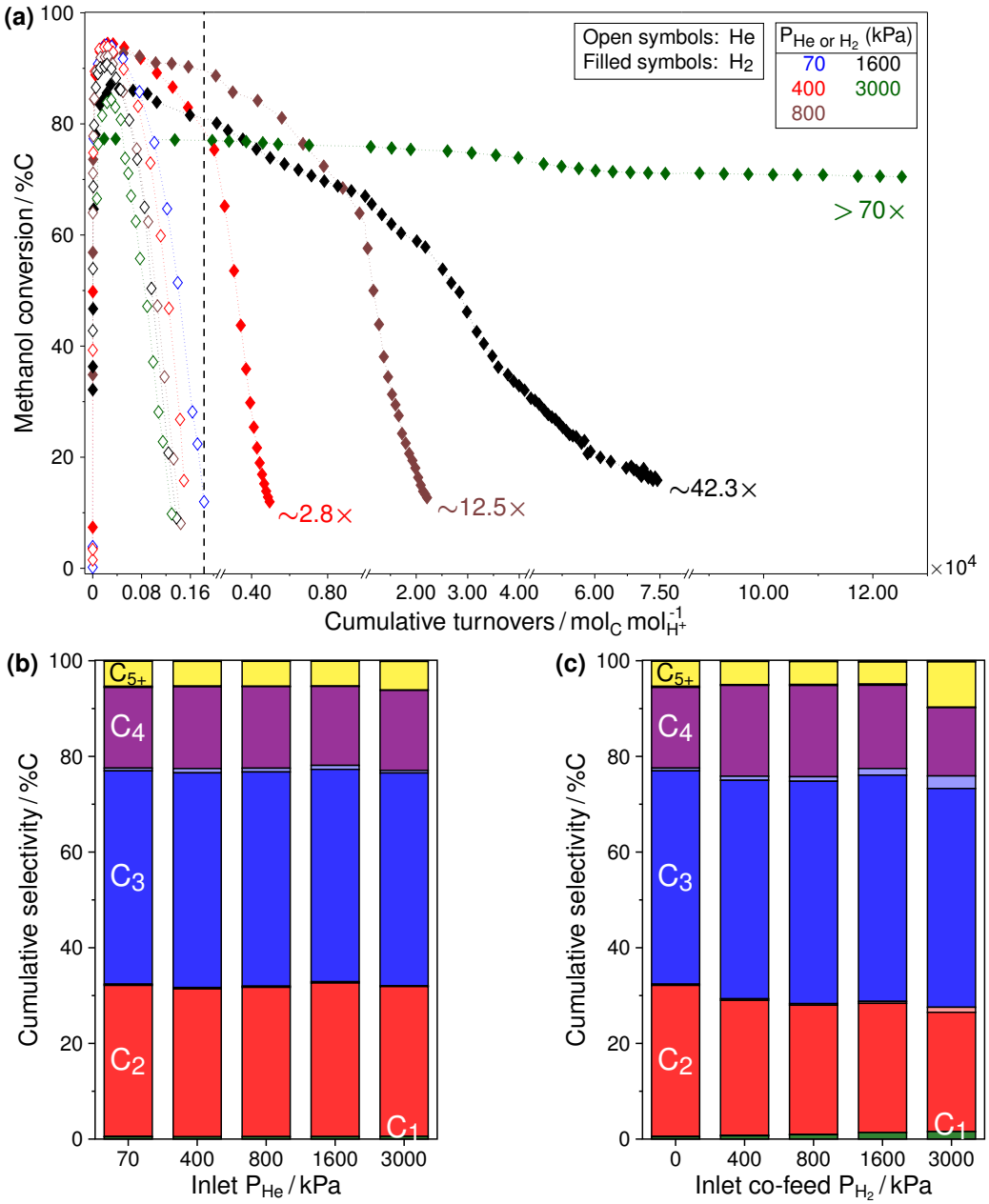

Fig. 4.1: (a) Methanol conversion profiles versus cumulative turnovers observed with varying He (empty symbols) or H_2 (filled symbols) cofeeds; (b), (c) Cumulative selectivity versus inlet partial pressures of (b) He or (c) H_2 cofeeds during methanol feed on 4 mg HSAPO-34 at 673 K, 13 kPa CH_3OH, 70 kPa He ($\equiv$ 0 kPa H_2) – 3000 kPa He; 400 – 3000 kPa H_2, 40 $g_{CH_3OH}\, g_{cat}^{-1}\, h^{-1}$. (a) The vertical dashed line denotes the cumulative turnover capacity of HSAPO-34 for methanol conversion with helium cofeed at 70 kPa, which is used to calculate the relative lifetime improvement factors (listed at the end of the lines with filled symbols) with different H_2 cofeeds; (b), (c) The dark- and light-shaded regions represent olefinic and paraffinic fractions of the respective carbon group listed in the dark bars.

tivity (including CH_4 and CO) is $< 1.6\,\%C$ at all H_2 partial pressures which is insignificant compared to the selectivity of C_2-C_4 fractions ($\sim$85 %C). The observed monotonic trends in selectivity with varying H_2 cofeeds are in contrast to the case of He cofeeds at equivalent conditions where no such perceptible trends are noted.

Table 4.1 presents the effects of varying H_2 partial pressure on the ethene-to-propene molar ratio (E/P), and olefins-to-paraffins molar ratio (O/P) in the effluent hydrocarbon product stream. E/P represents the ratio of the total molar amount of ethene to the total molar amount of propene, and O/P represents the ratio of the total molar amount of C_2-C_{6+} olefins to the total molar amount of C_1-C_{6+} paraffins, including CH_4, observed over the catalyst lifetime. The monotonic decrease in E/P (1.06 to 0.82) with increasing H_2 partial pressure (0 – 3000 kPa) suggests suppressed rates of propagation of the aromatics-based cycle over its olefins-based counterpart as ethene is predominantly formed in aromatics-based methylation and dealkylation events during MTO on HSAPO-34 [36, 115]. O/P also monotonically decreases (40.5 to 10.8) with increasing H_2 partial pressure (0 – 3000 kPa) but exceeds 10 even at the highest co-fed pressure of H_2 evidencing that the effluent product stream, dominated by C_2-C_4 fractions, is mostly composed of olefins and that co-processing H_2 does not disrupt the high light olefin selectivity characteristic of HSAPO-34 in MTO. In comparison, cofeeding He at equivalent pressures has no effect on both E/P and O/P.

Table 4.1: Ethene-to-propene (E/P) and olefins-to-paraffins (O/P) molar ratios with He versus H_2 cofeeds during methanol conversion on 4 mg HSAPO-34 at 673 K, 13 kPa CH_3OH, 70 kPa He ($\equiv$ 0 kPa H_2) – 3000 kPa He; 400 – 3000 kPa H_2, 22 kPa Ar, 40 $g_{CH_3OH}\,g_{cat}^{-1}\,h^{-1}$.

Cofeed	**He**					**H_2**				
Partial pressure (kPa)	70	400	800	1600	3000	0	400	800	1600	3000
E/P	1.06	1.03	1.05	1.08	1.06	1.06	0.93	0.87	0.86	0.82
O/P	40.5	36.2	38.3	37.1	41.0	40.5	29.4	23.5	16.1	10.8

The relative improvement in the cumulative turnover capacity of HSAPO-34 for MTO with increasing H_2 partial pressure is more significant and more pronounced (>10× versus $\sim$2.8× with 400 kPa H_2 cofeed, and >25× versus $\sim$12.5× with 800 kPa H_2 cofeed; Figs. 4.2a and 4.1a) at complete methanol conversion conditions or equivalently, at lower methanol space velocities (6 $g_{CH_3OH}\,g_{cat}^{-1}\,h^{-1}$ versus 40 $g_{CH_3OH}\,g_{cat}^{-1}\,h^{-1}$). This is likely an effect of lower averaged methanol concentration along the catalyst bed at lower space velocities that results in lower overall rates of transfer dehydrogenation of methanol which consequently manifests in a lower concentration of formaldehyde—implicated to induce catalyst deactivation [43, 61, 62, 116]. Moreover, analogous to the sub-complete conversion results, C_2-C_4 olefins remain dominant while C_2 selectivity is observed to monotonically decrease (36.9 %C to 28.8 %C) and the combined selectivity of C_3 and C_4 fractions is observed to

monotonically increase (57.5 %C to 64.5 %C) with increasing influent H_2 partial pressure (0 – 800 kPa) (Fig. 4.2b).

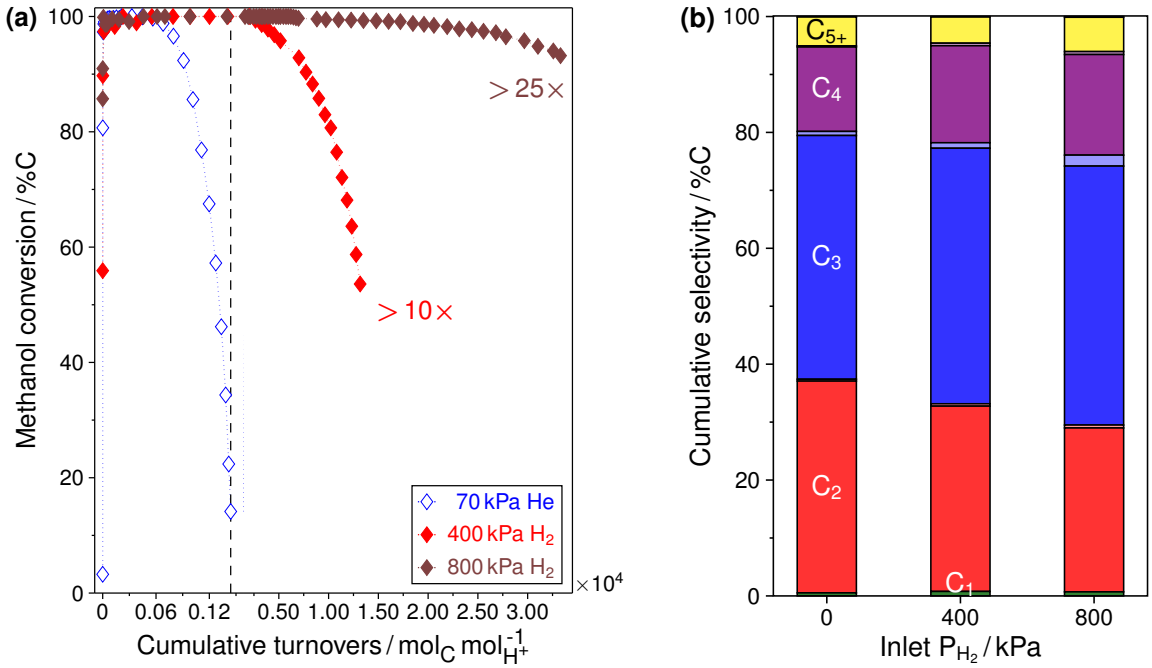

Fig. 4.2: (a) Methanol conversion profiles versus cumulative turnovers observed with varying He (empty symbols) or H_2 (filled symbols) cofeeds, and (b) Cumulative selectivity versus inlet partial pressures of H_2 cofeeds during methanol conversion on 27 mg HSAPO-34 at 673 K, 13 kPa CH_3OH, 0 kPa H_2 ($\equiv$ 70 kPa He) – 800 kPa H_2, 6 $g_{CH_3OH}\, g_{cat}^{-1}\, h^{-1}$. (a) The vertical dashed line denotes the cumulative turnover capacity of HSAPO-34 for methanol conversion with helium cofeed at 70 kPa, which is used to calculate the relative lifetime improvement factors (listed at the end of the lines with filled symbols) with different H_2 cofeeds; (b) The dark- and light-shaded regions represent olefinic and paraffinic fractions of the respective carbon group listed in the dark bars.

4.4.2 Effects of H_2 on MTO performance of zeolites other than HSAPO-34.

HSSZ-13, the silicoaluminate analog of HSAPO-34, also exhibits enhanced MTO lifetime (~4.5×) in the presence of high-pressure H_2 cofeeds (400 kPa) while maintaining high overall light olefins selectivity (>85 %C) at sub-complete conversion conditions (Fig. 4.6) evidencing that cofeeding H_2 results in longer catalyst lifetimes for MTO conversion irrespective of the identity of the chabazite material employed. HZSM-5, an silicoaluminate material with MFI framework type, also exhibits a significant increase in lifetime (~3×) for methanol conversion in the presence of high-pressure H_2 cofeeds (1600 kPa) while retaining high olefinic content (78.1 %C) in the predominant product groups, $C_2 - C_7$ (Fig. 4.3). The detailed physical and chemical characteristics of the HZSM-5 sample used in this study are reported in Chapter 2. These demonstrations clearly validate applicability of the proposed strategy of cofeeding high-pressure H_2 to enhance catalyst lifetime during methanol conversion over

zeolite materials diverse in composition and topology.

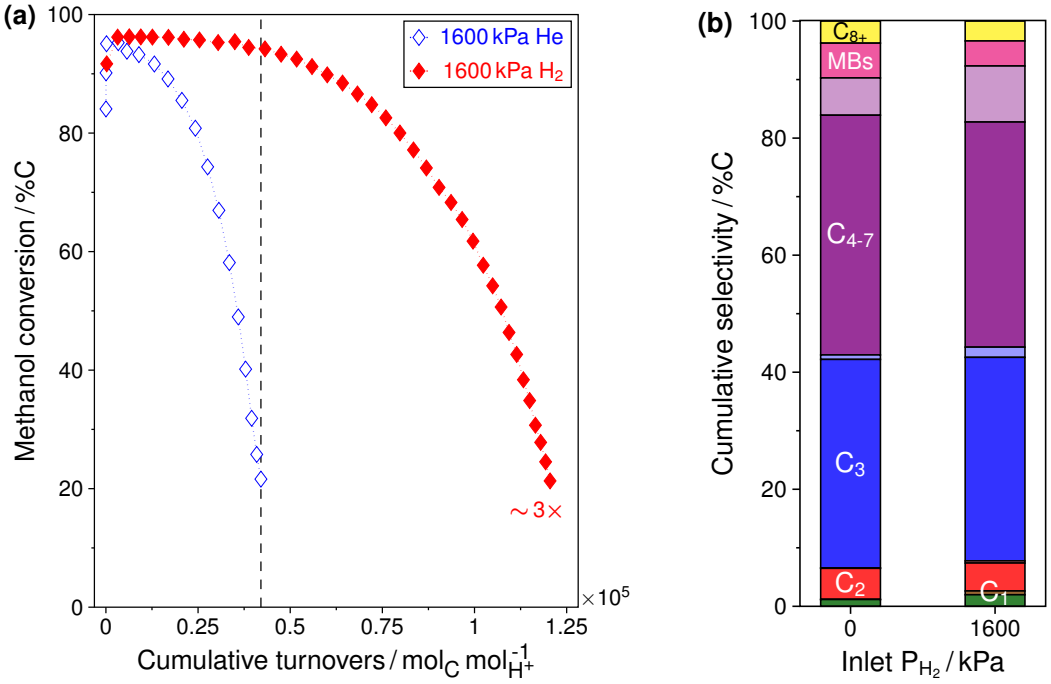

Fig. 4.3: (a) Methanol conversion profiles versus cumulative turnovers observed with He (empty symbol) or H_2 (filled symbol) cofeeds, and (b) Cumulative selectivity versus inlet partial pressures of H_2 cofeeds with methanol on 5 mg HZSM-5 at 723 K, 13 kPa CH_3OH, 0 kPa H_2 ($\equiv$ 1600 kPa He) – 1600 kPa H_2, 32.1 $g_{CH_3OH}\ g_{cat}^{-1}\ h^{-1}$. (a) The vertical dashed line denotes the cumulative turnover capacity of HZSM-5 for methanol conversion with helium cofeed at 1600 kPa, which is used to calculate the relative lifetime improvement factors (listed at the end of the lines with filled symbols) with different H_2 cofeeds; (b) The dark- and light-shaded regions represent olefinic and paraffinic fractions of the respective carbon group listed in the dark bars, and 'MBs' represents methyl-substituted benzenes.

4.4.3 Mechanistic basis for H_2 cofeed effects in MTO.

We surmise that the observed improvements in the total turnover capacity of zeolites/zeotypes for MTO conversion by co-processing H_2 likely result from the participation of H_2 in hydrogen transfer reactions with increasing efficacy as the partial pressure of H_2 in the feed increases. Zeolites/zeotypes are lesser known hydrogenation catalysts relative to metal-based formulations, however, both the ability of H_2 to facilitate hydrogen transfer at high-pressures [117–119], and the reversibility of monomolecular alkane dehydrogenation at atmospheric pressure on proton-form zeolites [120] have been documented in the literature. We evidenced the ability of H_2 to participate in hydrogen transfer events in independent studies involving reactions of propene-H_2 mixtures over HSAPO-34 at MTO-relevant conditions. Co-processing H_2 (400 – 1600 kPa) with propene (2.2 kPa) results in a monotonic increase in both the cumulative turnover capacity of HSAPO-34 for propene conversion

and the cumulative propane selectivity (Fig. 4.7), consistent with the observed increase in catalyst lifetime and decrease in O/P during MTO catalysis. Further, catalyst lifetime in MTO has been shown to correlate with average methanol partial pressure in recent reports demonstrating higher catalyst lifetime when using (i) DME versus methanol as feedstock over different zeolite or zeotype catalysts [62, 63, 80], (ii) continuous stirred tank reactors versus packed bed reactor configurations for methanol conversion over HZSM-5 [60], and (iii) low inlet methanol partial pressures or high contact times for methanol conversion over HSAPO-34 [43]. Methanol partial pressure plays a critical role in controlling the extent of transfer dehydrogenation events involving methanol that result in the production of formaldehyde in reference to methylation events involved in carbon chain-growth during MTO [43, 99]. Formaldehyde is purportedly involved in Prins condensation reactions with olefins and aromatics resulting in the transformation of active organic co-catalytic species to inactive polycyclic aromatic species [43, 61–63]. We demonstrate that co-processing H_2 (400 kPa) with a mixed feed of CH_3OH (13 kPa) and HCHO (13 Pa) on HSAPO-34 also results in improved catalyst lifetime relative to the case of co-processing He at equivalent pressures (Fig. 4.4). This observation suggests that a likely role of H_2 in MTO, among possible others, is to intercept formaldehyde-mediated alkylation reactions that catalyze the formation of polycyclic aromatic compounds responsible for loss of catalytic activity. An independent study involving chromatographic analysis of the occluded organic species extracted from spent HSAPO-34 samples at sub-complete methanol conversion suggests that cofeeding high-pressure H_2 does not significantly alter the composition of carbon-containing species retained in the catalyst at complete deactivation (Fig. 4.8). The composition of the extracts in all studies, irrespective of P_{H_2}, is typical of MTO conversion without any H_2 cofeeds over HSAPO-34 reported in the literature wherein pyrenes are observed to be the dominant species in the spent catalysts [114, 115].

Relative to existing strategies for improving MTO lifetime including the introduction of water cofeeds [44, 121], changing process parameters such as feed methanol pressure and contact-time [43, 116], and material parameters such as crystallite size [122, 123], acid site density [114, 124], introduction of mesoporous domains [52], incorporation of rare earth metal oxides or pure metals and/or their cations [125–127], co-processing H_2 is effective in enhancing the cumulative turnover capacity while sustaining high light olefins selectivity, typical of CHA-type zeolite/zeotype formulations. Our observations in this report also explain the observed stable time-on-stream behavior of physical mixtures of metal oxide catalysts and HSAPO-34 for high-pressure reactions of CO/H_2 or CO_2/H_2 mixtures for light olefins/paraffins production [128–132].

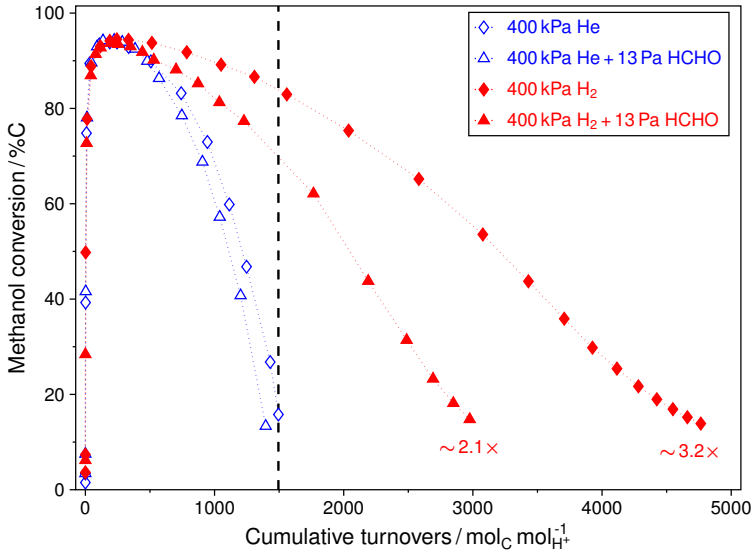

Fig. 4.4: Methanol conversion profiles versus cumulative turnovers during MTO with cofeeds of He, H_2, HCHO, or mixtures thereof on 4 mg HSAPO-34 at 673 K, 13 kPa CH_3OH, 13 Pa HCHO ($+110$ Pa H_2O), 400 kPa He, 400 kPa H_2, 40 $g_{CH_3OH}\, g_{cat}^{-1}\, h^{-1}$. The vertical dashed line denotes the cumulative turnover capacity of HSAPO-34 for methanol conversion with He cofeed at 400 kPa, which is used to calculate the relative lifetime improvement factors (listed at the end of the lines with filled symbols) when co-processing H_2 or H_2/HCHO mixtures.

4.5 Conclusions

We demonstrate that co-processing H_2 at high-pressures with CH_3OH over CHA-type zeolite/zeotype catalyst formulations results in marked improvements in catalyst lifetime (>70×) while preserving the high light olefins selectivity characteristic of these materials during MTO conversion. In independent studies, cofeeding high-pressure H_2 is shown to result in i) enhanced formation of propane from propene feeds over HSAPO-34, and ii) enhanced MTO lifetime of HSAPO-34 in the case of co-reacting CH_3OH and HCHO, thereby suggesting that H_2 participates in hydrogen transfer reactions and in effect, intercepts alkylation chemistries mediated by HCHO which otherwise result in the transformation of active co-catalytic hydrocarbon pool species to polycyclic aromatic compounds that engender catalyst deactivation during MTO catalysis.

Acknowledgements

Dr. Davy L. S. Nieskens and Dr. Andrzej Malek from Dow conceptualized the research effort. Dr. Andrzej Malek synthesized and provided the SAPO-34 sample used in the study. We acknowledge (i) Dow through the University Partnership Initiative and the National Science Foundation (CBET 1701534) for financial support, (ii) Dr. Seema Thakral and Dr. Bing Luo from the Characterization Facility, University of Minnesota, which receives partial

support from the National Science Foundation through the Materials Research Science and Engineering Centers program, for providing the X-ray diffraction and X-ray photoelectron spectroscopy data, respectively, (iii) Dr. Tanya Whitmer from the Ohio State University for providing the nuclear magnetic resonance spectroscopy data, (iv) Dow, Analytical Science, Midland and Terneuzen for providing the quantitative elemental analysis, scanning electron microscopy, and extracts analysis data, (v) Dr. Dean M. Millar from Dow for synthesizing and providing the SSZ-13 sample used in the study, and (vi) Dr. Joseph F. DeWilde from Dow for helpful technical discussions.

4.6 Supplementary Information

4.6.1 Effects of H_2 cofeeds on the relative increase in the cumulative turnover capacity at sub-complete conversion during MTO on HSAPO-34

Table 4.2 tabulates the relative increase in the cumulative turnover capacity of HSAPO-34 enumerated when final methanol conversion drops below ∼50 %C and ∼15 %C at sub-complete methanol conversion conditions.

Table 4.2: Relative increase in the cumulative turnover capacity of HSAPO-34 for MTO calculated at different final conversion levels.

Final conversion level / %C	**Inlet cofeed P_{H_2} / kPa**				
	0	400	800	1600	3000
∼50	1	2.2	8.5	22.8	>70×
∼15	1	2.8	12.5	42.3	>70×

4.6.2 Effects of He versus H_2 cofeeds on the maximum conversion levels attained at sub-complete conversion during MTO over HSAPO-34

Fig. 4.5 compares methanol conversion profiles at early turnovers (near the maximum conversion region) observed with He cofeed at 70 kPa versus He or H_2 cofeeds at high partial pressures (400 – 3000 kPa) with 13 kPa methanol feed. It is evident that any effects on the maximum conversion levels owing to potential catalyst bypass at the high diluent feed rates (1 – 8 $cm^3\,s^{-1}$) relative to methanol (0.033 $cm^3\,s^{-1}$)—required to achieve the desired partial pressures of methanol and diluent—trend in the same direction irrespective of the diluent identity, He or H_2.

4.6.3 Effects of H_2 cofeeds on MTO performance of HSSZ-13

The cumulative turnover capacity of HSSZ-13—silicoaluminate analog of HSAPO-34—is augmented by a factor of ∼4.5 when co-processing H_2 at 400 kPa versus He at 86 kPa with

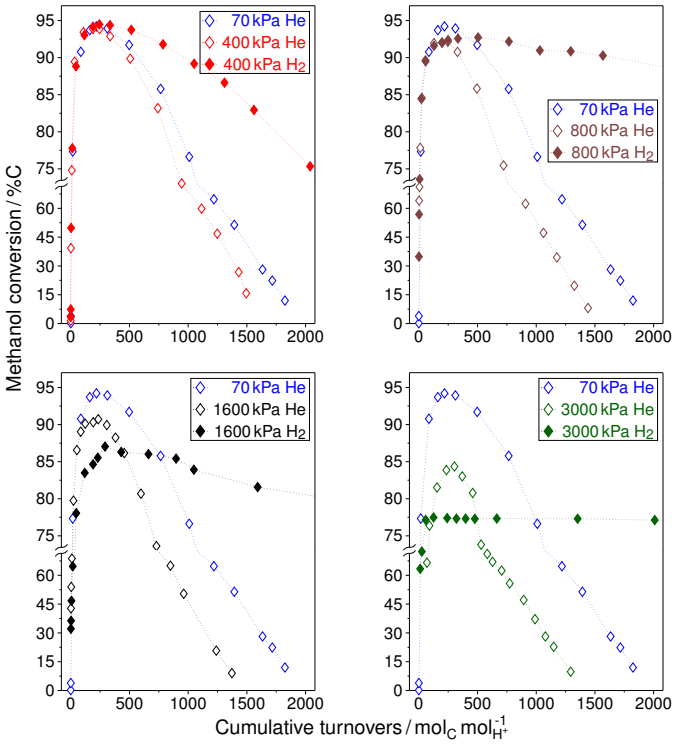

Fig. 4.5: Methanol conversion profiles at early turnovers observed with varying He (empty symbols) or H_2 (filled symbols) cofeeds at sub-complete methanol conversion on 4 mg HSAPO-34 at 673 K, 13 kPa CH_3OH, 70 – 3000 kPa He, 400 – 3000 kPa H_2, 40 g_{CH_3OH} g_{cat}^{-1} h^{-1}.

13 kPa CH_3OH feed at 673 K (Fig. 4.6a). $C_2 - C_4$ olefins remain dominant, and similar to the trends observed during methanol conversion over HSAPO-34, C_2 selectivity is noted to decrease at the expense of $C_3 - C_4$ in the presence of H_2 versus He cofeed (Fig. 4.6b).

4.6.4 Effects of H_2 cofeeds on propene conversion on HSAPO-34

Independent experiments involving co-processing H_2 with C_3H_6 over HSAPO-34 were performed under MTO-relevant conditions to further understand the role of H_2 in MTO conversion. Increasing the inlet partial pressure of H_2 (400 – 1600 kPa) with propene (2.2 kPa) feed over HSAPO-34 resulted in a monotonic increase in i) the the cumulative number of turnovers, and ii) the cumulative selectivity of propane at 210 minutes on stream (Fig. 4.7), evidencing the role of H_2 as a hydrogen transfer reagent over HSAPO-34.

4.6.5 Effects of H_2 cofeeds on the composition of carbonaceous deposits on spent HSAPO-34

Dissolution experiments were performed following a procedure analogous to the one detailed by Arstad and Kolboe [30] to ascertain the nature of carbon-containing species retained in

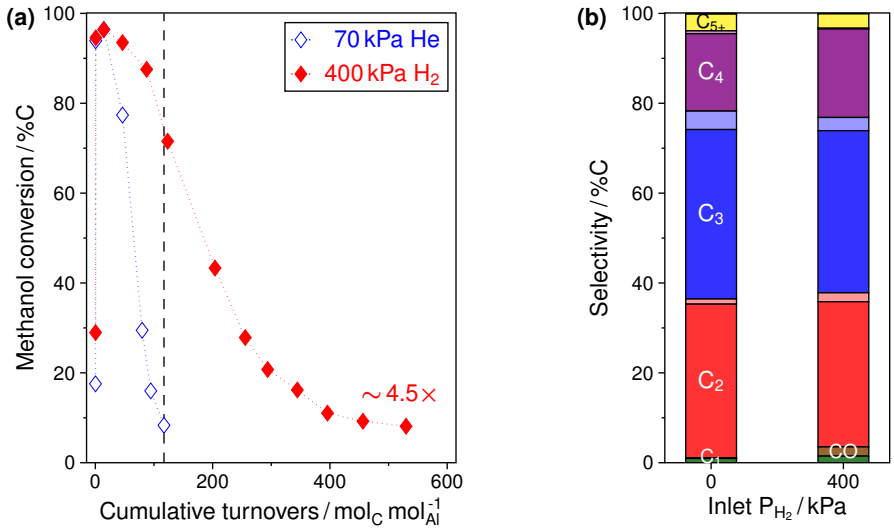

Fig. 4.6: (a) Methanol conversion profiles versus cumulative turnovers observed with He (empty symbol) or H_2 (filled symbol) cofeeds, and (b) Cumulative selectivity versus inlet partial pressures of H_2 cofeeds during methanol conversion on 10.5 mg HSSZ-13 (Si/Al = 10) at 673 K, 13 kPa CH_3OH, 0 kPa H_2 (≡ 86 kPa He) or 400 kPa H_2, 34.1 $g_{CH_3OH}\ g_{cat}^{-1}\ h^{-1}$. (a) The vertical dashed line denotes the cumulative turnover capacity of HSSZ-13 for methanol conversion with helium cofeed at 70 kPa, which is used to calculate the relative lifetime improvement factors (listed at the end of the lines with filled symbols) with H_2 cofeed; (b) The dark- and light-shaded regions represent olefinic and paraffinic fractions of the respective carbon group listed in the dark bars.

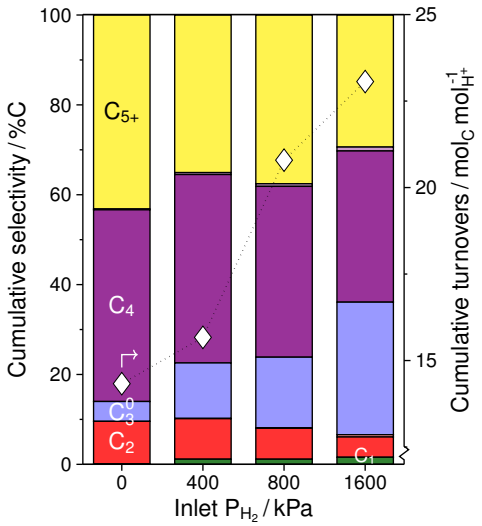

Fig. 4.7: Cumulative selectivity (*left* ordinate) and Cumulative turnovers (*right* ordinate, ◊) attained at 210 minutes on stream with varying H_2 cofeeds with propene on 27 mg HSAPO-34 at 673 K, 2.2 kPa C_3H_6, 0 kPa H_2 (≡42 kPa He); 400 – 1600 kPa H_2, 1.1 $g_{C_3H_6}\ g_{cat}^{-1}\ h^{-1}$. The dark- and light-shaded regions represent olefinic and paraffinic fractions of the respective carbon group listed in the dark bars.

the spent HSAPO-34 samples obtained after methanol conversion with varying H_2 cofeeds at sub-complete conversion. In a typical experiment, the catalyst sample was removed from the reactor tube soon after (∼2 minutes) the feed was turned off, and transferred to a screw-cap Teflon vial followed by dissolution in 1 mL of 1 M HCl solution (Laboratory Reagent, VWR) overnight. After the acid dissolution, 1 mL of 1 M NaOH solution (prepared by dissolving ∼0.85 g of NaOH pellets (Certified ACS, Fischer Scientific) in ∼20 g of deionized water) was added to neutralize the acid. 1 mL of CH_2Cl_2 (HPLC Plus, Sigma-Aldrich) solution (with 0.15 wt% C_2Cl_6 (99%, Sigma-Aldrich) added as an internal standard) was added to the resulting solution to extract the liberated organic molecules from the water phase. The organic and water phases were allowed to separate overnight and the CH_2Cl_2 phase was subject to chromatographic analysis. The concentrations (in ppm wt.) of different organic species observed with varying H_2 cofeeds are presented in Fig. 4.8.

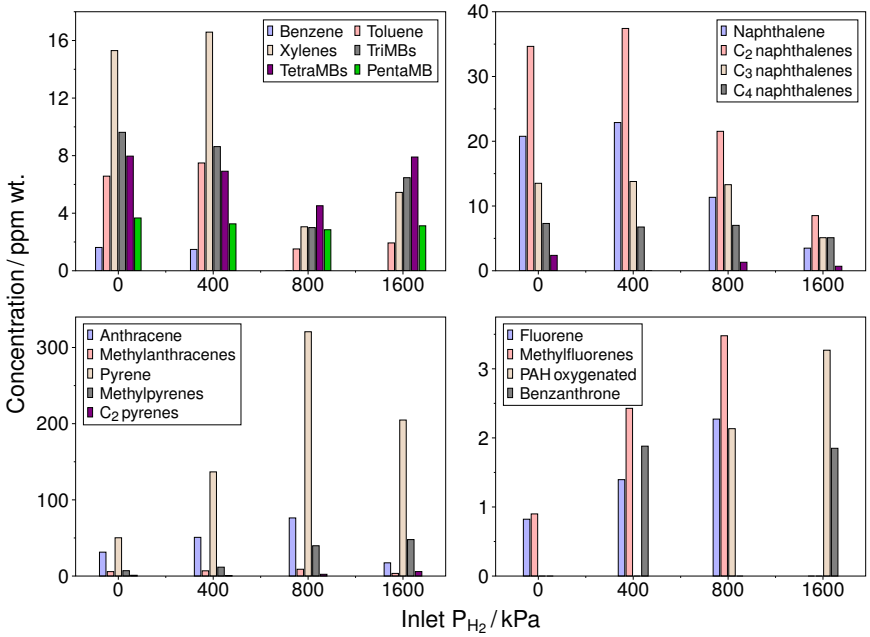

Fig. 4.8: Concentrations (in ppm wt.) of various carbonaceous species observed during chromatographic analysis of the organic extracts obtained on dissolution of spent HSAPO-34 samples after MTO with varying H_2 cofeeds at sub-complete methanol conversion.

4.6.6 X-ray Diffraction

The powder X-ray diffraction pattern of the as-synthesized uncalcined SAPO-34 sample was recorded on a Bruker D8 DISCOVER diffractometer using Cu-K_α ($\lambda = 1.54$ Å) as the radiation source. The observed pattern confirmed the framework type as CHA (reference material ICDD #98-002-0692) [133, 134] and indicated that no major impurity phases were present in the material (Fig. 4.9).

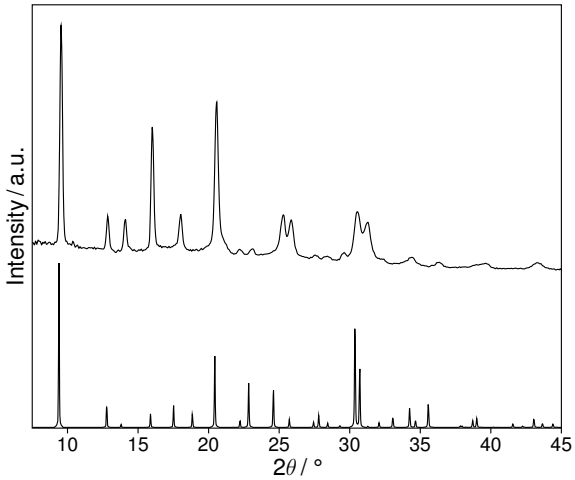

Fig. 4.9: Powder X-ray diffraction pattern of the as-synthesized uncalcined SAPO-34 sample (*top*) and the reference CHA material [ICDD #98-002-0692] (*bottom*).

4.6.7 Elemental Analysis

The overall $(Al + P)/Si = 9.7$ atomic ratio of the as-synthesized uncalcined SAPO-34 sample was determined from quantitative elemental analysis obtained using X-ray Fluorescence (XRF) (Table 4.3). Measurements obtained from Inductively Coupled Plasma – Atomic Emission Spectroscopy (ICP-AES) and Neutron Activation Analysis (NAA) indicated the absence of any major metallic impurities in the sample.

Table 4.3: Bulk elemental composition of the as-synthesized uncalcined SAPO-34 sample determined from XRF, ICP-AES, and NAA measurements.

Elemental composition					
XRF (wt%)		**ICP-AES (ppm)**		**NAA (ppm)**	
Al	21.89 ± 0.13	Ca	16.53	Mo	2.1 ± 0.4
Si	4.32 ± 0.15	Cr	20.27	Ni	120 ± 50
P	21.52 ± 0.11	Fe	30.41	Fe	<300
		Zn	54.14	Zn	10 ± 2
		Ti	0.01		
		Cu	45.51		

4.6.8 X-ray Photoelectron Spectroscopy

X-ray photoelectron spectrum (XPS) of the as-synthesized uncalcined sample was recorded on a PHI Versa Probe III instrument using a monochromated Al K_α X-ray source (1486.6 eV) (Fig. 4.10). The $(Al + P)/Si = 8.1$ atomic ratio in the near-surface region was calculated from the atomic percentages (Table 4.4) obtained from the survey spectra using the Mul-

tipak Software provided with the XPS instrument. For high resolution data, the lowest binding-energy C1s peak (presumably, C−C/C−H peak) was set at 285.0 eV and was used as a reference.

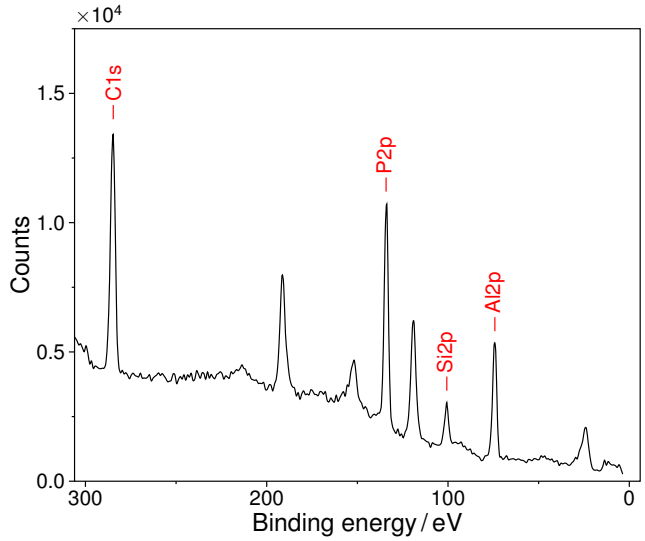

Fig. 4.10: XPS of the as-synthesized uncalcined SAPO-34 sample obtained using a monochromated Al K_α X-ray source.

Table 4.4: Al, Si, and P concentrations in the near-surface region of the as-synthesized uncalcined SAPO-34 sample.

	Atomic %
Al	9.0
Si	2.2
P	8.9

4.6.9 Scanning Electron Microscopy

The scanning electron microscopy (SEM) images (Fig. 4.11) of the as-synthesized uncalcined sample were used to characterize the cubic crystal morphology and ascertain the average crystallite size (∼1 µm).

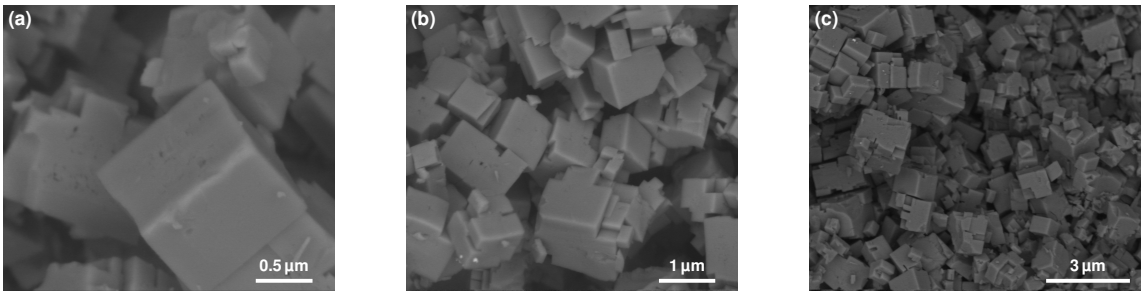

Fig. 4.11: SEM images of the as-synthesized uncalcined SAPO-34 sample at different magnification levels.

4.6.10 N_2 Physisorption

N_2 physisorption measurements were obtained on a Micromeritics ASAP 2020 system. The as-synthesized uncalcined SAPO-34 sample was treated in dry air flow at 823 K (0.0167 K s^{-1})

for 6 h in order to obtain the de-templated form prior to being subject to degassing (initial evacuation to <10 µmHg at 363 K followed by heat treatment at 723 K [0.0167 K s^{-1}] for 4 h), and N_2 adsorption-desorption at 77 K. The BET surface area and t-plot micropore volume values obtained from the resulting isotherms (Fig. 4.12) are presented in Table 4.5, and are typical of silicoaluminophosphates [5, 135].

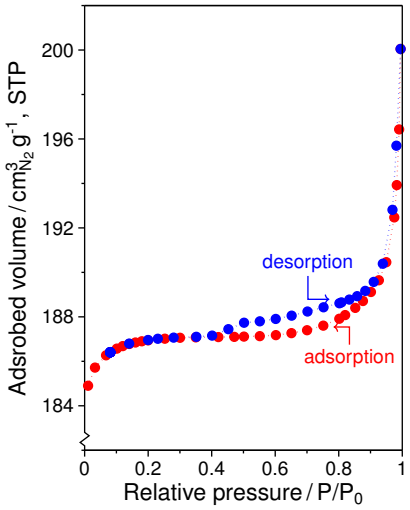

Fig. 4.12: N_2 physisorption isotherms of calcined SAPO-34 sample.

Table 4.5: Textural properties of calcined SAPO-34 sample obtained from the N_2 adsorption and desorption isotherms presented in Fig. 4.12.

Surface area (m^2 g^{-1})	554
Micropore volume (cm^3 g^{-1})	0.28

4.6.11 Magic-Angle Spinning Nuclear Magnetic Resonance Spectroscopy

The ^{27}Al, ^{29}Si, and ^{31}P Magic-Angle Spinning Nuclear Magnetic Resonance (MAS NMR) spectra of the as-synthesized uncalcined SAPO-34 sample were recorded on a AVIIIHD Bruker 600 MHz wide-bore NMR spectrometer equipped with a 3.2 mm HXY MAS probe. The experimental conditions for all the measurements are summarized in Table 4.6. The

Table 4.6: Experimental conditions for MAS NMR measurements of the as-synthesized uncalcined SAPO-34 sample. The flip angle for all measurements was $\pi/4$.

Nucleus	Resonance frequency (MHz)	Pulse duration (µs)	Repetition time (s)	MAS frequency (kHz)	Scans	Reference (external)
^{27}Al	156.4	3	0.25	15	256	Na_3AlF_6
^{29}Si	119.3	6.25	120	10	2048	$(CH_3)_4Si$
^{31}P	243.0	4	10	15	128	H_3PO_4, 85 wt%

chemical shifts observed at 40.1 ppm (Fig. 4.13a) and -28.5 ppm (Fig. 4.13c) in the ^{27}Al and ^{31}P NMR spectra, respectively, are typical of tetrahedral coordination in framework locations of aluminophosphate materials [136–139]. The presence of only a single major resonance line in both spectra indicates that a majority of Al and P atoms are located at

sites of identical chemical environment. The signal at 13.7 ppm in the ^{27}Al NMR is ascribed to Al atoms present in the framework interacting additionally with either the template or water present in the as-synthesized uncalcined sample because as reported by Vomscheid et al. [139], a similar peak in the ^{27}Al NMR spectra of their as-synthesized uncalcined SAPO-34 sample was observed to disappear after subjecting the sample to a calcination treatment at 823 K prior to collecting the NMR data. The small and symmetrical resonance lines observed at 33.1 and -90.5 ppm in the ^{31}P NMR (4.13c) are characterized as spinning sidebands.

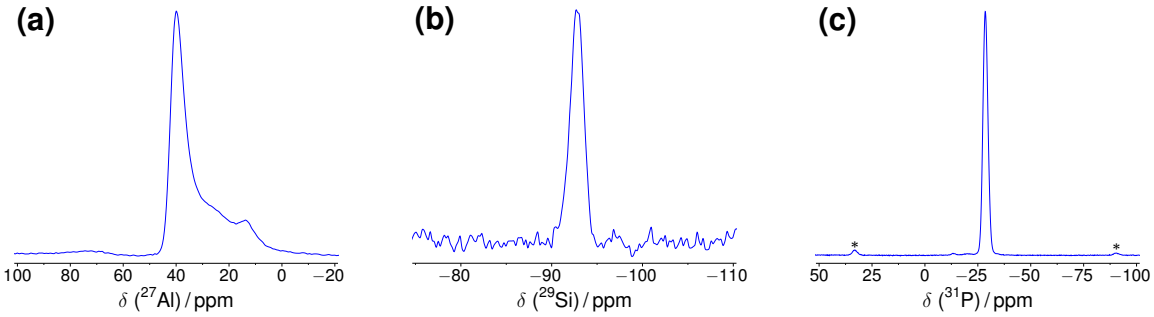

Fig. 4.13: (a), (b), and (c) showing ^{27}Al, ^{29}Si, and ^{31}P MAS NMR spectra, respectively of the as-synthesized uncalcined SAPO-34 sample. Asterisks (∗) in (c) denote spinning sidebands.

The resonance line at −92.7 ppm observed in the ^{29}Si NMR spectra (Fig. 4.13a) is attributed to silicon atoms bonded via oxygens to four aluminum atoms [136–139]; the absence of any other major spectral features indicates that a majority of Si atoms are incorporated as isolated sites.

4.6.12 NH_3 Temperature Programmed Desorption

The enumeration of the acid site density of the HSAPO-34 sample was done by performing NH_3 Temperature Programmed Desorption (TPD) experiment following a procedure analogous to the one detailed by Bates et al. [140] for HSSZ-13. ∼40 mg of HSAPO-34 sample was treated in flowing 500 ppm NH_3 (achieved by flowing a mixture of 0.083 $cm^3\,s^{-1}$ 1.01% NH_3 in balance He (Certified Standard, Praxair) and 1.58 $cm^3\,s^{-1}$ He (99.997%, Minneapolis Oxygen)) at 323 K for 2 h (sufficient for the NH_3 signal, monitored via mass spectroscopy (MKS Cirrus), in the effluent stream to reach the same levels as observed in the bypass). The saturation treatment was followed by a He (1.67 $cm^3\,s^{-1}$) purge for 10 h to remove any physisorbed NH_3. TPD was performed under combined He (1.62 $cm^3\,s^{-1}$) and Ar (0.042 $cm^3\,s^{-1}$; 99.9995%, Matheson, used as an internal standard) flow by setting the ramp rate at 0.083 $K\,s^{-1}$ to reach a final temperature of 823 K, during which the effluent stream was monitored via mass spectrometry for signals corresponding to m/z = 16 (for NH_3)

and 40 (for Ar). The TPD profile obtained is shown in Fig. 4.14 plotted as the "desorption rate" versus temperature; the red (characterized by a low-temperature peak centered around ~423 K) and blue (characterized by a high-temperature peak centered around ~623 K) lines in the corresponding figure are peak deconvolution curve fits to the overall desorption curve fitted using Haarhoff-VanderLinde functions [141]. The area calculated under the blue curve was used to enumerate the Brønsted acid site density (Table 4.7) of the sample because as reported elsewhere [140, 142], the low-temperature feature is observed to disappear either by (i) washing the NH_3-saturated sample with deionized water at 323 K, or (ii) starting with the NH_4^+ form of the zeolite, prepared by treatment with NH_4NO_3, before exposure to NH_3. The disappearance of the low-temperature feature in case (i) and its complete absence in case (ii) is attributed to Lewis acid sites (supposedly giving rise to the low-temperature feature) being saturated with H_2O instead of NH_3 thereby indicating weak interactions with the latter [140, 142, 143].

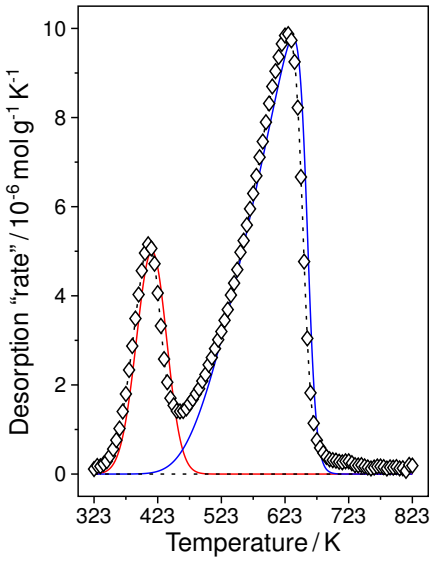

Fig. 4.14: NH_3 TPD curve of the HSAPO-34 sample observed during temperature ramp at 0.083 K s^{-1} following saturation with NH_3 at 323 K. The deconvoluted fitted curves characterized by a low-temperature peak (centered around ~423 K) and a high-temperature peak (centered around ~623 K) are shown as red- and blue-colored lines, respectively.

Table 4.7: Acid site density of the HSAPO-34 sample obtained from the area calculated under the NH_3 TPD curve presented in Fig. 4.14.

Acid site density	(mmol/g)	(per Si)
Total	1.43	0.93
Brønsted (blue curve)	1.11	0.72

Chapter 5

A mechanistic basis for effects of high pressure H_2 cofeeds on methanol to hydrocarbons catalysis over zeolites

*Reported from S. S. Arora, Z. Shi, A. Bhan, *ACS Catal.* **9** (2019) 6407-6414
(doi.org/10.1021/acscatal.9b00969)

5.1 Abstract

Co-feeding high-pressure (16 bar) H_2 with methanol (0.005 bar) during methanol to hydrocarbons conversion over acidic zeolites with varying topologies (CHA, AEI, FER, and BEA) results in a ∼2× to >15× enhancement in catalyst lifetime compared to He cofeeds, as determined by the cumulative turnovers attained per proton before the final methanol conversion level drops below 15 %C. These beneficial effects of prolonged catalyst lifetime are observed without any impact on the carbon backbone of effluent hydrocarbon products characteristic of the particular zeolite topology. The olefins-to-paraffins ratio of C_{2+} hydrocarbons, however, decreases due to enhanced paraffins production and the magnitude of this decrement depends on the specific zeolite topology. The observations of marked lifetime improvements and topology-dictated variations in the paraffin make of MTH effluent with H_2 cofeeds can be interpreted based on the different proclivities of zeolitic protons confined in varying topological environments for catalyzing hydrogenation of aliphatic hydrocarbons that are predominantly formed via formaldehyde-based alkylation routes (*e.g.*, 1,3-butadiene) or methanol-based alkylation routes (*e.g.*, ethene and propene). Independent kinetic studies reveal that measured hydrogenation rates (per H^+) of 1,3-butadiene are at least an order of magnitude (∼7× to ∼320×) higher than that of ethene or propene, which provides an explanation for the observed lifetime improvements in MTH with H_2 cofeeds. Further, trends in the reactivities of ethene and propene with H_2 over the different zeolites help explicate the topology-dependent variations in the paraffin content of the effluent hydrocarbons during MTH with H_2 cofeeds.

5.2 Introduction

The identity and distribution of hydrocarbon products in methanol-to-hydrocarbon (MTH) conversion primarily depend on the topological features of the zeolite used as the solid acid catalyst. The conversion of methanol over proton-form small-pore HSSZ-13 and HSSZ-39 zeolites characterized by large ellipsoidal cages interconnected via narrow 8-membered ring windows (3.8 Å × 3.8 Å) [98] results in the selective production of light hydrocarbons (C_2 – C_4) [16, 17, 144], while proton-form medium-pore HFER and large-pore HBEA zeolites primarily yield gasoline-range hydrocarbons—C_{4+} and aromatics [15, 26, 40]. The mechanistic origins of these hydrocarbon products are rationalized based on the hydrocarbon pool mechanism which can be described by a dual-cycle schematic that considers olefins and aromatics—interconvertible via chemistries of dehydrocyclization and dealkylation—as co-catalytic centers involved in distinct propagation events based on methylation and β-scission of olefins (referred as the 'olefins cycle'), and methylation and dealkylation of aromatics (referred as the 'aromatics cycle') [26, 31, 32, 37–39]. The aforementioned differences in the identity and distribution of hydrocarbon products depending on the zeolite topology are a consequence of the relative propagation of the olefins and aromatics cycles. The small-pore zeolites—HSSZ-13 and HSSZ-39—preferentially propagate the aromatics cycle in the large cages while only allowing the effusion of light hydrocarbons ($C_2 - C_4$); on the other hand, medium- and large-pore zeolites—HFER and HBEA—allow the simultaneous propagation of the olefins and aromatics cycles, and the effusion of both larger C_{4+} hydrocarbons and aromatics. The propagation events in MTH however, terminate with reaction progress due to the transformation of active olefin and aromatic species to inactive polycyclics, thereby causing catalyst deactivation [15, 26, 27, 90]. The formation of formaldehyde in transfer dehydrogenation events involving methanol, and its involvement in electrophilic addition reactions with olefins resulting in polyenes that can undergo dehydrocyclization to form aromatics and in electrophilic substitution reactions with aromatics to form intermediates that can further transform to polycyclic compounds has been documented in the recent literature [43, 60–63, 99, 106, 145].

In Chapter 4, we observed that co-feeding high-pressure H_2 results in the interception of formaldehyde-mediated alkylation pathways thereby resulting in longer catalyst lifetimes during MTH over HSAPO-34. Here, we demonstrate the utility of this strategy of co-feeding high-pressure H_2 for improving the MTH lifetime of various zeolites with distinct topologies (CHA, AEI, FER, and BEA). Besides the effect on lifetime, co-feeding H_2 also results in enhanced formation of paraffins, which manifests in lower olefins-to-paraffins ratios of the effluent hydrocarbons compared to the case of He cofeeds, albeit to varying extents depending on the specific zeolite topology. We provide a mechanistic basis for these observations in context of the reactivity of H_2 with 1,3-butadiene (formed via reaction between formaldehyde and propene [106, 145–147]) that intercepts its transformation to inactive polycyclics

compared to the reactivity of H_2 with ethene and propene (formed from methanol-based alkylation routes) that results in the formation of undesired paraffins in MTH over zeolites. This reactivity is quantified by hydrogenation rate constants measured during reactions of ethene, propene, and 1,3-butadiene with H_2 over the different zeolites in independent kinetic studies reported herein.

5.3 Materials and Methods

5.3.1 Catalyst characterization

The small-pore zeolites, SSZ-13 and SSZ-39, were obtained from ACS Material while the medium- and large-pore zeolites, FER and BEA, were sourced from Zeolyst (CP914C and CP814E, respectively) in their ammonium-form and converted to the proton-form by thermal treatment in flowing dry air (1.67 $cm^3\,s^{-1}$; Zero Grade, Matheson) at 823 K (0.0167 $K\,s^{-1}$ ramp rate from RT) for 4 h followed by pelletization, crushing, and sieving to retain 180-250 µm (60-80 mesh) aggregates. The bulk Si/Al ratios of these samples were ascertained from Scanning Electron Microscopy with Energy Dispersive X-ray Spectroscopy (SEM-EDS) measurements and are tabulated in Table 5.1. The Brønsted acid site densities of these samples are also listed in Table 5.1 and were obtained from NH_3 temperature programmed desorption (TPD) measurements performed by saturating ~50 mg of the proton-form samples with flowing 500 ppm NH_3 (1.01% in balance helium, Certified Standard, Praxair) balanced by He (99.9999%, Matheson) and Ar (99.9999%, Matheson) at 423 K followed by a purge in flowing He (1.67 $cm^3\,s^{-1}$) for 4 h at 423 K to desorb any physisorbed NH_3, and ramping the temperature at 0.167 $K\,s^{-1}$ ramp rate to 823 K in flowing He and Ar during which the effluent stream was monitored via mass spectrometry (MKS Cirrus) for signals corresponding to m/z = 16 (for NH_3) and 40 (for Ar, used as the internal standard) (Fig. 5.4a). Further, the Brønsted acid site count was also ascertained for the HFER and HBEA samples by pyridine infrared (IR) spectroscopy measurements (Table 5.4 and Fig. 5.4b) performed on self-supporting wafers following a procedure similar to the one reported by Harris et al. [148]. The integrated molar extinction coefficient (IMEC) for the IR band at 1542 cm^{-1} assigned to pyridine adsorbed on Brønsted acid sites was taken as 1.13 [149]. These measurements were not performed on the small-pore zeolite (HSSZ-13 and HSSZ-39) samples since pyridine is too bulky to enter the pores of these zeolites. The Brønsted acid site densities thus obtained are tabulated in Table 5.4 along with the corresponding values enumerated from NH_3-TPD, and are within a factor of ~0.8 – 1 of the NH_3-TPD count. To be consistent, all rate constants reported herein are obtained after normalization of the observed rates by the site count measured from NH_3-TPD. X-ray diffraction patterns were collected using a Bruker micro-diffractometer with Cu-K_α (λ = 1.54 Å) as the radiation source to confirm the framework type of the respective samples and are shown in Fig. 5.5. The t-plot micropore volume, Brunauer-Emmett-Teller (BET) and Langmuir surface areas

of the samples are also listed in Table 5.1 and were obtained from N_2 adsorption measurements collected at 77 K using ASAP 2020 (Micromeritics). The samples were degassed by evacuating the sample tube to ≤10 µmHg at 363 K (0.083 K s^{-1} ramp rate from RT) followed by thermal treatment in vacuo at 723 K (0.083 K s^{-1} ramp rate from 363 K) for 4 h prior to N_2 adsorption.

Table 5.1: Physical and chemical characteristics of zeolites used in the study.

Zeolite	Framework type	Source	Si/Al	H^+ density	Surface area		Micropore volume
					BET	Langmuir	
				(mmol g^{-1})	(m^2 g^{-1})		(cm^3 g^{-1})
HSSZ-13	CHA	ACS Material	13.2	0.44	560	825	0.28
HSSZ-39	AEI	ACS Material	9.0	0.83	506	761	0.27
HFER	FER	Zeolyst	10.0	0.64	283	419	0.13
HBEA	BEA	Zeolyst	12.4	0.33	530	798	0.16

5.3.2 Catalytic testing

All experiments were performed in a tubular glass-lined stainless steel reactor (6.35 mm O.D. and 4 mm I.D., Scientific Glass Engineering). The proton-form zeolite aggregates were physically mixed with aggregates of sand (Acros Organics, subjected prior to an overnight wash in 2 M HNO_3 solution followed by deionized water rinse until pH ∼7, and a final thermal treatment in flowing dry air (1.67 cm^3 s^{-1}) at 1273 K (0.083 K s^{-1} ramp rate from RT) for 16 h; $10 < wt_{diluent}/wt_{cat} < 15$) and packed in the middle of the reactor tube between quartz wool (Technical Glass Products) plugs. The tubular reactor was then placed inside a resistively heated furnace (Model 3210, Applied Test Systems); the reaction temperature was measured using a K-type thermocouple (TJ36-CAXL-020U-12, Omega) wrapped around the reactor periphery with the tip placed at the center of the catalyst bed and regulated with an electronic controller (Series 96, Watlow). The free volume above and below the catalyst bed was filled by quartz rods (3 mm O.D.; Technical Glass Products) to prevent any vertical displacement of the catalyst bed. Prior to catalytic measurements, the catalyst bed was pretreated in flowing dry air (1.67 cm^3 s^{-1}) at 823 K (0.0167 K s^{-1} ramp rate from RT) for 4 h prior to cooling down to the desired reaction temperature in helium flow (1.67 cm^3 s^{-1}). The gas-phase pressure of the influent and effluent streams was measured using pressure transducers (0 – 6890 kPag; PX32B1-1KGV, Omega) placed upstream and downstream of the reactor tube. The composition of the reactant and product streams were quantified using a gas chromatograph (Model 7890A, Agilent) equipped with a dimethylpolysiloxane HP-1 column (50 m × 320 µm × 0.52 µm) connected to a flame ionization detector and a mass spectrometer (Model 5975C, Agilent) for detection of hydrocarbons and oxygenates, and a GS-GasPro column (60 m × 320 µm) or Porapak Q (4.6 m × 3.2 mm × 2 mm) connected to a thermal conductivity detector for detecting permanent gases (H_2, Ar, and N_2).

Methanol conversion with H_2 or He cofeeds

Methanol (CHROMASOLV®; Honeywell) was fed using a 100 mL stainless-steel syringe (Harvard Apparatus) and PHD ULTRA® XF syringe pump (Harvard Apparatus) to heated lines and carried by the gas stream. The diluent [H_2 (99.9999%, Matheson)] and internal standard [N_2 (99.999%, Matheson)] flows were metered using mass flow controllers (Model 5850E, Brooks). H_2 was substituted with He (99.9999%, Matheson) as the diluent in the control experiments. Product selectivities and methanol conversion (calculated based on the total amount of methanol/dimethyl ether (DME)-derived carbon atoms observed in the effluent hydrocarbons) profiles were measured during reactions of methanol (0.005 bar) with high-pressure (16 bar) H_2 or He cofeeds over packed beds comprised of HSSZ-13, HSSZ-39, HFER, and HBEA at 623 K and space velocities that resulted in sub-complete methanol conversion.

Ethene, propene, and 1,3-butadiene hydrogenation with H_2

Ethene (0.1% in balance He, Primary Standard, Matheson), propene (0.1% in balance Ar, Certified Standard, Gasco), 1,3-butadiene (0.05% in balance He, Certified Standard, Praxair), H_2 (99.9999%, Matheson), and Ar (99.9995%, Matheson; used as the internal standard) flows were metered using mass flow controllers (Model 5850E, Brooks). The steady state hydrogenation rates were measured by adjusting the reactant flow rates to obtain the desired partial pressures of the respective reagents (0.0001 – 0.001 bar for the hydrocarbons, and 1 – 16 bar for H_2) and space velocities that resulted in differential conditions ($< 5\%$ conversion). The apparent enthalpic and entropic barriers were estimated from hydrogenation rate constants measured between 623 K and 748 K.

5.4 Results and Discussion

5.4.1 Effects of H_2 cofeeds on MTH catalysis

As shown in Fig. 5.1a, MTH lifetime, as assessed by cumulative turnovers—defined as the total amount of methanol/DME-derived carbon atoms observed in the effluent hydrocarbons normalized by the total acid sites in the catalyst bed [36]—attained until the final methanol conversion drops below 15 %C, of HSSZ-13, HSSZ-39, HFER, and HBEA is considerably enhanced ($\sim$2× to >15×) with high-pressure (16 bar) H_2 cofeeds relative to the case of He cofeeds at equivalent concentrations under sub-complete methanol conversion conditions. These observations are in line with the results reported in Chapter 4 and in a recent report by Zhao et al. [150] during methanol conversion over HSAPO-34, and demonstrate the general utility of the proposed strategy of co-feeding high-pressure H_2 to markedly mitigate catalyst deactivation and prolong catalyst lifetimes during MTH over zeolites. Furthermore, as depicted in Fig. 5.1b, these improvements in catalyst lifetime are observed without any

impact on the carbon backbone of the effluent hydrocarbons characteristic of the particular zeolite topology. The maximum methanol conversion levels decrease with H_2 cofeeds relative to the case of He cofeeds over all zeolites. This is likely related to the increase in the production of paraffins with H_2 cofeeds since paraffins can be considered as terminal products under MTH conditions [96].

The increase in paraffins production with H_2 cofeeds causes a decrement in the overall olefins-to-paraffins ratio—defined as the ratio of cumulative turnovers attained towards C_{2+} olefins and cumulative turnovers attained towards C_{2+} paraffins in the effluent over the catalyst lifetime—relative to the case of co-feeding He (Fig. 5.1b). This decrement primarily arises from the enhanced production of C_2-C_4 paraffins over all zeolites, except in the case of HSSZ-39 where it is specifically a result of the higher formation of propane. Further, the magnitude of the decrement depends on the specific zeolite topology (∼2.8× over HSSZ-13, ∼4.6× over HSSZ-39, ∼9.8× over HFER, and ∼1.6× over HBEA).

We postulate that the observed effects of lifetime improvement and topology-dependent differences in the paraffin make of the MTH effluent with H_2 cofeeds can be mechanistically related to the relative reactivity of ethene, propene, and 1,3-butadiene with H_2 among the different zeolites. We evidence this by obtaining the rate constants for hydrogenation of the aforementioned species in independent kinetic studies, as detailed in the next section.

5.4.2 Kinetic studies of ethene, propene, and 1,3-butadiene hydrogenation with H_2

Reactions of ethene, propene, and 1,3-butadiene (0.0001 – 0.001 bar) with high-pressure H_2 (1 – 16 bar) while maintaining high H_2-to-hydrocarbon ratios (>3000 in the case of ethene and propene and >12000 in the case of 1,3-butadiene) at temperatures relevant for MTH catalysis (623 – 748 K) and differential conversions (<5 %C) resulted in high selectivity of the first hydrogenated analogs—ethane (>99 %C), propane (>80 %C; balance CH_4 and C_2H_4 likely resulting from cracking of C_3H_8 or C_3H_6 oligomers), and a mix of butene isomers (>80 %C; balance C_2H_4 and C_3H_6 likely resulting from cracking of C_4H_8 or C_4H_8 oligomers)—of the respective hydrocarbon reactant. The measured hydrogenation rates (per H^+) were stable with time on stream and depended weakly on the space velocity of the hydrocarbon reactant (Fig. 5.6) indicating that the rate measurements were not affected by deactivation and secondary reactions or inhibition by products. Further, using the Weisz-Prater criterion [151], and measuring hydrogenation rates (per H^+) on a HFER sample with a different Si/Al ratio (= 27.5) than the one presented here (Si/Al = 10), it was verified that the measured rates were not corrupted by internal diffusion limitations and reflect solely the propensity of zeolitic protons confined in varying topological environments to catalyze the hydrogenation reactions under study (Table 5.5 and Fig. 5.8).

Fig. 5.2 shows that the measured formation rates of ethane, propane, and butene

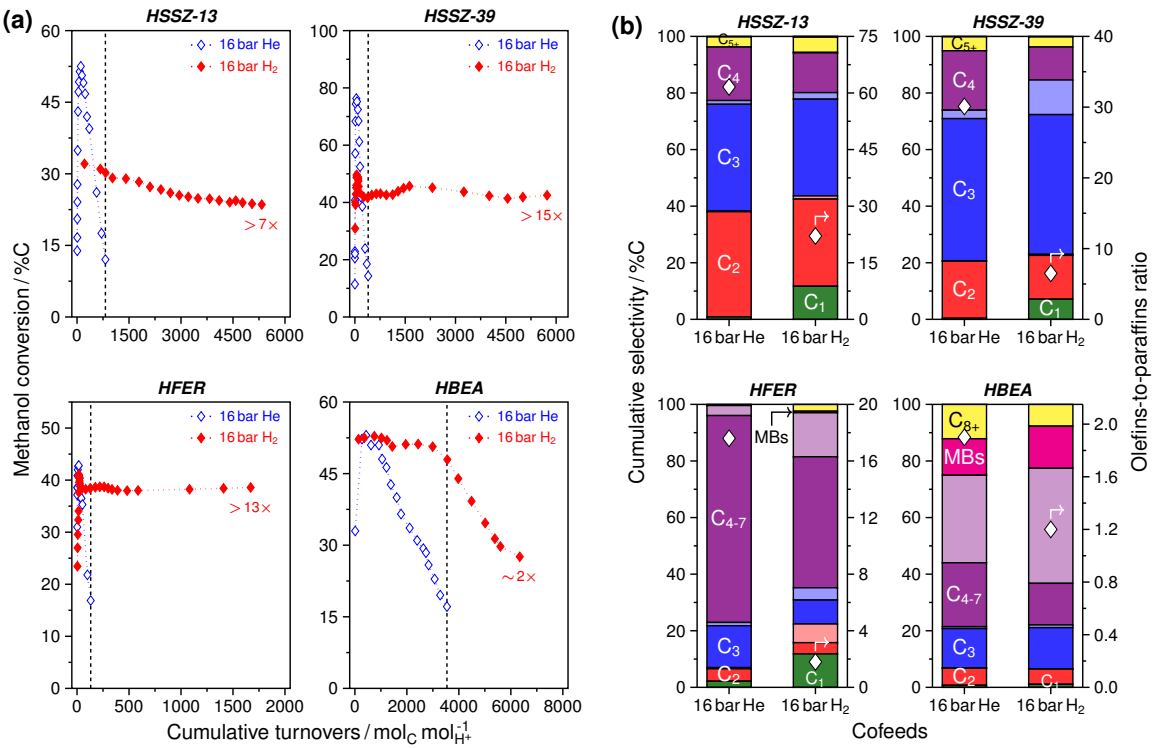

Fig. 5.1: (a) Methanol conversion profiles versus cumulative turnovers; (b) Cumulative selectivity (*left* ordinate) and the overall olefins-to-paraffins ratio (*right* ordinate, ◊) in the effluent stream observed during methanol feeds without (empty symbols) and with (filled symbols) H_2 cofeeds over HSSZ-13, HSSZ-39, HFER, and HBEA at 623 K, 0.005 bar CH_3OH, 16 bar He or H_2 co-feed, 350 (HSSZ-13); 114 (HSSZ-39); 61 (HFER); 89 (HBEA) $mol_C\ (mol_{H^+} \cdot ks)^{-1}$. (a) The vertical dashed lines denote the cumulative turnover capacity of the particular zeolite for methanol conversion with 16 bar He co-feed, which is used to calculate the relative lifetime improvement factors (listed at the end of the lines with filled symbols) with 16 bar H_2 cofeeds. (b) The dark- and light-shaded bars represent the olefinic and paraffinic forms, respectively, of the respective carbon group listed in the dark bars; 'MBs' represents methyl-substituted benzenes.

isomers (r_{RH_2}) normalized by the total Brønsted acid sites ($[H^+]$) in the catalyst bed are linearly dependent on the partial pressures of both the aliphatic hydrocarbon [R = ethene (e), propene (p), 1,3-butadiene (b)] (p_R) and H_2 (p_{H_2}), and can be described by the rate expression shown in Eq. 5.1.

$$\frac{r_{RH_2}}{[H^+]} = k^R_{H_2} p_R p_{H_2} \tag{5.1}$$

The effective second-order rate constants ($k^R_{H_2}$), calculated as the slope of the linear fit to the observed rate measurements, of hydrogenation of ethene, propene, and 1,3-butadiene over the four zeolites considered in this study are tabulated in Table 5.2.

The observed rate expression for hydrogenation of aliphatic hydrocarbons over acidic zeolites (Eq. 5.1) can be realized by the set of elementary steps shown in Scheme 5.1 under

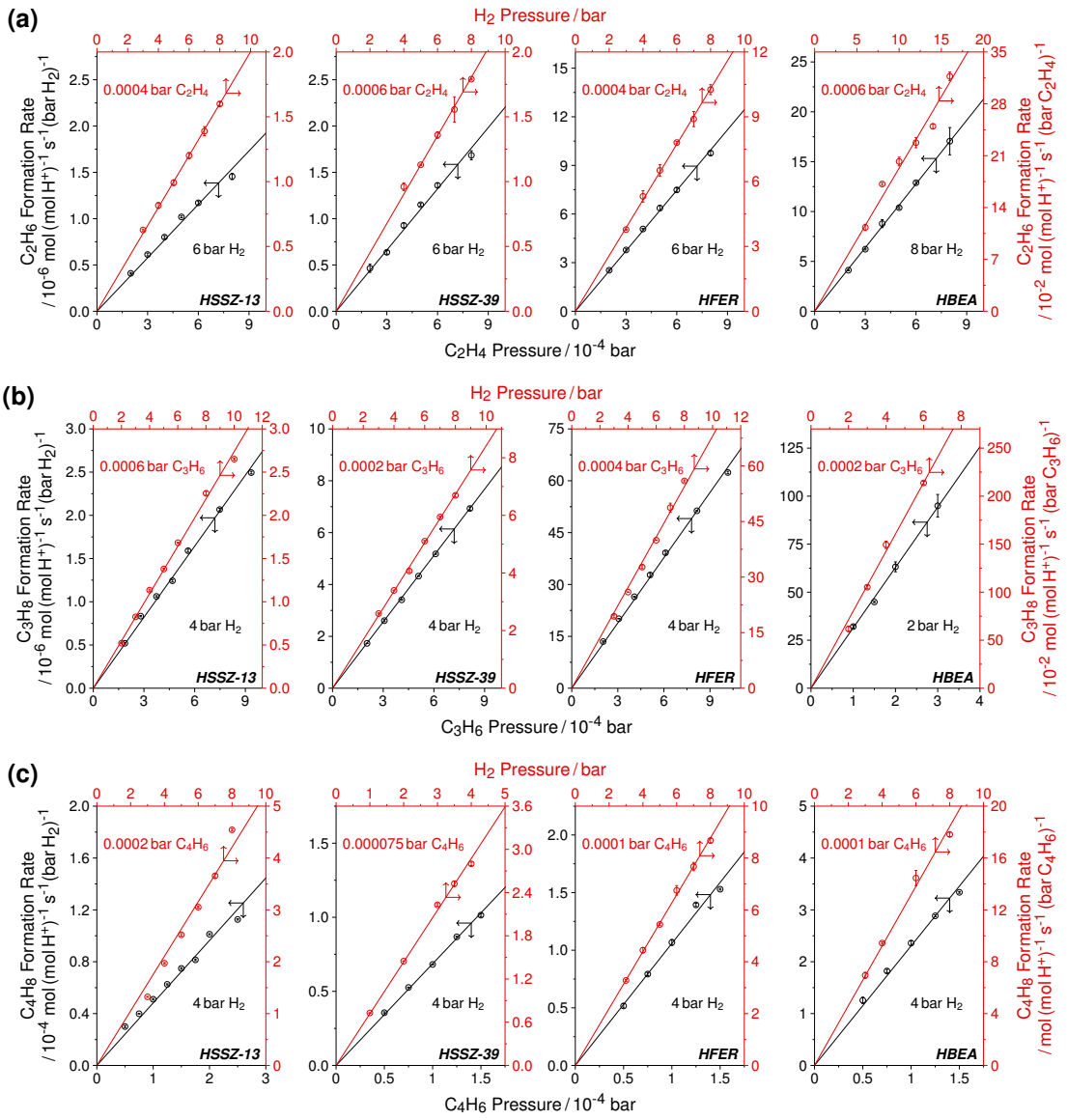

Fig. 5.2: Dependence of the formation rates (per H^+) of ethane, propane, and butenes on partial pressures of the hydrocarbon (*bottom-left* axes) and H_2 (*top-right* axes) during reactions of (a) ethene, (b) propene, and (c) 1,3-butadiene with H_2 over HSSZ-13 , HSSZ-39, HFER, and HBEA at 673 K. The quantities listed along each line indicate the partial pressure of either the hydrocarbon or H_2 held constant while varying the partial pressure of the other reagent during the kinetic measurements. The vertical bars on each data point represent the standard-error associated with each measurement. The solid lines represent a linear fit to the experimental data.

the following assumptions: i) the fourth step involving the reaction between the surface intermediate derived from the hydrocarbon reactant (RH^+) and intrazeolite H_2 species ($H_2\,(z)$) is rate-limiting, ii) all other steps involving the adsorption/desorption of the reactants and products into and out of the zeolite channels are quasi-equilibrated, and iii)

Table 5.2: Effective second-order rate constants [mol (mol H^+)$^{-1}$ s^{-1} (bar R)$^{-1}$ (bar H_2)$^{-1}$] of hydrogenation of aliphatic hydrocarbons [R = ethene (C_2H_4), propene (C_3H_6), and 1,3-butadiene (C_4H_6)] with H_2 over acidic zeolites at 673 K and their 95% confidence intervals.

Zeolite	$k_{H_2}^{C_2H_4}$	$k_{H_2}^{C_3H_6}$	$k_{H_2}^{C_4H_6}$
HSSZ-13	0.0019 ± 0.00017	0.0027 ± 0.00017	0.50 ± 0.09
HSSZ-39	0.0022 ± 0.00027	0.0084 ± 0.00030	0.70 ± 0.05
HFER	0.013 ± 0.00062	0.066 ± 0.0052	1.1 ± 0.11
HBEA	0.020 ± 0.0024	0.33 ± 0.058	2.3 ± 0.41

Brønsted acid sites (H^+) are the dominant surface species. The observed kinetic behavior is consistent with and the proposed set of elementary steps follow those reported by Gounder and Iglesia [120] for hydrogenation of propene on acidic zeolites.

$R\,(g)$	$\overset{k_1}{\underset{k_{-1}}{\rightleftharpoons}}$	$R\,(z)$	K_1
$H_2\,(g)$	$\overset{k_2}{\underset{k_{-2}}{\rightleftharpoons}}$	$H_2\,(z)$	K_2
$R\,(z) + H^+$	$\overset{k_3}{\underset{k_{-3}}{\rightleftharpoons}}$	RH^+	K_3
$\mathbf{RH^+ + H_2\,(z)}$	$\xrightarrow{\boldsymbol{k_4}}$	$\mathbf{RH_2\,(z) + H^+}$	$\boldsymbol{k_4}$
$RH_2\,(z)$	$\overset{k_5}{\underset{k_{-5}}{\rightleftharpoons}}$	$RH_2\,(g)$	K_5
$R\,(g) + H_2\,(g)$	$\xrightarrow{k_{H_2}^R}$	$RH_2\,(g)$	

$$r_{RH_2} = k_4\,[RH^+]\,[H_2(z)]$$

$$\frac{r_{RH_2}}{[H^+]} = \underbrace{k_4 K_3 K_2 K_1}_{k_{H_2}^R} p_R p_{H_2}$$

Scheme 5.1: Elementary steps proposed for hydrogenation of aliphatic hydrocarbons [R = ethene (e), propene (p), and 1,3-butadiene (b)] with H_2 over Brønsted acid (H^+) zeolites. The step highlighted in bold is considered as rate-limiting. The notations g and z in the parenthesis denote the gas phase and intrazeolite phase, respectively.

The temperature dependence of the measured hydrogenation rate constants at fixed partial pressures of R and H_2 is presented in Fig. 5.3 and can be described by the Arrhenius equation,

$$\ln(k_{H_2}^R) = \ln A - \frac{E_a}{RT}\,, \tag{5.2}$$

where A and E_a reflect the pre-exponential factors and the apparent enthalpic barriers, respectively, for the hydrogenation reactions. The pre-exponential factors in Eq. 5.2 can

be used to calculate the apparent entropic barriers (ΔS_a) after accounting for the number of C–H bonds (n_b) in the first hydrogenated analogs of the hydrocarbon reactants (6, 8, and 8 for ethene, propene, and 1,3-butadiene, respectively) using Eq. 5.3, which follows the formalism reported by Gounder and Iglesia [120, 152]. Under the observed kinetic regime characterized by a linear dependence on both hydrocarbon and H_2 pressures, the measured apparent enthalpic (or entropic) barriers reflect the enthalpy (or entropy) difference between the hydrogenation transition state (TS) in the intrazeolite phase, and the gas-phase reactants (R and H_2) and the bare H^+ (Eqs. 5.4 and 5.6). Separately, considering the expression of the hydrogenation rate constant ($k^R_{H_2} = k_4K_3K_2K_1$) deduced from the elementary steps proposed in Scheme 5.1, the apparent enthalpic (or entropic) barriers can also be interpreted as a combination of two components – (i) enthalpic gains (or entropic losses) resulting from adsorption of gas-phase reactants (R and H_2) into the confining voids of a zeolite, represented by ΔH_{ads} (or ΔS_{ads}) which arises from a combination of K_1, K_2, and K_3; and (ii) enthalpic losses (or entropic gains) originating from reaction of the adsorbed intermediates to form the relevant transition state that transforms to the gas-phase product, represented by ΔH_{int} (or ΔS_{int}) which arises from k_4 (Eqs. 5.5 and 5.7). Accordingly, positive or negative values of the apparent enthalpic (or entropic) barriers reflect compensation between these enthalpic (or entropic) gains or losses during a certain reaction over a particular zeolite [153–155]. Specifically, a positive value of the apparent enthalpic barrier reflects a scenario when $\Delta H_{int} > \Delta H_{ads}$, and a negative value can be realized when $\Delta H_{int} < \Delta H_{ads}$. The experimentally measured values of these barriers for hydrogenation reactions of ethene, propene, and 1,3-butadiene over all zeolite samples used in the study are listed in Table 5.3. We note that the distinct topological features of the acidic zeolites can affect the measured enthalpic (or entropic) barriers by influencing ΔH_{ads} (or ΔS_{ads}) and ΔH_{int} (or ΔS_{int}), therefore, any interpretation of the observed differences based on their topology would require evaluation of both these components under reaction conditions.

$$\Delta S_a = R\left[\ln\left(\frac{A}{n_b}\right) - \ln\left(\frac{k_B T}{h}\right)\right]. \tag{5.3}$$

$$E_a = E_{TS} - E_{R(g)} - E_{H_2(g)} - E_{H^+} \tag{5.4}$$

$$= \Delta H_{int} - \Delta H_{ads} \tag{5.5}$$

$$\Delta S_a = \Delta S_{TS} - \Delta S_{R(g)} - \Delta S_{H_2(g)} - \Delta S_{H^+} \tag{5.6}$$

$$= \Delta S_{int} - \Delta S_{ads} \tag{5.7}$$

As shown in Table 5.2, the measured hydrogenation rate constants of 1,3-butadiene are

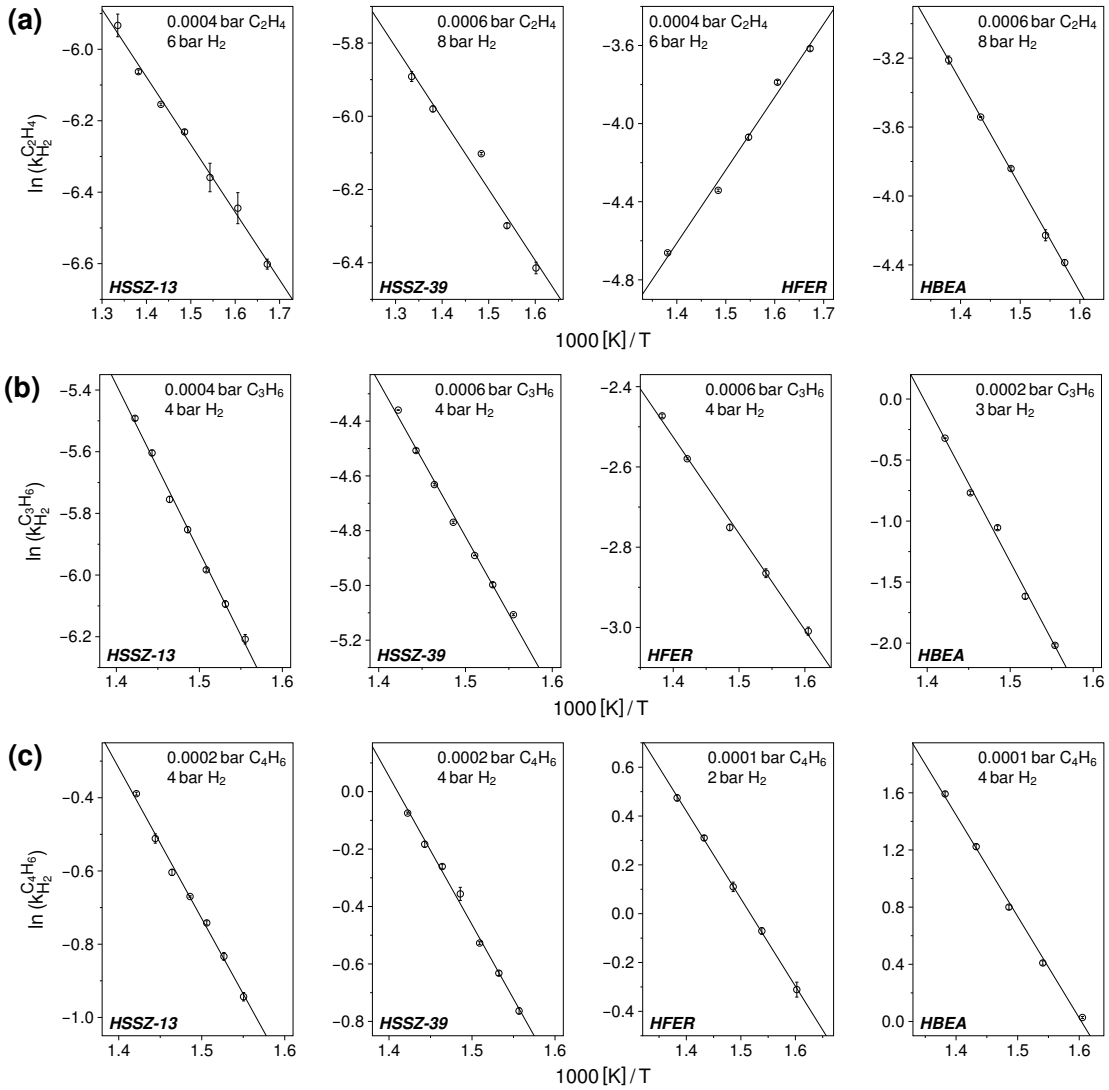

Fig. 5.3: Temperature dependence of the effective second-order hydrogenation rate constants of (a) ethene, (b) propene, and (c) 1,3-butadiene hydrogenation with H_2 over HSSZ-13, HSSZ-39, HFER, and HBEA at 623 – 748 K. The pressures listed in each panel represent the partial pressures of the hydrocarbon reactant and H_2 that were held constant while varying the temperature. The vertical bars on each data point represent the standard-error associated with each measurement. The solid lines represent a linear fit to the experimental data.

at least an order-of-magnitude (∼7× to ∼320×) higher than the corresponding values for ethene and propene over all zeolites used in the study. This difference is indicative of the high reactivity of 1,3-butadiene with H_2 which consequently results in interception of its further transformation to aromatics and polycyclics, and provides a mechanistic basis for the observed enhancements in catalyst lifetime during MTH with H_2 cofeeds. We propound that the weak hydrogenation ability of Brønsted acid sites in zeolites relative to metal-based hydrogenation catalyst formulations, and the higher degree of unsaturation in 1,3-butadiene

Table 5.3: Apparent enthalpic (E_a; [kJ mol^{-1}]) and entropic (ΔS_a; [J mol^{-1} K^{-1}]) barriers for hydrogenation of ethene, propene, and 1,3-butadiene over acid zeolites and their 95% confidence intervals.

Zeolite	Ethene		Propene		1,3-Butadiene	
	E_a (kJ mol^{-1})	ΔS_a (J mol^{-1} K^{-1})	E_a (kJ mol^{-1})	ΔS_a (J mol^{-1} K^{-1})	E_a (kJ mol^{-1})	ΔS_a (J mol^{-1} K^{-1})
HSSZ-13	16 ± 1	-295 ± 2	45 ± 2	-251 ± 4	34 ± 2	-224 ± 3
HSSZ-39	16 ± 4	-294 ± 6	46 ± 3	-239 ± 5	43 ± 3	-208 ± 4
HFER	-31 ± 4	-348 ± 6	20 ± 2	-262 ± 2	30 ± 1	-224 ± 1
HBEA	51 ± 2	-223 ± 3	106 ± 12	-120 ± 18	59 ± 4	-174 ± 7

than in ethene and propene likely results in the observed higher reactivity of 1,3-butadiene with H_2 compared to ethene and propene.

Further, we discuss the topology-dependent decrements in the olefins-to-paraffins ratios of effluent with H_2 cofeeds in context of the measured hydrogenation rate constants of ethene and propene that are observed to be dictated by the zeolite topology (Table 5.2). The low ($\sim$2.8$\times$) decrement in the olefins-to-paraffins ratio or correspondingly, the predominance of C_2-C_4 olefins over their paraffinic counterparts during MTH with H_2 cofeeds over HSSZ-13 compared to other zeolites can be explained by the lowest values of the hydrogenation rate constants of ethene (0.0019 versus $0.013-0.020$ mol (mol H$^+$)$^{-1}$ s^{-1} (bar C_2H_4)$^{-1}$ (bar H_2)$^{-1}$) and propene (0.0027 versus $0.0084-0.33$ mol (mol H$^+$)$^{-1}$ s^{-1} (bar C_3H_6)$^{-1}$ (bar H_2)$^{-1}$) over HSSZ-13 among the zeolites used in the study. In the case of HSSZ-39 compared to HSSZ-13, the higher selectivity of propane in the MTH effluent with H_2 cofeeds can be explicated by the higher value (0.0084 versus 0.0027 mol (mol H$^+$)$^{-1}$ s^{-1} (bar C_3H_6)$^{-1}$ (bar H_2)$^{-1}$) of the measured rate constant of propene hydrogenation relative to HSSZ-13, while the insignificant increase in ethane formation can be considered a result of its low activity [0.0022 mol (mol H$^+$)$^{-1}$ s^{-1} (bar C_2H_4)$^{-1}$ (bar H_2)$^{-1}$] for ethene hydrogenation which is similar to HSSZ-13. The measured hydrogenation rate constants of ethene, 0.013 mol (mol H$^+$)$^{-1}$ s^{-1} (bar C_2H_4)$^{-1}$ (bar H_2)$^{-1}$, and propene, 0.066 mol (mol H$^+$)$^{-1}$ s^{-1} (bar C_3H_6)$^{-1}$ (bar H_2)$^{-1}$, are both observed to be significantly higher on HFER relative to both HSSZ-13 and HSSZ-39, and expound the highest decrement ($\sim$9.8$\times$) in the olefins-to-paraffins ratio during MTH with H_2 cofeeds. HBEA, however, deviates from the trend and although the hydrogenation rate constants of ethene, propene, and 1,3-butadiene are highest amongst the zeolites considered, the effects on lifetime ($\sim$2$\times$ increment) and olefins-to-paraffins ratio ($\sim$1.6$\times$ decrement) with H_2 cofeeds are less significant compared to other zeolites (Fig. 5.1). This is likely a consequence of the relatively high lifetime ($\sim$3500 versus $\sim 130-800$ mol$_C$ mol$_{H^+}^{-1}$) and low olefins-to-paraffins ratio ($\sim$1.9 versus $\sim 17.6-61.6$) observed in the baseline MTH case with He cofeeds over HBEA compared to other zeolites.

5.5 Conclusions

The effectiveness of high-pressure H_2 cofeeds to enhance catalyst lifetime during MTH catalysis is demonstrated for four different zeolites (HSSZ-13, HSSZ-39, HFER, and HBEA) with varying topologies (CHA, AEI, FER, and BEA) validating the general utility of the proposed strategy. This effect of lifetime improvement with H_2 cofeeds can be mechanistically related to the higher proclivity of 1,3-butadiene to undergo hydrogenation with H_2, relative to ethene and propene, which intercepts its further transformation and likely leads to suppressed production of deactivation-inducing polycyclics during methanol conversion. The topology-dependent variations in the paraffin make of the effluent hydrocarbons during MTH with H_2 cofeeds over different zeolites can be interpreted based on the varying catalytic behavior of protons towards hydrogenation of ethene and propene, wherein a higher predisposition for these reactions is observed to correspond to lower olefins-to-paraffins ratios or higher paraffins production during MTH with H_2 cofeeds.

Acknowledgements

Ms. Zhichen Shi from the University of Minnesota collected the NH_3 TPD measurements of all zeolite samples, transient during propane uptake in HSSZ-13, and also performed all the catalytic experiments involving methanol conversion with and without H_2 cofeeds over the different zeolites considered in the study. We thank (i) Dow through the University Partnership Initiative and the National Science Foundation (CBET 1701534) for financial support, (ii) Dr. Andrzej Malek, Dr. Davy L. S. Nieskens, and Dr. Joseph DeWilde from Dow for helpful technical discussions, (iii) Dr. Nicholas Seaton from the University of Minnesota Characterization Facility for providing the EDS data of all zeolite samples, (iv) Mr. Xinyu Li from the University of Minnesota for providing the XRD patterns of all zeolite samples and pyridine IR spectra of the HBEA sample.

5.6 Supplementary Information

5.6.1 Brønsted acid site density measurements

Fig. 5.4a shows the ammonia temperature programmed desorption (TPD) curve of the HSSZ-13 sample and Fig. 5.4b shows the infrared (IR) spectra recorded after pyridine adsorption on the HBEA sample. The site densities enumerated from these measurements on the samples are tabulated in Table 5.4.

5.6.2 X-ray Diffraction

The powder X-ray diffraction patterns of the different zeolite samples – SSZ-13, SSZ-39, FER, and BEA – used in the study were recorded on a Bruker D5005 diffractometer using Cu-K_α ($\lambda = 1.54\,\text{Å}$) as the radiation source. The observed diffraction patterns (Fig. 5.5)

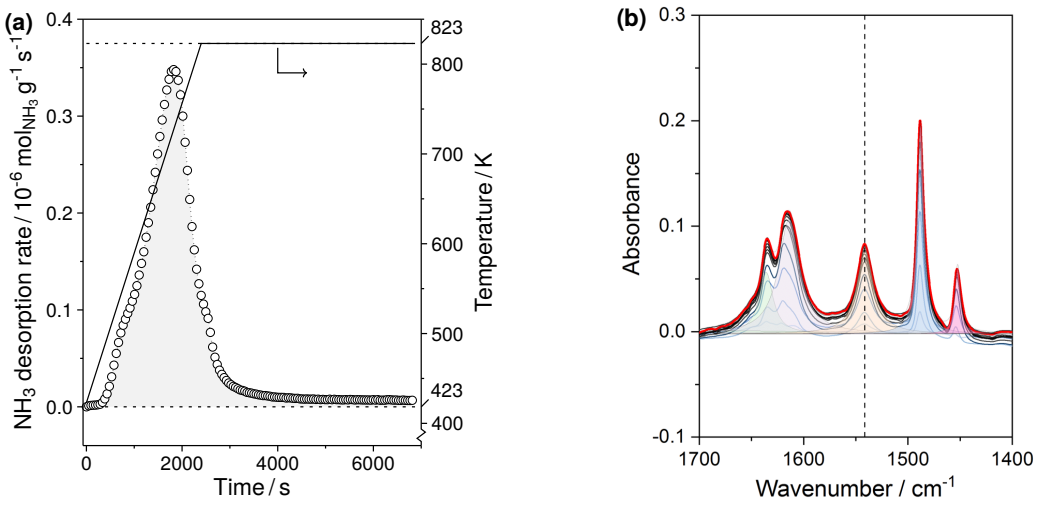

Fig. 5.4: (a) NH_3 desorption rate (*left* ordinate) versus time curve observed during temperature (*right* ordinate) ramp at $0.167\,K\,s^{-1}$ following saturation at 423 K in NH_3 TPD measurement of the HSSZ-13 sample. (b) IR spectra recorded under dynamic vacuum (∼20 µmHg) after pyridine adsorption (using sequential doses) on the HBEA sample at 323 K; the red curve represents the IR spectra obtained at saturation coverage of pyridine and the dashed line at $1542\,cm^{-1}$ represents the IR band associated with pyridine adsorbed on Brønsted acid sites.

Table 5.4: Brønsted acid site density of different zeolite samples enumerated using NH_3-TPD and pyridine IR measurements.

Sample	**Brønsted acid site density (mmol g^{-1})**	
	NH_3-TPD	Pyridine IR
HSSZ-13	0.44	n.m.*
HSSZ-39	0.83	n.m.
HFER	0.64	0.62
HBEA	0.33	0.26

*n.m. = not measured

confirm the framework types as CHA, AEI, FER, and BEA, respectively of the different zeolites, and indicate that no major impurity phases are present in the materials.

5.6.3 Check for stability and space-velocity effects on the rate measurements

As shown in Fig. 5.6a-b, the measured propane formation rates (per H^+) during reactions of propene (0.0004 bar) with H_2 (4 bar) over HSSZ-13 are observed to be stable with time on stream and weakly dependent on the space velocity (SV) of propene evidencing that the measured hydrogenation rates are unaffected by deactivation and secondary reactions or inhibition by products.

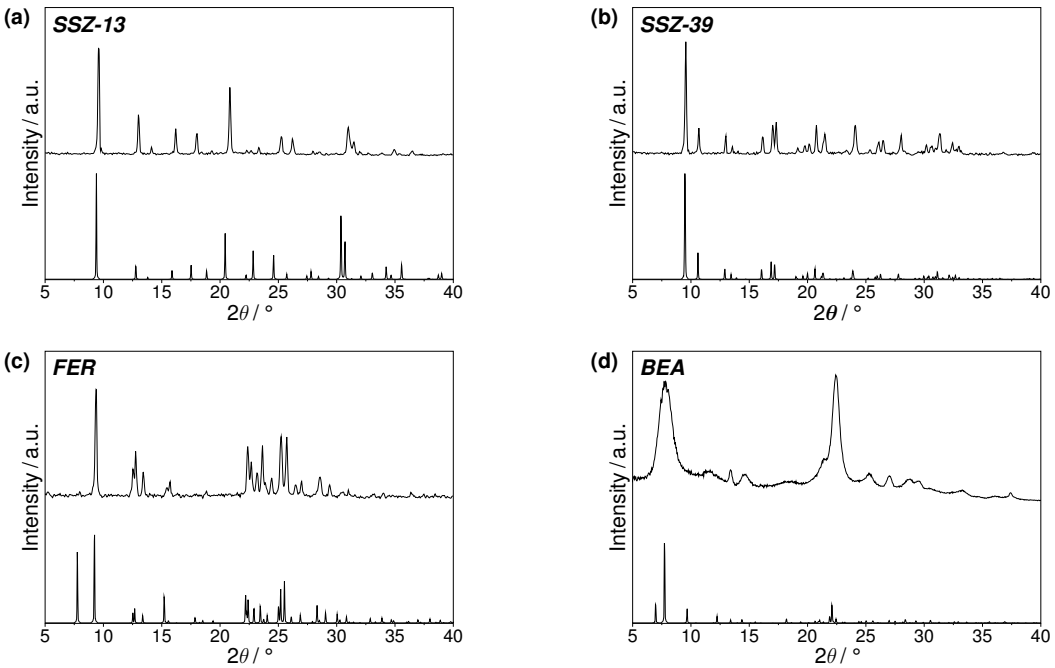

Fig. 5.5: XRD patterns of (a) SSZ-13, (b) SSZ-39, (c) FER, and (d) BEA samples used in the study (*top*) along with the reference spectra of the respective framework type obtained from IZA [98] (*bottom*).

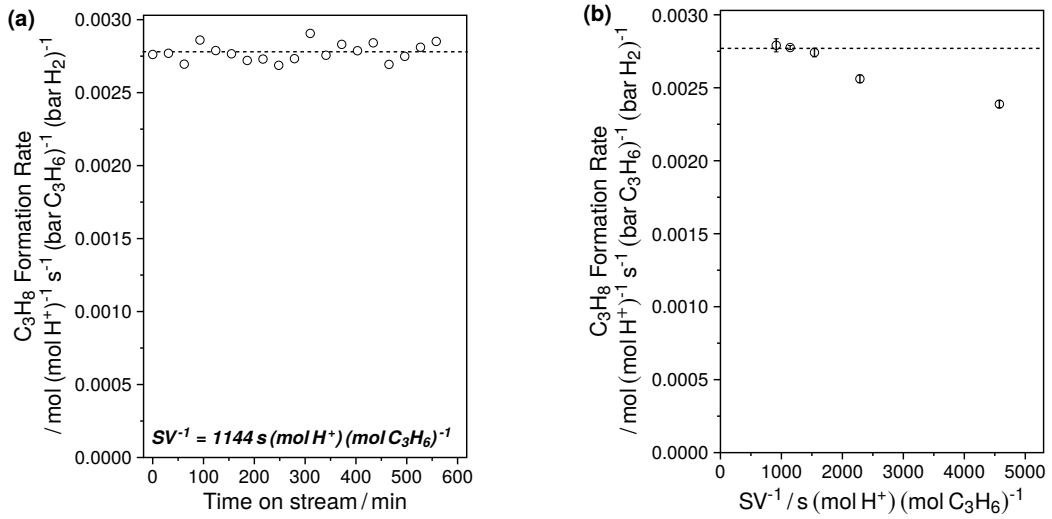

Fig. 5.6: Dependence of propane formation rates (per H^+) on (a) time on stream and (b) space velocity (SV) during reactions of propene (0.0004 bar) with H_2 (4 bar) over HSSZ-13. The vertical bars on each data point in (b) represent the standard-error associated with each measurement and the dashed horizontal lines in (a) and (b) represent the value of formation rate of propane that is constant irrespective of the time on stream or changes in the space-velocity.

5.6.4 Check for effects of intracrystalline diffusional limitations

The absence of intracrystalline diffusional limitations on the rate measurements, especially in the case of small-pore zeolites, HSSZ-13 and HSSZ-39, was confirmed by using the Weisz-Prater criterion [151]. The values tabulated in Table 5.5 show that the effectiveness factor (η) is = 1, which implies that the measured hydrogenation rates are not corrupted by internal mass transfer limitations. (Note: The value of D/R^2 was estimated by fitting the experimentally observed propane uptake data (Fig. 5.7) collected at 333 K to equation 5.8 [156]. The value of D/R^2 thus obtained provides a lower-bound on the diffusion rate since at reaction temperature of 673 K, the corresponding value will be higher. $(k_{H_2} p_{H_2})_{673\,K}$ represents the pseudo-first order hydrogenation rate constant measured at 673 K. Therefore, the Thiele modulus (ϕ) and the corresponding effectiveness factor (η) are calculated while considering the lower-bound on the diffusion rate and an upper-bound on the measured reaction rate.)

$$\frac{N_t}{N_\infty} = 1 - \frac{6}{\pi^2} \sum_{n=1}^{\infty} \frac{1}{n^2} \exp\left(\frac{-D\pi^2 n^2 t}{R^2}\right), \tag{5.8}$$

where N_t is the molar uptake at time t and N_∞ that at equilibrium, R^2/D represents the diffusional time scale.

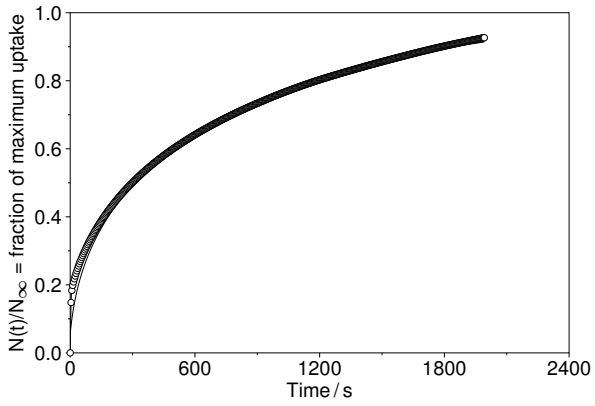

Fig. 5.7: Transient during propane uptake in HSSZ-13 at 333 K ($P^o_{C_3H_8}$ = 0.3 kPa). The solid line represents the fit to equation 5.8.

In addition to the above mathematical consideration of the effect of diffusional constraints, we also measured ethene hydrogenation rates (per H^+) on a different HFER sample (Zeolyst CP914; Si/Al = 27.5) with lower $[H^+]$ (= 0.39 mmol g^{-1} as assessed by NH_3 TPD) than the one (Zeolyst CP914C; Si/Al = 10; $[H^+]$ = 0.64 mmol g^{-1}) reported earlier to experimentally assess the effect of intracrystalline diffusional constraints on the rate measurements, since under conditions with severe mass transfer limitations, samples with high $[H^+]$ can create intracrystalline gradients due to rapid reactant depletion rates. As depicted in Fig. 5.8, ethane formation rates (per H^+) vary linearly with the

Table 5.5: Weisz-Prater criterion calculations for assessing effects of internal mass transfer limitations during propene hydrogenation rate measurements on HSSZ-13.

$[\mathbf{H^+}](\mathbf{R^2}/\mathbf{D_{C_3H_8\,@\,333\,K}})$	0.14	$(\mathrm{mol\,H^+})\,\mathrm{s}$
$(\mathbf{k_{H_2}p_{H_2}})_{\mathbf{673\,K}}$	2.7×10^{-7}	$(\mathrm{mol\,H^+})^{-1}\,\mathrm{s}^{-1}$
$\phi\left[=\sqrt{(\mathbf{k_{H_2}P_{H_2}})_{\mathbf{673\,K}} \times [\mathbf{H^+}]\mathbf{R^2}/\mathbf{D}}\right]$	1.9×10^{-4}	
$\eta\left[=\dfrac{\tanh\phi}{\phi}\right]$	1	

partial pressures of both ethene and H_2, and the effective second-order rate constant is $\sim$0.0097 mol $(\mathrm{mol\,H^+})^{-1}\,\mathrm{s}^{-1}$ $(\mathrm{bar\,C_2H_4})^{-1}$ $(\mathrm{bar\,H_2})^{-1}$ which is within a factor of $\sim$0.7 to the value of 0.013 (Table 5.2) observed on the sample with the higher $[H^+]$. This demonstrates that the measured hydrogenation rate constants are invariant with $[H^+]$ and are thus unaffected by internal diffusional constraints.

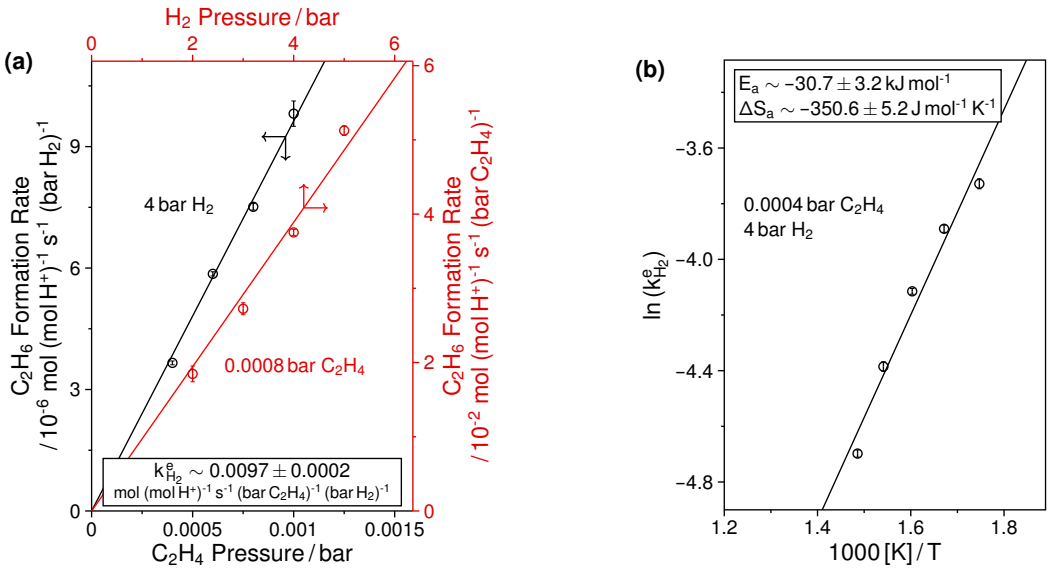

Fig. 5.8: Dependence of ethane formation rates (per H^+) on (a) partial pressures of the hydrocarbon (*bottom-left* axes) and H_2 (*top-right* axes) at 673 K and (b) temperature at fixed partial pressures of ethene and H_2 during hydrogenation of ethene over HFER (Zeolyst CP914).

Chapter 6

Kinetics of aromatics hydrogenation over HBEA

6.1 Abstract

Zeolite HBEA catalyzes hydrogenation of aromatic hydrocarbons – methyl-substituted benzenes (benzene and toluene), alkenyl-substituted benzenes (styrene), and polycyclics (naphthalene) in the presence of excess H_2 at high-temperatures (573 – 748 K) with rates that depend linearly on the aromatic hydrocarbon and H_2 pressures. The observed kinetic behavior can be rationalized based on a sequence of elementary steps where the first hydrogenation step of the quasi-equilibrated benzenic intermediate formed on the zeolitic protons is rate-determining while other hydrogenation and desorption steps are quasi-equilibrated and H^+ is the most abundant surface intermediate. Among the hydrocarbons considered, styrene is the most reactive with H_2 resulting in the exclusive formation of ethylbenzene while keeping the benzene ring intact whereas hydrogenation of benzene/toluene and naphthalene results in the formation of their triply-hydrogenated 5-membered ring and doubly-hydrogenated ring-open analogs, respectively. Independent studies involving co-reaction of cyclohexene and methylcyclopentene with H_2 infer their facile hydrogenation and interconversion indicating that benzene hydrogenation to methylcyclopentane can occur via the intermediate formation of cyclohexadiene/methylcyclopentadiene and cyclohexene/methylcyclopentene.

6.2 Introduction

Solid Brønsted acid zeolites are commonly used materials for several acid-catalyzed reactions, *e.g.*, isomerization [157], disproportionation [158, 159], reforming [160], dehydration [161], acylation [162], carbonylation [102], transalkylation [163, 164], etc. due to their thermal stability and shape-selective nature [6–8, 165–168]. However, these materials are lesser known for hydrogenation reactions and are often instead used as supports for transition or noble metals for direct hydrogenation [169, 170], hydrocracking [9, 171] and hydroisomerization [172] applications. The ability of Brønsted acid sites in zeolites to activate H_2 for direct hydrogenation of olefins and monocyclic aromatics was initially demonstrated in the

1980s by Sano and co-workers [173–175], Gadalla et al. [176], and Kanai et al. [117]. Sano [177] implicated the acidic protons in HZSM-5 to be the active sites for hydrogenation of olefins by showing that the selectivity of C_2-C_3 paraffins was ∼25%C over a Fe/HZSM-5 sample (0.82 wt% Fe; Si/Al = 20) compared to ∼1%C over a Fe/silicalite sample (2.2 wt% Fe) during CO hydrogenation ($CO/H_2 \sim 1$) at 673 K, 9.8 bar, 1000 h^{-1}. Similarly, Sano and co-workers [174, 175, 177] demonstrated the active role of acidic protons in aromatics hydrogenation by showing that the conversion levels of benzene (H/C = 1) during its co-reaction with excess H_2 ($C_6H_6/H_2 = 3/97$) at 846 K, 39.3 bar, 5000 h^{-1} over HZSM-5 samples with fixed Si/Al (∼35) but with varying amounts of Fe (∼0.009 – 0.7 wt%) did not vary significant and the H/C ratio of effluent products was ∼1.4 over the sample with 0.009 wt% Fe loading compared to ∼1.5 in the case of higher Fe contents. In their study, benzene hydrogenation led to the formation of methane, ethane, propane, toluene, and xylenes while formation of the direct hydrogenated analogs—cyclohexane and methylcyclopentane—was only observed at lower temperatures (∼573 K).

Several experimental [112, 120, 178] and theoretical reports [118, 179] since have validated the ability of proton-form zeolites for catalyzing olefins hydrogenation, and it has been proposed that in the kinetic regime where the measured rates of paraffins formation vary linearly with olefin and H_2 pressures, this reaction occurs via a set of elementary steps that are the microscopic reverse of protolytic dehydrogenation of paraffins [120]. The results reported in Chapter 4 and in a recent report by Zhao et al. [150] have demonstrated that the hydrogenation ability of acidic protons can be exploited to significantly improve catalyst lifetime (>70× enhancement in total turnover capacity) during methanol-to-hydrocarbons (MTH) conversion over HSAPO-34 with H_2 cofeeds. The formation of formaldehyde in transfer dehydrogenation events involving methanol, and its involvement in electrophilic addition reactions with olefins and methyl-substituted benzenes facilitating the formation of polycyclics have been implicated as critical in catalyst deactivation during methanol conversion over zeolites (Scheme 6.1) [43, 60, 61, 99, 106, 145]. The observed improvements in lifetime with H_2 cofeeds during methanol conversion therefore suggest that cofeeding H_2 intercepts formaldehyde-mediated alkylation pathways via preferential hydrogenation of the unsaturated intermediates formed during polycyclics production. In support of this proposal, we reported in Chapter 5 results from independent kinetic studies of ethene, propene, and 1,3-butadiene hydrogenation over various zeolites (HSSZ-13, HSSZ-39, HFER, and HBEA) wherein it was observed that the measured hydrogenation rate constants of 1,3-butadiene were at least one order of magnitude (∼7× to ∼320×) higher than the corresponding values for ethene and propene over all zeolites considered. Zhao et al. [150] showed that the composition of entrained hydrocarbons shifts from large polycyclics to light aromatics upon treatment of a deactivated HSAPO-34 sample with high-pressure (∼13 bar) H_2 feed. Although this demonstration in addition to the ones reported by Sano and co-workers [174, 175, 177] evinces the ability of acidic zeolites to effect aromatics hydrogenation, no rates,

mechanisms, or pathways of the involved reactions were presented.

Herein, we report results from kinetic studies of several aromatic compounds (benzene, toluene, styrene, and naphthalene) over HBEA, which exhibits a 3-dimensional system of mutually intersecting straight 12-membered ring channels with large pore openings (6.4×7.6 Å along [100] and 5.5×5.5 Å along [001]) that allow diffusion of aromatics in and out of the zeolite channels [180]. We rationalize the observed linear dependence of the measured hydrogenation turnover rates (per H^+) on the reactant pressures based on a sequence of elementary steps where the first hydrogenation step of the quasi-equilibrated Brønsted acid-bound aromatic intermediate is rate-determining. We report a quantitative kinetic model that evinces that ring-reduction during benzene hydrogenation to methylcyclopentane can take place via a combination of the 'C6 pathway' (involving the intermediate formation of cyclohexadiene and cyclohexene) and the 'C5 pathway' (involving the intermediate formation of methylcyclopentadiene and methylcyclopentene). We also note that the higher reactivity with H_2 exhibited by styrene and naphthalene compared to benzene/-toluene provides corroborating evidence to the aforementioned proposal stating that H_2 cofeeds result in the interception of formaldehyde-mediated pathways thereby leading to longer catalyst lifetimes during MTH.

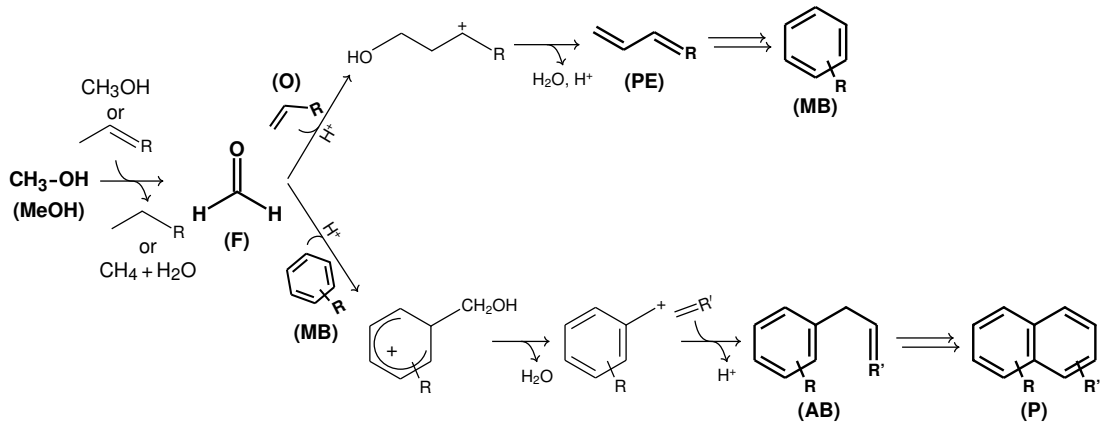

Scheme 6.1: Schematic illustrating formation of formaldehyde (F) from transfer dehydrogenation of methanol (MeOH) with itself or an olefin and its involvement in Prins reaction pathways with olefins (O) and methyl-substituted benzenes (MB) resulting in the formation of unsaturated intermediates—polyenes (PE) and alkenyl-substituted benzenes (AB)—that eventually transform to polycyclics (P) during methanol conversion over acidic zeolites. Reaction scheme adapted from [43].

6.3 Materials and Methods

6.3.1 Catalyst characterization

Zeolite BEA was sourced from Zeolyst (CP814E) in its ammonium-form and converted to the proton-form by thermal treatment in flowing dry air (1.67 $cm^3\,s^{-1}$; Zero Grade, Matheson) at 823 K (0.0167 $K\,s^{-1}$ ramp rate from RT) for 4 h. The framework type was confirmed as BEA by powder X-ray Diffraction (XRD) collected using a Bruker micro-diffractometer with Cu-K_α ($\lambda = 1.54$ Å) as the radiation source (Fig. 6.4a). The t-plot micropore volume (0.16 $cm^3\,g^{-1}$) and Brunauer-Emmett-Teller (BET) surface area (530 $m^2\,g^{-1}$) of the sample were obtained from N_2 adsorption measurements collected at 77 K using ASAP 2020 (Micromeritics). The sample was degassed by evacuating the sample tube to $\leq$10 µmHg at 363 K (0.083 $K\,s^{-1}$ ramp rate from RT) followed by thermal treatment in vacuo at 723 K (0.083 $K\,s^{-1}$ ramp rate from 363 K) for 4 h prior to N_2 adsorption. The adsorption-desorption isotherms are shown in Fig. 6.4b. The average crystallite size of the sample was ascertained as ~500 µm from the Scanning Electron Microscopy (SEM) images (Fig. 6.6). The bulk Si/Al atomic ratio of ~12.5 was determined from Scanning Electron Microscopy with Energy Dispersive X-ray Spectroscopy (SEM-EDS) measurements, and matches closely with the value of 17.6 measured in the near-surface region obtained from X-ray Photoelectron Spectroscopy (XPS) measurements indicating that Al is uniformly distributed in the lattice. The Brønsted acid site density was obtained from NH_3 temperature programmed desorption (0.33 $mmol\,g^{-1}$) and pyridine IR (0.26 $mmol\,g^{-1}$) measurements as reported earlier in Chapter 5. We note that the two site counts are within a factor of 0.8, therefore to be consistent with the other kinetic results reported in Chapter 5 for ethene, propene, and 1,3-butadiene hydrogenation over this sample, all rate constants reported herein are obtained after normalization of the observed rates by the site count measured from NH_3 TPD.

6.3.2 Catalytic testing

All experiments were performed in a borosilicate glass-lined stainless steel reactor tube (6.35 mm outer diameter and 4 mm inner diameter; Scientific Glass Engineering). The proton-form zeolite sample was subject to pelletization, crushing, and sieving to retain 180-250 µm (60-80 mesh) aggregates which were physically mixed with aggregates of sand (Acros Organics; subjected prior to an overnight wash in 2 M HNO_3 solution followed by deionized water rinse until pH ~7, and a final thermal treatment in flowing dry air (1.67 $cm^3\,s^{-1}$) at 1273 K (0.083 $K\,s^{-1}$ ramp rate from RT) for 16 h; $10 < wt_{diluent}/wt_{cat} < 15$) and packed in the middle of the reactor tube between quartz wool (Technical Glass Products) plugs. The tubular reactor was placed inside a resistively heated furnace (Model 3210, Applied Test Systems), and the reaction temperature was measured using a K-type thermocouple (TJ36-CAXL-020U-12, Omega) wrapped around the reactor periphery with the tip placed near the axial-center and regulated with an electronic controller (Series 96, Watlow). The

free volume above and below the catalyst bed was filled by quartz rods (3 mm O.D.; Technical Glass Products) to prevent any vertical displacement of the catalyst bed. Prior to catalytic measurements, the catalyst bed was pretreated in flowing dry air (1.67 $cm^3 s^{-1}$) at 823 K (0.0167 $K s^{-1}$ ramp rate from RT) for 4 h before being allowed to cool down to 673 K and being subject to a He (1.67 $cm^3 s^{-1}$; 99.997%, Matheson) purge at 673 K for $\geq$2 h. All gas flows including H_2 (99.9999%, Matheson), He, and Ar (99.9995%, Matheson) were metered using mass flow controllers (Model 5850E, Brooks). Liquid reagents including benzene ($\geq$99.0%, ACS Reagent, Sigma-Aldrich), cyclohexene ($\geq$99.0%, Sigma-Aldrich), 1-methyl-1-cyclopentene ($\geq$98.0%, Sigma-Aldrich), toluene ($\geq$99.9%, HPLC Plus, Sigma-Aldrich), styrene ($\geq$99.0% with 4-*tert*-butylcatechol as stabilizer which was removed prior to use with an alumina-based inhibitor remover (product #306320, Sigma-Aldrich), ReagentPlus®, Sigma-Aldrich), ethylbenzene (99.8%, anhydrous, Sigma-Aldrich), and p-xylene ($\geq$99.0%, puriss. p.a. Sigma-Aldrich) were delivered using a syringe pump (Legato 100, KD Scientific), vaporized in heat traced lines ($\sim$358 K), and swept by the flowing gas stream. Naphthalene (99%, Sigma-Aldrich) is a solid at room temperature, and was therefore dissolved and fed as a mixture with benzene (naphthalene/benzene $\sim$ 35). Cyclohexene, 1-methyl-1-cyclopentene, and styrene were also fed as a dilute mixture with toluene (R/-toluene $\sim$ 370 – 525) in order to obtain their low inlet partial pressures (0.04 – 0.30 $\times 10^{-5}$ bar) which was necessary to eliminate any secondary reactions and to obtain high selectivity of products resulting from their direct hydrogenation with H_2. Control experiments were performed with He cofeeds instead of H_2 in order to verify that the observed hydrogenation was a consequence of direct hydrogen transfer from H_2 and not due to intermolecular hydrogen transfer between hydrocarbons. The total gas-phase pressure was measured using a pressure transducer (0 – 6890 kPag; PX32B1-1KGV, Omega) placed upstream of the reactor tube, and controlled using a back-pressure regulator (0 – 3440 kPag; 44-2300 series, Tescom) placed downstream of the reactor tube. The composition of the reactant and product streams was characterized and quantified using a gas chromatograph (Model 7890A, Agilent) equipped with a dimethylpolysiloxane HP-1 column (50 m $\times$ 320 µm $\times$ 0.52 µm) connected to a flame ionization detector and a mass spectrometer (Model 5975C, Agilent) for detection of hydrocarbons, and a GS-GasPro column (60 m $\times$ 320 µm) connected to a thermal conductivity detector for detecting permanent gases (H_2 and Ar).

6.4 Results

6.4.1 Hydrogenation of methyl-substituted benzenes over HBEA

Benzene and toluene were chosen as the representative methyl-substituted benzenes in this study. Reactions of benzene and toluene with excess H_2 (H_2/R > 1500, where R = C_6H_6/C_7H_8) at 673 K on HBEA under differential conditions (<0.1% conversion) resulted in the formation of methylcyclopentane in the case of benzene, and a combination

of dimethylcyclopentanes, ethylcyclopentane and methylcyclohexane in the case of toluene, as shown in Scheme 6.2. As seen in Fig. 6.5a-b, the measured hydrogenation rates of benzene and toluene showed a weak dependence on the space velocity evidencing that the rate measurements were not influenced by secondary conversions or product inhibition. Further, using the Weisz-Prater criterion [151], it was verified that the measured rates were not corrupted by internal diffusion limitations and reflect solely the propensity of protons to catalyze the hydrogenation reactions under study (Table 6.2). Fig. 6.1 shows that the measured rates of benzene and toluene hydrogenation normalized by the total Brønsted acid sites (H^+) in the catalyst bed depend linearly on the partial pressures of both the aromatic hydrocarbon (p_R) and H_2 (p_{H_2}), and can be described by the rate expression shown in Eq. 6.1.

$$\frac{r}{[H^+]} = k^R_{H_2} p_R p_{H_2} \,. \tag{6.1}$$

The term $k^R_{H_2}$ in Eq. 6.1 represents an effective second-order rate constant and can be enumerated as the slope of the linear fit to the observed rate measurements as a function of the aromatic or H_2 pressures. The values ($k^{C_6H_6}_{H_2}$ and $k^{C_7H_8}_{H_2}$) thus obtained in the case of benzene and toluene hydrogenation over HBEA at 673 K are (0.0012 ± 0.0002) and (0.0033 ± 0.0004), respectively, with the corresponding units as mol $(\text{mol}\,H^+)^{-1}\,s^{-1}$ $(\text{bar}\,R)^{-1}\,(\text{bar}\,H_2)^{-1}$. The temperature dependence of the measured rate constants is presented in Fig. 6.7 and can be described by the Arrhenius expression (Eq. 6.8). This description allows enumeration of the apparent enthalpic and entropic barriers for hydrogenation of benzene and toluene over the HBEA sample, and the corresponding values are tabulated in Table 6.3.

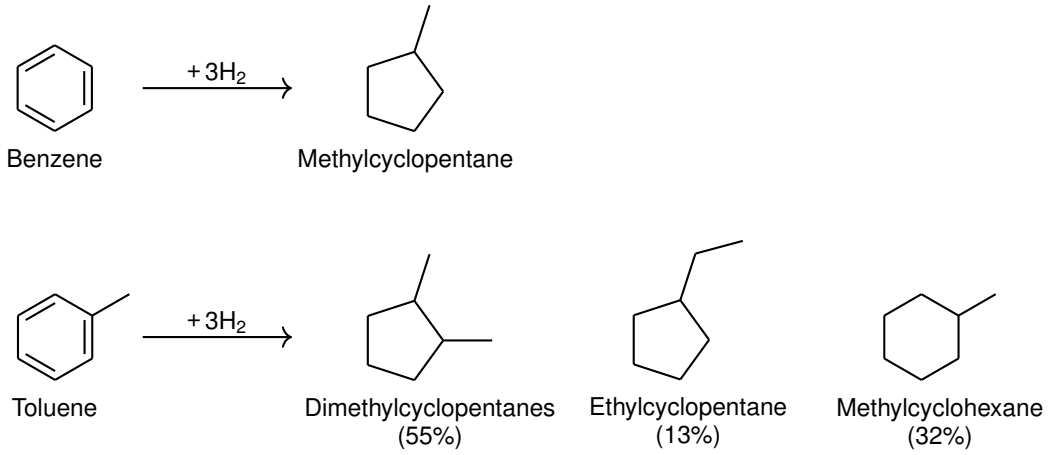

Scheme 6.2: Schematic showing the typical product distribution observed during benzene and toluene hydrogenation over HBEA at 673 K. The conversion level in case of toluene hydrogenation was ~0.06% during its feed at 0.0016 bar with 3.0 bar H_2 at 24.9 $\text{mol}_{C_7H_8}\,(\text{mol}_{H^+}\cdot\text{ks})^{-1}$ and 3.07 bar total pressure (including 0.068 bar Ar).

The observed linear dependence of measured turnover rates of benzene and toluene hydrogenation over HBEA (Eq. 6.1) can be realized by the set of elementary steps shown

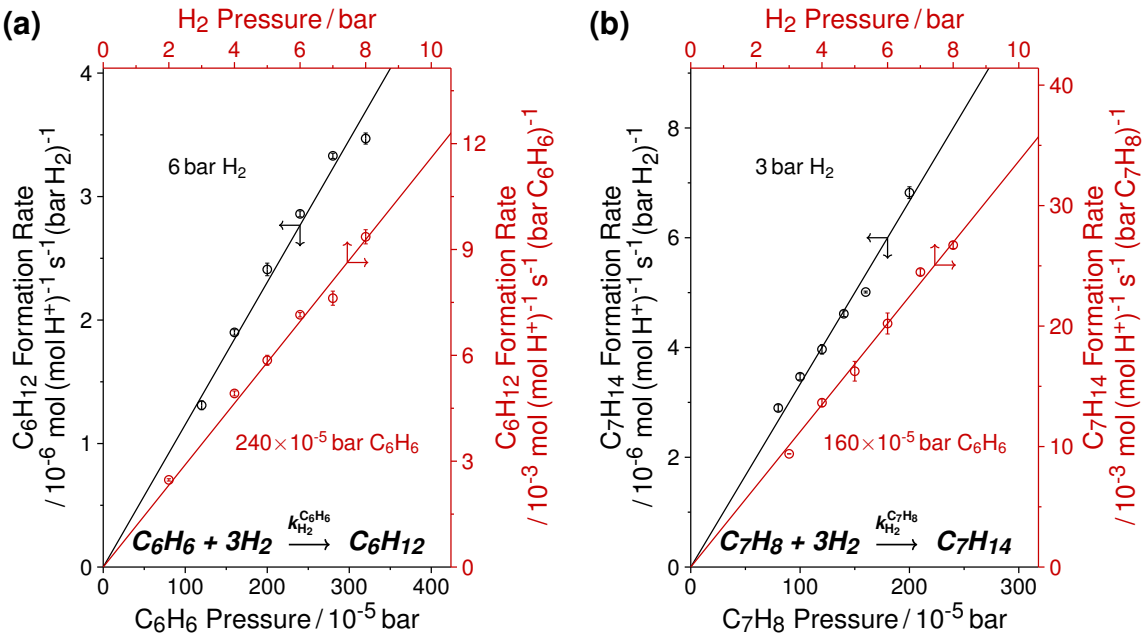

Fig. 6.1: Dependence of the turnover rates (per H^+) of (a) benzene and (b) toluene hydrogenation on partial pressures of the aromatic (*bottom-left* axes) and H_2 (*top-right* axes) during their reaction at 673 K and (a) 18.7 – 49.8 $mol_{C_6H_6}$ $(mol_{H^+} \cdot ks)^{-1}$; (b) 19.9 – 53.0 $mol_{C_7H_8}$ $(mol_{H^+} \cdot ks)^{-1}$ over HBEA. The quantities listed along each line indicate the partial pressure of either the aromatic hydrocarbon or H_2 held constant while varying the partial pressure of the other reagent during the kinetic measurements. The vertical bars on each data point represent the standard-error associated with each measurement. The solid lines represent a linear fit to the experimental data. The total gas-phase pressure of the reactant stream varied from 2.07 – 8.07 bar (including 0.068 bar Ar) during the experiments.

in Scheme 6.3 under the following assumptions: i) the fourth step involving the first hydrogenation reaction between the surface intermediate derived from the hydrocarbon reactant (RH^+) and intrazeolite H_2 species ($H_2\,(z)$) is rate-determining, ii) all other hydrogenation steps and steps involving the adsorption/desorption of the reactants and products into and out of the zeolite channels are quasi-equilibrated, and iii) Brønsted acid sites (H^+) are the most abundant surface species.

The selective formation of the 5-membered ring hydrogenated analogs during benzene and toluene hydrogenation over HBEA is unlike the case over metals-based catalysts where the primary products typically formed are cyclohexane and methylcyclohexane, respectively [169]. This observation is consistent with (i) the higher stability of 5-membered ring cycloalkanes compared to their six-membered ring analogs as predicted by thermodynamic considerations (calculated ΔG_f^o (623 K) $\sim -338.2\,kJ\,mol^{-1}$ for methylcyclopentane compared to $\sim -329.9\,kJ\,mol^{-1}$ for cyclohexane; see Section 6.7.5 for the calculations), and the ability of acid zeolites to promote the formation of carbenium ions that evolve

$R\,(g)$	$\overset{k_1}{\underset{k_{-1}}{\rightleftharpoons}}$	$R\,(z)$	K_1
$H_2\,(g)$	$\overset{k_2}{\underset{k_{-2}}{\rightleftharpoons}}$	$H_2\,(z)$	K_2
$R\,(z) + H^+$	$\overset{k_3}{\underset{k_{-3}}{\rightleftharpoons}}$	RH^+	K_3
$\mathbf{RH^+ + H_2\,(z)}$	$\xrightarrow{k_4}$	$\mathbf{RH_3{}^+}$	$\mathbf{K_4}$
$RH_3{}^+ + H_2\,(z)$	$\overset{k_5}{\underset{k_{-5}}{\rightleftharpoons}}$	$RH_5{}^+$	K_5
$RH_5{}^+ + H_2\,(z)$	$\overset{k_6}{\underset{k_{-6}}{\rightleftharpoons}}$	$RH_6\,(z) + H^+$	K_6
$RH_6\,(z)$	$\overset{k_7}{\underset{k_{-7}}{\rightleftharpoons}}$	$RH_6\,(g)$	K_7

$$r = k_4\,[RH^+]\,[H_2(z)]$$

$$\frac{r}{[H^+]} = \underbrace{k_4 K_3 K_2 K_1}_{k^R_{H_2}}\, p_R p_{H_2}$$

Scheme 6.3: Elementary steps proposed for hydrogenation of aromatic hydrocarbons [R = C_6H_6/C_7H_8] with H_2 over HBEA. The step highlighted in bold is considered as rate-determining. The notations g and z in the parenthesis denote the gas phase and intrazeolite phase, respectively.

through alkyl and hydride rearrangements toward the thermodynamically more stable form [9, 181]. The observed linear dependence of the measured hydrogenation rates on the reactant pressures and the corresponding interpretation that the first hydrogenation step is the rate-determining step implies that it is kinetically infeasible to ascertain when the ring-reduction takes place during the three hydrogenation steps since the intermediate species will react rapidly to the final observed products, or in other words, $k_1^{C6/C5} \ll k_2^{C6/C5}$ or $k_3^{C6/C5}$ (Scheme 6.4). To further validate this, we carried out independent studies involving hydrogenation of cyclohexene and 1-methyl-1-cyclopentene over HBEA in order to enumerate the values of k_3^{C6} and k_3^{C5} for comparison with $k_1^{C6/C5} (= k_{H_2}^{C_6H_6})$ reported earlier.

Co-feeding cyclohexene and 1-methyl-1-cyclopentene (diluted with toluene) independently with excess H_2 ($H_2/R > 33{,}000$) resulted in the formation of methylcyclopentane, however, in both cases facile interconversion between cyclohexene and methylcyclopentenes was also observed which was independent of the cofeed identity among H_2 or He. Scheme 6.5 shows the effluent product distribution observed while feeding cyclohexene or 1-methyl-1-cyclopentene with H_2 under identical reaction conditions. Therefore, in order to enumerate the values of their hydrogenation rate constants (k_3^{C6} and k_3^{C5}, respectively) while considering their disposition to interconvert, we considered an integral packed bed model with

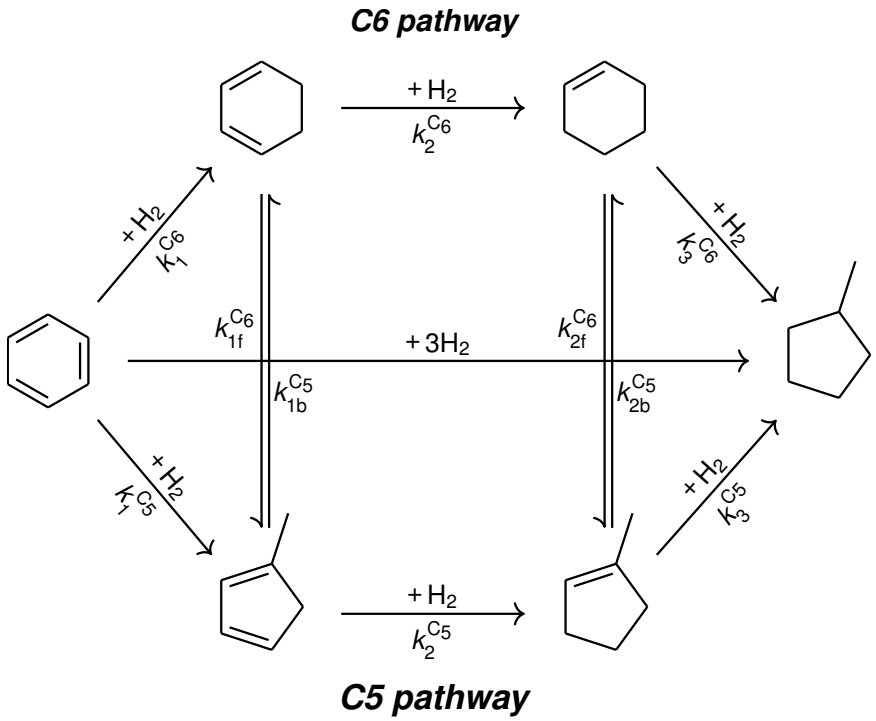

Scheme 6.4: Schematic showing the sequential hydrogenation steps during co-reaction of benzene and H_2 over HBEA leading to the formation of methylcyclopentane. The top pathway involving the transient formation of cyclohexadiene and cyclohexene is referred as the 'C6 pathway' and the bottom pathway involving the transient formation of methylcyclopentadiene and methylcyclopentene is referred as the 'C5 pathway'.

plug-flow hydrodynamics with the corresponding material balance equations shown in Eqs. 6.2 – 6.4.

$$\frac{d\dot{n}_i}{dw} = \sum_j r_{i,j}(k_j, p_j)\,, \tag{6.2}$$

$$\left(\frac{\dot{V}}{RT}\right)\frac{d(p_i/p_\mathrm{o})}{d(w/w_\mathrm{o})} = \sum_j r_{i,j}(k_j, p_j/p_\mathrm{o}) \times w_\mathrm{o}\,, \tag{6.3}$$

$$\left(\frac{\dot{V}}{RT}\right)\frac{d(p_i/p_\mathrm{o})}{dy} = \sum_j r_{i,j}(k_j, p_j/p_\mathrm{o}) \times w_\mathrm{o}\,, \tag{6.4}$$

where $\dot{n}$ represents the molar flow rate of species i measured at ambient conditions (295 K and 1 atm), w represents the number of H^+ in the catalyst bed, $\sum_j r_{i,j}$ represents the net rate of formation of species i from j reactions, k_j represents the unknown rate constant of reaction j, p_i or p_j represent the instantaneous partial pressures of species i/j along the catalyst bed, $\dot{V}$ represents the total volumetric flow rate of the inlet feed measured at ambient conditions, p_o represents the inlet partial pressure of the reactant, and w_o represents the total number of H^+ in the catalyst bed. The boundary condition for this model is: @$y = 0$, $p_i/p_\mathrm{o} = 1$ for reactants and 0 for products.

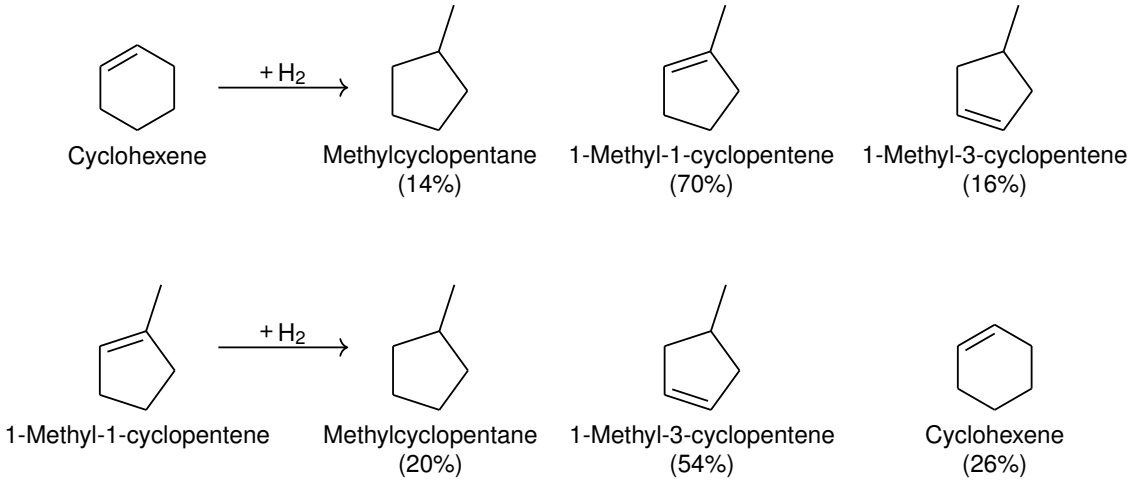

Scheme 6.5: Schematic showing effluent product distribution observed during co-reaction of 0.11×10^{-5} bar cyclohexene or 1-methyl-1-cyclopentene with 0.15 bar H_2 over HBEA at 623 K and 0.15 $mol_{C_6H_{10}}$ $(mol_{H^+} \cdot ks)^{-1}$ with corresponding conversion levels of 88% and 26%. The overall composition of the reactant stream was 0.11×10^{-5} bar cyclohexene/1-methyl-1-cyclopentene, 59×10^{-5} bar toluene, 0.15 bar H_2, 1.35 bar He and 0.026 bar Ar, and the total pressure was 1.52 bar.

The two methylcyclopentene isomers were lumped together as one species, and the rates of the interconversion reactions between cyclohexene and methycyclopentenes were considered to depend linearly on the partial pressure of the reactants while the rates of their hydrogenation reactions were considered to depend linearly on the partial pressures of both the hydrocarbon and H_2. Under these assumptions, the corresponding material balance equations for solving the partial pressure profiles of the three species involved—(1) cyclohexene, (2) methylcyclopentenes, and (3) methylcyclopentane—are shown in Eqs. 6.5 – 6.7.

$$\left(\frac{\dot{V}}{RT}\right)\frac{d(p_1/p_o)}{dy} = [k_{2b}^{C5}\,(p_2/p_o) - k_{2f}^{C6}\,(p_1/p_o) - k_3^{C6}\,(p_1/p_o)\,p_{H_2}] \times w_o\,. \tag{6.5}$$

$$\left(\frac{\dot{V}}{RT}\right)\frac{d(p_2/p_o)}{dy} = [k_{2f}^{C6}\,(p_1/p_o) - k_{2b}^{C5}\,(p_2/p_o) - k_3^{C5}\,(p_2/p_o)\,p_{H_2}] \times w_o\,. \tag{6.6}$$

$$\left(\frac{\dot{V}}{RT}\right)\frac{d(p_3/p_o)}{dy} = [k_3^{C6}(p_1/p_o)p_{H_2} + k_3^{C5}(p_2/p_o)p_{H_2}] \times w_o\,. \tag{6.7}$$

We used the 'ode45' function in MATLAB to solve for the partial pressure profiles along the catalyst bed ($y = 0{:}1$) and 'lsqcurvefit' to ascertain the estimates of the four unknown parameters—k_{2f}^{C6}, k_{2b}^{C5}, k_3^{C6}, and k_3^{C5}—while minimizing the difference between the values of p_i/p_o at $y = 1$ obtained from the MATLAB simulations and those observed during experiments (see Section 6.7.6 for the code). In total, 44 different data sets, including variations in the inlet partial pressures of cyclohexene/methylcyclopentene ($0.09 - 0.21 \times 10^{-5}$ bar) and

H_2 (0.075 – 0.375 bar) while keeping the total pressure fixed at 1.52 bar (balanced by a combination of toluene, argon, and helium), and variations in the inlet space velocities of cyclohexene/methylcyclopentene (0.09 – 0.53 $mol_{C_6H_{10}}$ $(mol_{H^+} \cdot ks)^{-1}$) were fitted together to estimate the unknown kinetic parameters and the corresponding values along with their 95% confidence interval values are listed in Table 6.1. Fig. 6.2 shows the parity plot between the simulated and experimentally observed exit partial pressures of the three species.

Table 6.1: Estimates of the kinetic parameters dictating interconversion between cyclohexene and methylcyclopentenes, and their hydrogenation to methylcyclopentane at 623 K over HBEA along with their 95% confidence interval values obtained using MATLAB. Scheme 6.5 shows the correspondence between the different kinetic parameters and the specific reactions they dictate.

Kinetic parameter	Estimated value	Units
k_{2f}^{C6}	481.6 ± 11.17	mol $(mol\,H^+)^{-1}$ s^{-1} $(bar\,R)^{-1}$
k_{2b}^{C5}	48.02 ± 3.972	mol $(mol\,H^+)^{-1}$ s^{-1} $(bar\,R)^{-1}$
k_{3}^{C6}	207.0 ± 21.16	mol $(mol\,H^+)^{-1}$ s^{-1} $(bar\,R)^{-1}$ $(bar\,H_2)^{-1}$
k_{3}^{C5}	45.17 ± 7.080	mol $(mol\,H^+)^{-1}$ s^{-1} $(bar\,R)^{-1}$ $(bar\,H_2)^{-1}$

As shown in Fig. 6.7, the hydrogenation rate constant of benzene at 623 K is ∼0.00029 mol $(mol\,H^+)^{-1}$ s^{-1} $(bar\,C_6H_6)^{-1}$ $(bar\,H_2)^{-1}$ which is significantly lower (∼156,000 – 715,000×) than the hydrogenation rate constants of either cyclohexene or methylcyclopentenes, evidencing that the intermediate species formed after the first hydrogenation step react rapidly to the final product. Furthermore, we observe that although the hydrogenation rate constant of cyclohexene is higher (∼4.6×) than the corresponding value for methylcyclopentenes, the rate constant for its conversion to methylcyclopentenes is also higher (∼10×) than the corresponding value for the conversion of methylcyclopentenes to cyclohexene. This consideration suggests that hydrogenation of benzene to form methylcyclopentane can occur via a combination of the 'C6' and 'C5' pathways.

6.4.2 Hydrogenation of alkenyl-substituted benzenes and polycyclics over HBEA

Styrene and Naphthalene were chosen as the representative alkenyl-substituted benzene and polycyclic in this study. Reactions of styrene (diluted with toluene) and naphthalene (diluted with benzene) with excess H_2 ($H_2/R > 28{,}000$) at 673 K on HBEA under differential conditions (<11%C conversion) resulted in the exclusive formation of ethylbenzene in the case of styrene, and a combination of 1,4-dihydronaphthalene, tetralin, 1-methyl-1-propenyl-benzene, 1-ethenyl-4-ethyl-benzene, and 1-propenyl-benzene (likely resulting from protolytic cracking of 1-methyl-1-propenyl-benzene with the corresponding methyl group reacting with benzene and naphthalene in the feed to form toluene and methylnaphthalene,

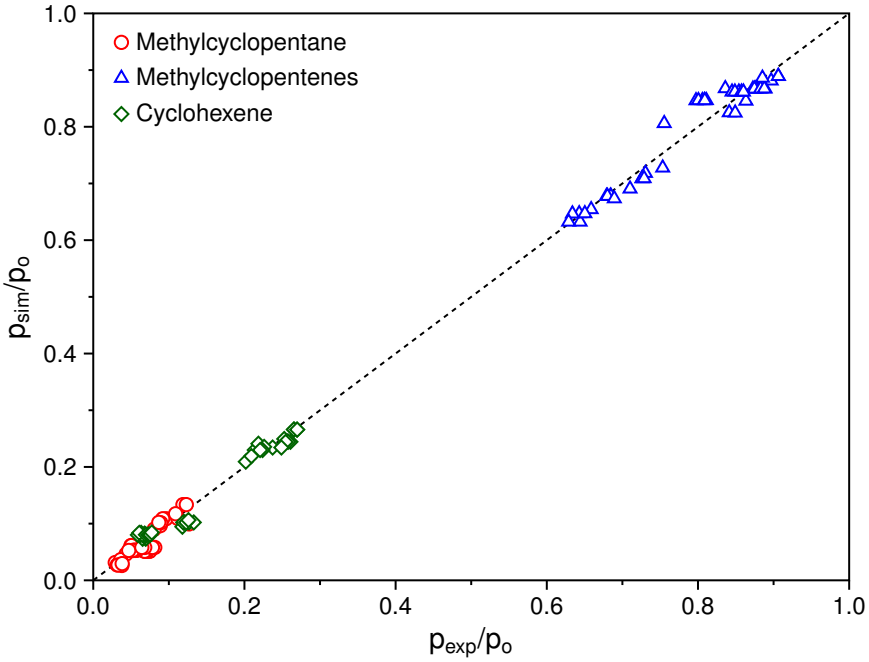

Fig. 6.2: Parity plot between the simulated (p_{sim}) and experimentally (p_{exp}) observed exit partial pressures (normalized by the inlet partial pressures of the reactant (p_0)) of cyclohexene (◇), methylcyclopentenes (△), and methylcyclopentane (○) during independent experiments involving co-reactions of cyclohexene or 1-methyl-1-cyclopentene ($0.09-0.21\times10^{-5}$ bar) with H_2 ($0.075-0.375$ bar) at 623 K and $0.09-0.53\,mol_{C_6H_{10}}\,(mol_{H^+}\cdot ks)^{-1}$ over HBEA. The overall composition of the reactant stream was $0.09-0.21\times10^{-5}$ bar cyclohexene/1-methyl-1-cyclopentene, $47.3-110.3\times10^{-5}$ bar toluene, $0.075-0.375$ bar H_2, $1.20-1.40$ bar He and 0.026 bar Ar, and the total pressure was 1.52 bar.

respectively, both of which were observed in the effluent) in the case of naphthalene as shown in Scheme 6.6. Fig. 6.3 shows that the turnover rates (per H^+) of both styrene and naphthalene hydrogenation vary linearly with the partial pressures of the respective reactant and H_2, as was the case during benzene and toluene hydrogenation (Fig. 6.1). This again stipulates that the observed kinetic behavior can be described by the rate expression shown in Eq. 6.1 and rationalized by the sequence of elementary steps shown in Scheme 6.3 where the first hydrogenation step is rate-determining regardless of the number of moles of H_2 incorporated in the effluent products. The temperature dependence of the measured hydrogenation rate constants of both styrene and naphthalene is shown in Fig. 6.7. From Fig. 6.3, the effective second-order rate constants are enumerated as (38.2 ± 5.7) for styrene hydrogenation at 623 K and (0.71 ± 0.24) for naphthalene hydrogenation at 673 K with the corresponding units being mol $(mol\,H^+)^{-1}\,s^{-1}\,(bar\,R)^{-1}\,(bar\,H_2)^{-1}$. For comparison with other hydrogenation rate constants reported at 673 K, the corresponding value for styrene is 68.1 mol $(mol\,H^+)^{-1}\,s^{-1}\,(bar\,C_8H_8)^{-1}\,(bar\,H_2)^{-1}$) as obtained from Fig. 6.7).

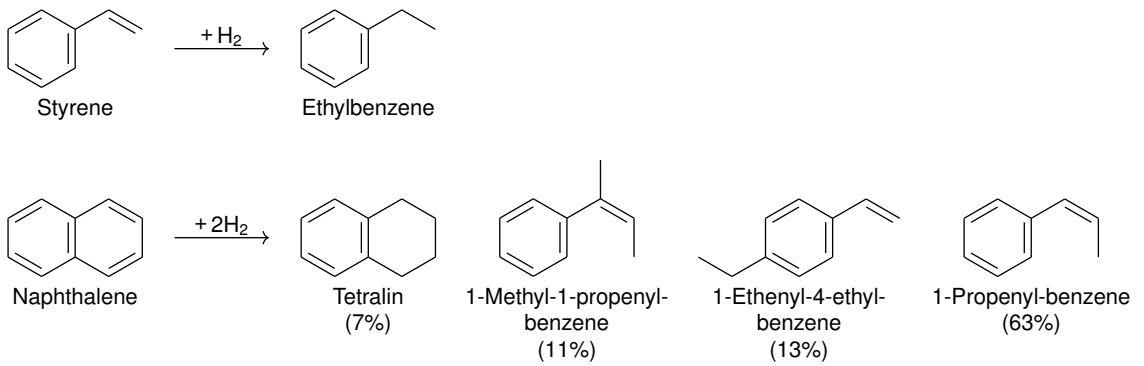

Scheme 6.6: Schematic showing the typical product distribution observed during styrene and naphthalene hydrogenation over HBEA at 673 K. In the case of naphthalene hydrogenation, the balance 6% selectivity belongs to the singly-hydrogenated analog of naphthalene—1,4-dihydro-naphthalene—and the overall conversion level was ∼4% during its feed at 8.7×10^{-5} bar with 3.02 bar H_2 and 4.7 $mol_{C_{10}H_8}$ $(mol_{H^+} \cdot ks)^{-1}$. The overall composition of the reactant stream was 8.7×10^{-5} bar naphthalene, 304.5×10^{-5} bar benzene, 3.02 bar H_2, and 0.068 bar Ar, and the total pressure was 3.09 bar.

6.5 Discussion

We note that while hydrogenation of benzene and toluene results primarily in the formation of their triply-hydrogenated 5-membered ring analogs, hydrogenation of styrene results only in the formation of ethylbenzene via hydrogenation of the ethenyl-substituent group while leaving the benzene ring intact (Schemes 6.2 and 6.6). Further, co-reacting ethylbenzene with excess H_2 ($H_2/C_8H_{10} \sim 10{,}000$) in independent studies also did not yield any hydrogenated analogs of ethylbenzene and instead, ethylbenzene underwent cracking to form benzene and ethene. Similarly, co-reacting p-xylene with excess H_2 ($H_2/C_8H_{10} \sim 1{,}200{,}000$) also did not result in the formation of its hydrogenated analogs and instead, p-xylene underwent isomerization to m-xylene, and disproportionation to toluene and trimethylbenzenes. These observations suggest that the presence of an alkyl-substituent or more than one methyl-substituent on the benzene ring introduce secondary reaction pathways which prevent the direct hydrogenation of the benzenic ring until the corresponding molecules transform to either benzene or toluene. The detailed mechanistic origins of this observation are still not yet fully understood.

As deduced by the differences in the measured rate constants, styrene and naphthalene are observed to exhibit significantly higher (∼20,300 – 58,900× and ∼210 – 620×, respectively) propensity for hydrogenation compared to benzene/toluene at 673 K. The higher reactivity of styrene with H_2 compared to benzene/toluene can be rationalized based on (i) the retainment of aromaticity in the singly-hydrogenated analog—ethylbenzene—observed during styrene hydrogenation compared to the triply-hydrogenated analogs observed in the case of benzene/toluene hydrogenation, and (ii) the presence of π delocalization in

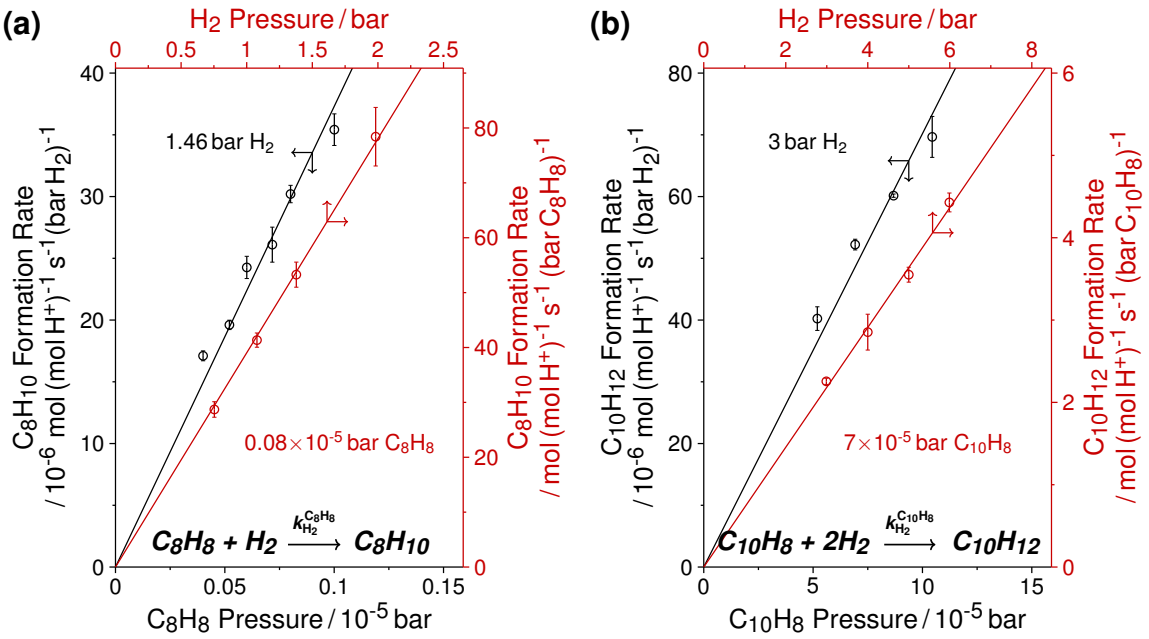

Fig. 6.3: Dependence of the turnover rates (per H^+) of (a) styrene and (b) naphthalene hydrogenation on partial pressures of the aromatic (*bottom-left* axes) and H_2 (*top-right* axes) during reactions of (a) styrene with H_2 at 623 K and 0.4 – 1.0 $mol_{C_8H_8}$ $(mol_{H^+} \cdot ks)^{-1}$, and (b) naphthalene with H_2 at 673 K and 2.7 – 5.3 $mol_{C_{10}H_8}$ $(mol_{H^+} \cdot ks)^{-1}$ over HBEA. The quantities listed along each line indicate the partial pressure of either the aromatic hydrocarbon or H_2 held constant while varying the partial pressure of the other reagent during the kinetic measurements. The vertical bars on each data point represent the standard-error associated with each measurement. The solid lines represent a linear fit to the experimental data. In the case of styrene hydrogenation, the overall composition of the reactant stream was $0.04 - 0.1 \times 10^{-5}$ bar styrene, $14.8 - 37.0 \times 10^{-5}$ bar toluene, 0.075 – 1.98 bar H_2 and 0.012 bar Ar, and the total pressure varied from 1.38 – 2.00 bar. In the case of naphthalene hydrogenation, the overall composition of the reactant stream was $5 - 10 \times 10^{-5}$ bar naphthalene, 0.00175 – 0.0035 bar benzene, 3.0 – 6.0 bar H_2 and 0.068 bar Ar, and the total pressure was 3.08 – 6.08 bar.

the benzyl carbenium ion ($C_6H_5 - CH^+ - CH_3$) that is likely formed upon interaction of the ethenyl-substitutent group in styrene with H^+ compared to the case of arenium ions ($C_6H_7^+$ or $C_6H_6^+ - CH_3$) likely formed upon the interaction of benzene/toluene with H^+ in step 3 of Scheme 6.3 [182]. The higher reactivity of naphthalene compared to benzene with H_2 over HBEA is consistent with similar reactivity trends observed over sulfided metal-based catalysts [183] and is likely rationalized based on the lower resonance energy per ring in naphthalene (∼117 kJ/mol) compared to benzene (∼167 kJ/mol) although the overall resonance stabilization is higher in naphthalene (∼314 kJ/mol) [169, 184].

In Chapter 5, we reported the effective second-order hydrogenation rate constants of ethene, propene, and 1,3-butadiene over this sample at 673 K as 0.020, 0.33, and 2.3, re-

spectively, in the same units as those used in this study. Comparing these values with those measured for benzene and toluene, we infer that both olefins and polyenes are more reactive (>6× higher rate constants) with H_2 than benzene/toluene, which can be likely ascribed to resonance stabilization present in the latter. Further, akin to the observation of higher reactivity with H_2 of alkenyl-substituted benzenes (styrene) compared to methyl-substituted benzenes (benzene and toluene), polyenes (1,3-butadiene) are observed to be more reactive (>7× higher rate constant) than olefins (ethene and propene). Overall, these observations indicate that both the unsaturated intermediates (polyenes and alkenyl-substituted benzenes) and polycyclics that result in formaldehyde-mediated alkylation pathways during methanol conversion (Scheme 6.1) are more prone to reaction with H_2, which underlies the observed effectiveness of high-pressure H_2 cofeeds in prolonging catalyst lifetimes during MTH over acidic zeolites.

6.6 Conclusions

Hydrogenation of benzene, toluene, styrene, and naphthalene with excess H_2 over HBEA under differential conditions occurs with rates that vary linearly with both the aromatic hydrocarbon and H_2 pressures implicating the first hydrogenation step to be rate-determining. Hydrogenation of benzene and toluene results primarily in the formation of their triply-hydrogenated 5-membered ring analogs. Independent kinetic studies of cyclohexene and methylcyclopentene hydrogenation reveal that the rate constants dictating their interconversion and hydrogenation to methylcyclopentane are significantly larger than the rate constant of benzene hydrogenation to methylcyclopentane, indicating the feasibility of the intermediate formation of cyclohexadiene/methylcyclopentadiene and cyclohexene/methylcyclopentene during benzene hydrogenation. Hydrogenation of styrene results in the exclusive formation of ethylbenzene while leaving the benzene ring intact. Co-reacting ethylbenzene or p-xylene with excess H_2 also does not result in the hydrogenation of the benzene ring, but instead these reactants undergo secondary reactions including cracking, isomerization, and disproportionation to yield benzene and toluene which further yield the 5-membered ring hydrogenated products. Based on the magnitudes of the measured rate constants, it is concluded that both alkenyl-substituted benzenes and polycyclics exhibit a higher predisposition for reaction with H_2 than methyl-substituted benzenes, thereby providing a mechanistic basis for the observed enhancements in catalyst lifetime during MTH with H_2 cofeeds over acidic zeolites.

Acknowledgements

We acknowledge (i) Dow through the University Partnership Initiative and the National Science Foundation (CBET 1701534) for financial support, (ii) Dr. Andrzej Malek, Dr. Davy L. S. Nieskens, and Dr. Joseph DeWilde from Dow for helpful technical discussions, (iii) Dr.

Nicholas Seaton from the University of Minnesota Characterization Facility, which receives partial support from the National Science Foundation through the Materials Research Science and Engineering Centers program, for providing the SEM-EDS measurements and SEM images of the HBEA sample, (iv) Mr. Xinyu Li from the University of Minnesota for providing the X-ray diffractogram and pyridine IR spectra of the HBEA sample, and (v) Ms. Zhichen Shi from the University of Minnesota for providing the NH_3 TPD data of the HBEA sample.

6.7 Supplementary Information

6.7.1 X-ray Diffraction and N_2 adsorption-desorption isotherms

Figs. 6.4a-b show the XRD pattern and the adsorption-desorption isotherms, respectively, of the HBEA sample that confirm its crystalline and microporous nature.

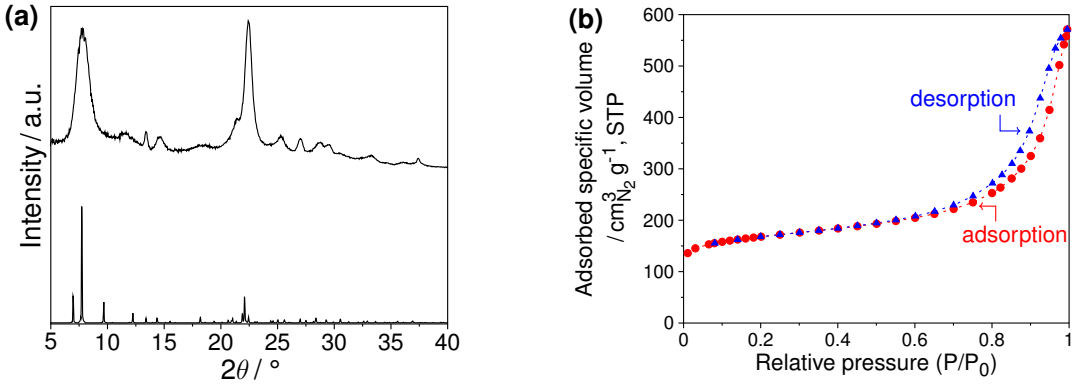

Fig. 6.4: (a) X-ray diffractogram of the HBEA sample (*top*) along with the reference diffractogram obtained from IZA [98] (*bottom*); (b) N_2 adsorption and desorption isotherms of the HBEA sample.

6.7.2 Check for space-velocity effects on rate measurements

As shown in Fig. 6.5a-b, the measured hydrogenation rates during reactions of benzene (0.0024 bar) with H_2 (2 bar), and toluene (0.0016 bar) with H_2 (4 bar) over HBEA at 673 K are weakly dependent on the space velocity (SV) of the aromatic reactant and are thus unaffected by secondary reactions or inhibition by products.

6.7.3 Check for effects of intracrystalline diffusional limitations

The absence of intracrystalline diffusional limitations on the rate measurements was confirmed by using the Weisz-Prater criterion [151]. The values tabulated in Table 6.2 show that the effectiveness factor (η) is $= 1$, which implies that the measured hydrogenation rates are not corrupted by internal mass transfer limitations. (Note: The diffusivity coefficient (D,

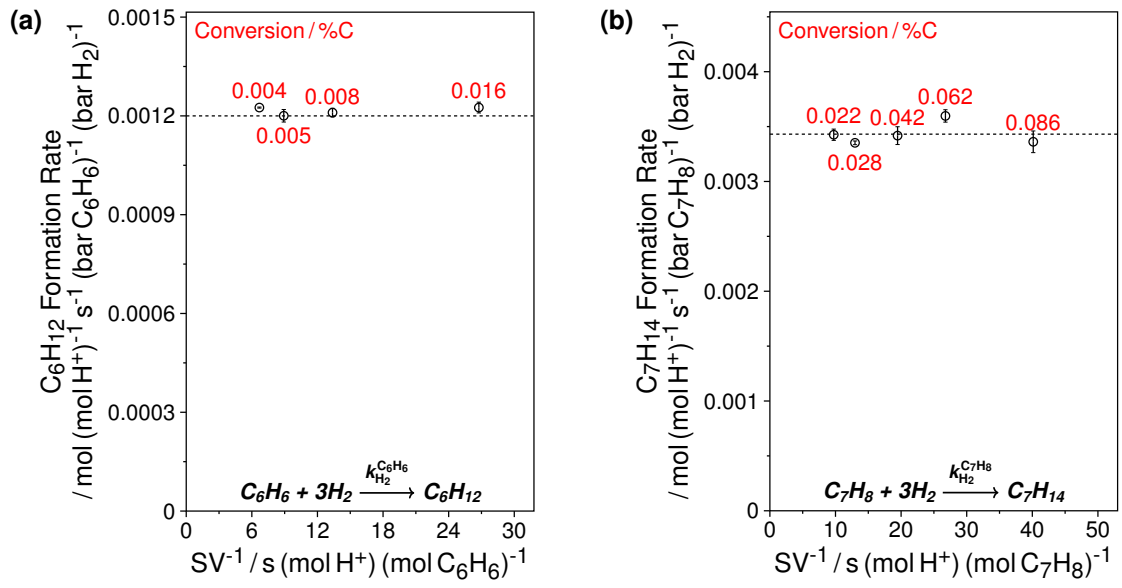

Fig. 6.5: Dependence of hydrogenation rates (per H^+) on space velocity (SV) during reactions of (a) benzene (0.0024 bar) with H_2 (2 bar), and (b) toluene (0.0016 bar) with H_2 (4 bar) over HBEA. The vertical bars on each data point represent the standard-error associated with each measurement and the dashed horizontal lines are drawn as a guide to the viewer in order to show that hydrogenation rates vary insignificantly with changes in the space-velocities of benzene and toluene during their hydrogenation with H_2 over HBEA at 673 K.

$\sim 2 \times 10^{-14}$ m^2 s^{-1} @ 300 K) of toluene in HBEA was obtained from [185] and the crystallite size (R, $\sim$500 µm) was estimated from scanning electron microscopy images (Fig. 6.6). The value of D/R^2 thus obtained provides a lower-bound on the diffusion rate since at reaction temperature of 673 K, the corresponding value will be higher. $(k_{H_2} p_{H_2})_{673\,K}$ represents the pseudo-first order hydrogenation rate constant measured at 673 K. Therefore, the Thiele modulus (ϕ) and the corresponding effectiveness factor (η) are calculated while considering the lower-bound on the diffusion rate and an upper-bound on the measured reaction rate.)

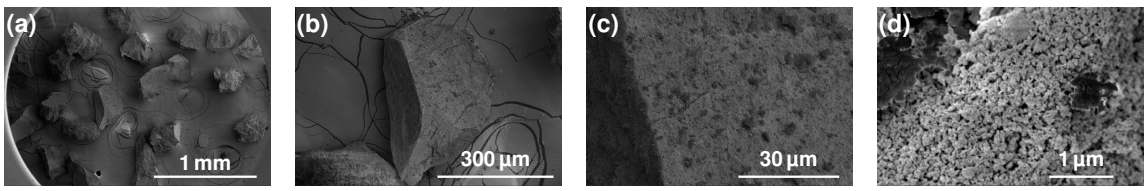

Fig. 6.6: SEM images of the HBEA sample at different magnification levels.

Table 6.2: Weisz-Prater criterion calculations for assessing effects of internal mass transfer limitations during toluene hydrogenation measurements on HBEA.

$[\mathbf{H^+}](\mathbf{R^2}/\mathbf{D_{C_7H_8\,@\,300\,K}})$	13.4	$(\mathrm{mol\,H^+})\,\mathrm{s}$
$(\mathbf{k_{H_2}p_{H_2}})_{\mathbf{673\,K}}$	2.6×10^{-7}	$(\mathrm{mol\,H^+})^{-1}\,\mathrm{s}^{-1}$
$\boldsymbol{\phi}\left[=\sqrt{(\mathbf{k_{H_2}p_{H_2}})_{\mathbf{673\,K}} \times [\mathbf{H^+}]\mathbf{R^2}/\mathbf{D}}\right]$	0.0019	
$\boldsymbol{\eta}\left[=\dfrac{\tanh\phi}{\phi}\right]$	1	

6.7.4 Temperature dependence of the measured hydrogenation rate constants

The temperature dependence of the measured hydrogenation rate constants of the different aromatic hydrocarbons is shown in Fig. 6.7 and can be described by the Arrhenius expression shown in Eq. 6.8.

$$k_{\mathrm{H_2}}^{\mathrm{R}} = A \exp\left(-\frac{E_{\mathrm{a}}}{RT}\right), \tag{6.8}$$

where A and E_{a} represent the pre-exponential factors and the apparent enthalpic barriers, respectively, for the hydrogenation reactions. The pre-exponential factors in Eq. 6.8 can be used to calculate the apparent entropic barriers (ΔS_{a}) after accounting for the number of C–H bonds (n_{b}) in the hydrogenated analogs of the reactants (12, 11, 5, and 8 in the case of benzene, toluene, styrene, and naphthalene, respectively) using Eq. 6.9, which follows the formalism reported by Gounder and Iglesia [152]. The experimentally measured values of these barriers for hydrogenation reactions of all the aromatic hydrocarbons considered over the HBEA sample are listed in Table 6.3.

$$\Delta S_{\mathrm{a}} = R\left[\ln\left(\frac{A}{n_{\mathrm{b}}}\right) - \ln\left(\frac{k_{\mathrm{B}}T}{h}\right)\right]. \tag{6.9}$$

Table 6.3: Apparent enthalpic (E_{a}; $[\mathrm{kJ\,mol^{-1}}]$) and entropic (ΔS_{a}; $[\mathrm{J\,mol^{-1}\,K^{-1}}]$) barriers for hydrogenation of benzene, toluene, styrene, and naphthalene over HBEA and their 95% confidence intervals.

Aromatic hydrocarbon	$\boldsymbol{E_{\mathrm{a}}}$ $(\mathrm{kJ\,mol^{-1}})$	$\boldsymbol{\Delta S_{\mathrm{a}}}$ $(\mathrm{J\,mol^{-1}\,K^{-1}})$
Benzene	89 ± 11	-196 ± 17
Toluene	59 ± 10	-230 ± 15
Styrene	33 ± 6	-181 ± 10
Naphthalene	63 ± 7	-177 ± 11

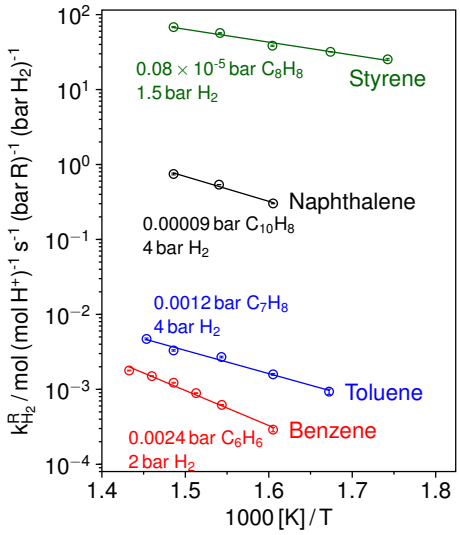

Fig. 6.7: Temperature dependence of the measured second-order hydrogenation rate constants of benzene, toluene, styrene, and naphthalene hydrogenation with H_2 over HBEA at 623 – 698 K. The pressures listed along each solid line represent the partial pressures of the hydrocarbon reactant and H_2 that were held constant while varying the temperature. The vertical bars on each data point represent the standard-error associated with each measurement. The solid lines represent an exponential fit to the experimental data.

6.7.5 Calculation of Gibbs free energies of formation

The standard enthalpies (ΔH_f^o) and entropies (ΔS_f^o) of formation of cyclohexane and methylcyclopentane at 298.15 K listed in Table 6.4 were obtained from NIST ([186] and [187], respectively). The functional forms of the variations in molar specific heats at constant pressure with temperature for both cyclohexane and methylcyclopentane were obtained by a second-order polynomial fit to the values reported by NIST [187] and are shown in Fig. 6.8.

Table 6.4: Standard enthalpies (ΔH_f^o) and entropies (ΔS_f^o) of formation of cyclohexane and methylcyclopentane at 298.15 K obtained from NIST ([186] and [187], respectively).

	Cyclohexane	Methylcyclopentane
$\Delta H^o_{f,\,298.15\,K}$ (kJ mol^{-1})	– 124.60	– 106.69
$\Delta S^o_{f,\,298.15\,K}$ (J mol^{-1} K^{-1})	298.19	339.82

Using Eqs. S3 and S4, the standard enthalpies and entropies of formation of cyclohexane and methylcyclopentane at 623 K were obtained to yield the respective standard Gibbs free

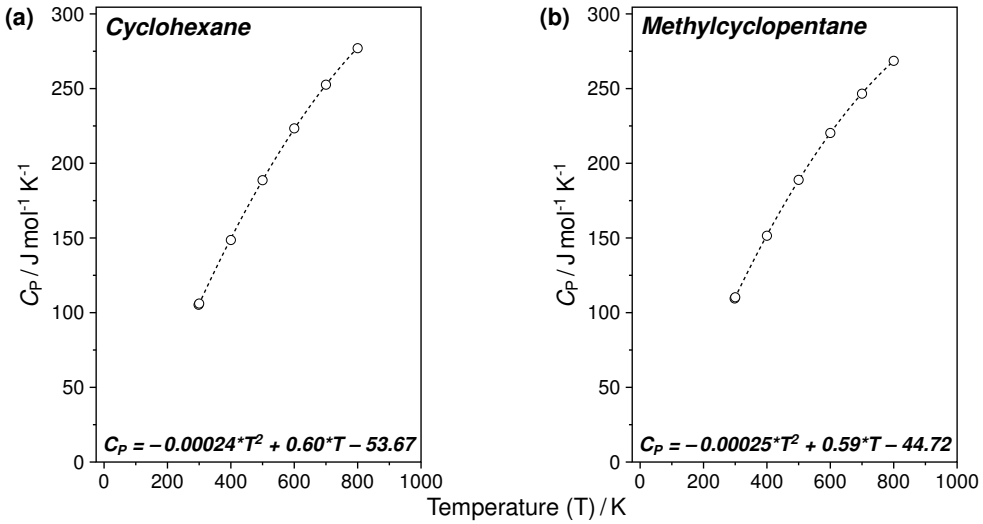

Fig. 6.8: Plots showing variations in the molar specific heats at constant pressure (C_{P}) with temperature for (a) cyclohexane and (b) methylcyclopentane. The dashed lines represent the second-order polynomial fit to the data obtained from NIST [187] and the corresponding functional forms of the polynomials are listed at the bottom of each plot.

energies of formation as -329.9 and $-338.2\,\mathrm{kJ\,mol^{-1}}$.

$$\Delta H^{\mathrm{o}}_{\mathrm{f},\,623\,\mathrm{K}} = \Delta H^{\mathrm{o}}_{\mathrm{f},\,298.15} + \int_{298.15}^{623} \frac{C_{\mathrm{P}}}{1000}\, dT\,. \tag{S3}$$

$$\Delta S^{\mathrm{o}}_{\mathrm{f},\,623\,\mathrm{K}} = \Delta S^{\mathrm{o}}_{\mathrm{f},\,298.15\,\mathrm{K}} + \int_{298.15}^{623} \frac{C_{\mathrm{P}}}{T}\, dT. \tag{S4}$$

6.7.6 MATLAB code for estimating kinetic parameters involved in cyclohexene and methylcyclopentene hydrogenation

The main source code is as follows.

```
clear;
clc;
global n p_fit p_profile
%cyhx=cyclohexene
%mcpo=methylcyclopentenes
%mcpp=methylycyclopentane
exp=[
0.1121  0.0266  0.0722  0.0133  0.3735  9.3392  0.0268
0.1128  0.0285  0.0743  0.0100  0.2632  9.3392  0.0268
0.1128  0.0304  0.0766  0.0059  0.1504  9.3392  0.0268
0.0896  0.0238  0.0613  0.0046  0.1494  9.3392  0.0268
0.1345  0.0357  0.0921  0.0067  0.1494  9.3392  0.0268
```

```
0.1579  0.0426  0.1074  0.0078  0.1504  9.3392  0.0268
0.1568  0.0409  0.1008  0.0151  0.2988  9.3392  0.0268
0.1121  0.0289  0.0729  0.0103  0.2988  9.3392  0.0268
0.1128  0.0287  0.0715  0.0126  0.3008  9.3392  0.0268
0.1121  0.0279  0.0705  0.0138  0.3735  9.3392  0.0268
0.1128  0.0241  0.0819  0.0068  0.1504  9.2785  0.0302
0.1120  0.0226  0.0772  0.0122  0.2988  9.2785  0.0302
0.1128  0.0236  0.0801  0.0091  0.2256  9.2785  0.0302
0.1135  0.0248  0.0855  0.0033  0.0757  9.2785  0.0302
0.1128  0.0255  0.0824  0.0049  0.1128  9.2785  0.0302
0.0902  0.0202  0.0655  0.0045  0.1504  9.2785  0.0302
0.0752  0.0166  0.0548  0.0038  0.1504  9.2785  0.0302
0.1128  0.0133  0.0852  0.0143  0.1504  9.2785  0.0670
0.1128  0.0135  0.0909  0.0084  0.0752  9.2785  0.0670
0.0908  0.0115  0.0724  0.0068  0.0757  9.2785  0.0670
0.0752  0.0100  0.0602  0.0051  0.0752  9.2785  0.0670
0.1316  0.0159  0.1064  0.0093  0.0752  9.2785  0.0670
0.1503  0.0179  0.1219  0.0106  0.0752  9.2785  0.0670
0.1691  0.0208  0.1368  0.0115  0.0752  9.2785  0.0670
0.1135  0.0143  0.0949  0.0043  0.0378  9.2785  0.0670
0.0842  0.0058  0.0738  0.0047  0.1504  9.2782  0.0603
0.0706  0.0049  0.0594  0.0063  0.2988  9.2782  0.0603
0.0842  0.0055  0.0715  0.0073  0.3008  9.2782  0.0603
0.0842  0.0057  0.0727  0.0058  0.2256  9.2782  0.0603
0.0853  0.0054  0.0773  0.0027  0.0762  9.2782  0.0603
0.0853  0.0058  0.0765  0.0031  0.1028  9.2782  0.0603
0.1053  0.0070  0.0928  0.0056  0.1504  9.2782  0.0603
0.0636  0.0044  0.0555  0.0037  0.1514  9.2782  0.0603
0.0742  0.0052  0.0649  0.0041  0.1514  9.2782  0.0603
0.1264  0.0079  0.1116  0.0068  0.1504  9.2782  0.0603
0.1474  0.0087  0.1310  0.0077  0.1503  9.2782  0.0603
0.1684  0.0110  0.1495  0.0079  0.1503  9.2782  0.0603
0.1280  0.0078  0.1160  0.0042  0.0762  9.2782  0.0603
0.0897  0.0065  0.0758  0.0073  0.1494  9.3403  0.0670
0.0747  0.0052  0.0638  0.0057  0.1494  9.3403  0.0670
0.1098  0.0080  0.0932  0.0086  0.1494  9.3403  0.0670
0.1292  0.0096  0.1108  0.0088  0.1494  9.3403  0.0670
0.1494  0.0113  0.1285  0.0096  0.1494  9.3403  0.0670
0.1098  0.0085  0.0972  0.0042  0.0747  9.3403  0.0670
];%experimental data
%po(bar) p_cyhx(bar) p_mcpo(bar) p_mcpp(bar)...
%p_h2(bar) Vdot/RT(mol/s/bar) mol_H+
%Note: all values are multiplied by 1e5 except H2 pressure...
%for easy handling of numbers

init=[
0.1121  0.0000  0.0000
0.1128  0.0000  0.0000
```

```
0.1128  0.0000  0.0000
0.0896  0.0000  0.0000
0.1345  0.0000  0.0000
0.1579  0.0000  0.0000
0.1568  0.0000  0.0000
0.1121  0.0000  0.0000
0.1128  0.0000  0.0000
0.1121  0.0000  0.0000
0.1128  0.0000  0.0000
0.1120  0.0000  0.0000
0.1128  0.0000  0.0000
0.1135  0.0000  0.0000
0.1128  0.0000  0.0000
0.0902  0.0000  0.0000
0.0752  0.0000  0.0000
0.1128  0.0000  0.0000
0.1128  0.0000  0.0000
0.0908  0.0000  0.0000
0.0752  0.0000  0.0000
0.1316  0.0000  0.0000
0.1503  0.0000  0.0000
0.1691  0.0000  0.0000
0.1135  0.0000  0.0000
0.0000  0.0842  0.0000
0.0000  0.0706  0.0000
0.0000  0.0842  0.0000
0.0000  0.0842  0.0000
0.0000  0.0853  0.0000
0.0000  0.0853  0.0000
0.0000  0.1053  0.0000
0.0000  0.0636  0.0000
0.0000  0.0742  0.0000
0.0000  0.1264  0.0000
0.0000  0.1474  0.0000
0.0000  0.1684  0.0000
0.0000  0.1280  0.0000
0.0000  0.0897  0.0000
0.0000  0.0747  0.0000
0.0000  0.1098  0.0000
0.0000  0.1292  0.0000
0.0000  0.1494  0.0000
0.0000  0.1098  0.0000
];%initial conditions
%p_cyhx(bar) p_mcpo(bar) p_mcpp(bar)
%Note:all values are multiplied by 1e5...
%for easy handling of numbers

n=size(exp,1);%# of experimental points
```

```
sp=1;%starting set point of input data
po_exp=exp(sp:sp-1+n,1);%inlet reactant pressure
pc6o_exp=exp(sp:sp-1+n,2)./po_exp;%p1/po (cyclohexene)
pc5o_exp=exp(sp:sp-1+n,3)./po_exp;%p2/po (methylcyclopentenes)
pc5p_exp=exp(sp:sp-1+n,4)./po_exp;%p3/po (methylcyclopentane)
ph2_exp=exp(sp:sp-1+n,5);%p_h2
VRT_exp=exp(sp:sp-1+n,6);%Vdot/RT
wo=exp(sp:sp-1+n,7);%total # of H+ in bed

%normalizing the inlet pressure matrix
pin=zeros(n,3);%matrix of normalized inlet pressures
for i =1:3
pin(:,i)=init(sp:sp-1+n,i)./po_exp;%boundary condition at y=0
end
%experimental data matrix
pout_exp=[pc6o_exp pc5o_exp pc5p_exp];
%solving odes using ode45
k=[10 1 10 10];%initial guess for k_{2f}^{C6},k_{2b}^{C5},
%k_{3}^{C6},k_{3}^{C5}
dy=0.01;%step change in # of H+ in bed
y=0:dy:1;
lb=[0 0 0 0];%lower-bound for k's
options = optimoptions(@lsqcurvefit,'Algorithm',...
'trust-region-reflective','MaxFunctionEvaluations',2000,...
'FunctionTolerance',1e-20);
[kfit,Rsdnrm,Rsd,ExFlg,OptmInfo,Lmda,Jmat]=lsqcurvefit(...
@(a,b)ode_solve(a,b,y,ph2_exp,VRT_exp,wo),k,pin,pout_exp,...
lb,[],options);
conf=nlparci(kfit,Rsd,'jacobian',Jmat);%for confidence intervals
conf_int=conf(:,2)-kfit';%calculating confidence intervals
fprintf('The estimated parameters are:\n k_{2f}^{C6} = %f %s %f\n',...
kfit(1),char(177),conf_int(1));
fprintf('k_{2b}^{C5} = %f %s %f\n ',kfit(2),char(177),conf_int(2));
fprintf('k_{3}^{C6} = %f %s %f\n',kfit(3),char(177),conf_int(3));
fprintf('k_{3}^{C5} = %f %s %f\n',kfit(4),char(177),conf_int(4));
figure(1)
plot(pout_exp(:,1),p_fit(:,1),'ro',pout_exp(:,2),p_fit(:,2),'bo',...
pout_exp(:,3),p_fit(:,3),'go',[0 1],[0 1]);
set(gca,'TickDir','out','FontSize',16,'TickLength',[0.01,0.005]);
xlabel('p_{exp}/p_{o}')
ylabel('p_{sim}/p_{o}')
figure(2)
for i=1:n
plot(y,p_profile(:,1,i),'-.r',y,p_profile(:,2,i),'-b',...
y,p_profile(:,3,i),':g')
hold on
set(gca,'TickDir','out','FontSize',16,'TickLength',[0.01,0.005]);
end
```

```
xlabel('w/w_{o}')
ylabel('p_{fit}/p_{o}')
```

The two function files used by the main file as as follows.

```
function p_sim=ode_solve(k,pin,y,ph2_exp,VRT_exp,wo)
global n p_fit p_profile
p_sim=zeros(n,3);
for i=1:n
Z=pin(i,:);%boundary condition at y=0
[¬,p_bed]=ode45(@(a,b)ode_setup(a,b,k,ph2_exp,VRT_exp,wo,i),y,Z);
p_sim(i,:)=p_bed(end,:);
p_fit=p_sim;
p_profile(:,1,i)=p_bed(:,1);
p_profile(:,2,i)=p_bed(:,2);
p_profile(:,3,i)=p_bed(:,3);
end
end
```

and

```
function dpdy=ode_setup(y,p,k,ph2_exp,VRT_exp,wo,i)
dpdy=zeros(3,1);
%cyclohexene
dpdy(1)=(k(2)*p(2)-k(1)*p(1)-k(3)*p(1)*ph2_exp(i))*wo(i)/VRT_exp(i);
%methylcyclopentenes
dpdy(2)=(k(1)*p(1)-k(2)*p(2)-k(4)*p(2)*ph2_exp(i))*wo(i)/VRT_exp(i);
%methylcyclopentane
dpdy(3)=(k(3)*p(1)*ph2_exp(i)+k(4)*p(2)*ph2_exp(i))*wo(i)/VRT_exp(i);
end
```

References

(1) Olah, G. A. *Angew. Chem. Int. Ed.* **2005**, *44*, 2636–2639.
(2) Mokrani, T.; Scurrell, M. *Catal. Rev.* **2009**, *51*, 1–145.
(3) Tian, P.; Wei, Y.; Ye, M.; Liu, Z. *ACS Catal.* **2015**, *5*, 1922–1938.
(4) Newsam, J. M. *Science* **1986**, *231*, 1093–1099.
(5) Lok, B. M.; Messina, C. A.; Patton, R. L.; Gajek, R. T.; Cannan, T. R.; Flanigen, E. M. *J. Am. Chem. Soc.* **1984**, *106*, 6092–6093.
(6) Csicsery, S. M. *Zeolites* **1984**, *4*, 202–213.
(7) Moscou, L. *Stud. Surf. Sci. Catal.* **1991**, *58*, 1–12.
(8) Corma, A. *Chem. Rev.* **1995**, *95*, 559–614.
(9) Primo, A.; Garcia, H. *Chem. Soc. Rev.* **2014**, *43*, 7548–7561.
(10) Chang, C. D.; Silvestri, A. J. *J. Catal.* **1977**, *47*, 249–259.
(11) Langner, B. E. *Appl. Catal.* **1982**, *2*, 289–302.
(12) Chang, C. D. *Catal. Rev. Sci. Eng.* **1983**, *25*, 1–118.
(13) Chang, C. D. *Catal. Rev. Sci. Eng.* **1984**, *26*, 323–345.
(14) Teketel, S.; Skistad, W.; Benard, S.; Olsbye, U.; Lillerud, K. P.; Beato, P.; Svelle, S. *ACS Catal.* **2012**, *2*, 26–37.
(15) Olsbye, U.; Svelle, S.; Bjørgen, M.; Beato, P.; Janssens, T. V. W.; Joensen, F.; Bordiga, S.; Lillerud, K. P. *Angew. Chem. Int. Ed.* **2012**, *51*, 5810–5831.
(16) Bhawe, Y.; Moliner-Marin, M.; Lunn, J. D.; Liu, Y.; Malek, A.; Davis, M. *ACS Catal.* **2012**, *2*, 2490–2495.
(17) Dusselier, M.; Davis, M. E. *Chem. Rev.* **2018**, *118*, 5265–5329.
(18) Shen, Y.; Le, T. T.; Fu, D.; Schmidt, J. E.; Filez, M.; Weckhuysen, B. M.; Rimer, J. D. *ACS Catal.* **2018**, *8*, 11042–11053.
(19) Li, C.; Paris, C.; Martínez-Triguero, J.; Boronat, M.; Moliner, M.; Corma, A. *Nat. Catal.* **2018**, *1*, 547–554.
(20) Marcus, D. M.; McLachlan, K. A.; Wildman, M. A.; Ehresmann, J. O.; Kletnieks, P. W.; Haw, J. F. *Angew. Chem. Int. Ed.* **2006**, *45*, 3133–3136.
(21) Lesthaeghe, D.; Van Speybroeck, V.; Marin, G. B.; Waroquier, M. *Angew. Chem. Int. Ed.* **2006**, *45*, 1714–9.

(22) Lesthaeghe, D.; Van Speybroeck, V.; Marin, G. B.; Waroquier, M. *Ind. Eng. Chem. Res.* **2007**, *46*, 8832–8838.
(23) Haw, J. F.; Nicholas, J. B.; Song, W.; Deng, F.; Wang, Z.; Xu, T.; Heneghan, C. S. *J. Am. Chem. Soc.* **2000**, *122*, 4763–4775.
(24) Song, W.; Haw, J. F.; Nicholas, J. B.; Heneghan, C. S. *J. Am. Chem. Soc.* **2000**, *122*, 10726–10727.
(25) Song, W.; Marcus, D. M.; Fu, H.; Ehresmann, J. O.; Haw, J. F. *J. Am. Chem. Soc.* **2002**, *124*, 3844–3845.
(26) Haw, J. F.; Song, W.; Marcus, D. M.; Nicholas, J. B. *Acc. Chem. Res.* **2003**, *36*, 317–326.
(27) Olsbye, U.; Svelle, S.; Lillerud, K. P.; Wei, Z. H.; Chen, Y. Y.; Li, J. F.; Wang, J. G.; Fan, W. B. *Chem. Soc. Rev.* **2015**, *44*, 7155–7176.
(28) Chen, N.; Reagen, W. *J. Catal.* **1979**, *59*, 123–129.
(29) Ono, Y.; Mori, T. *J. Chem. Soc. Faraday Trans. 1 Phys. Chem. Condens. Phases* **1981**, *77*, 2209.
(30) Arstad, B.; Kolboe, S. *Catal. Letters* **2001**, *71*, 209–212.
(31) Bjørgen, M.; Svelle, S.; Joensen, F.; Nerlov, J.; Kolboe, S.; Bonino, F.; Palumbo, L.; Bordiga, S.; Olsbye, U. *J. Catal.* **2007**, *249*, 195–207.
(32) Bjørgen, M.; Joensen, F.; Lillerud, K.-P.; Olsbye, U.; Svelle, S. *Catal. Today* **2009**, *142*, 90–97.
(33) Ilias, S.; Bhan, A. *J. Catal.* **2012**, *290*, 186–192.
(34) Sun, X.; Müller, S.; Shi, H.; Haller, G. L.; Sanchez-Sanchez, M.; van Veen, A. C.; Lercher, J. A. *J. Catal.* **2014**, *314*, 21–31.
(35) Dai, W.; Wang, C.; Dyballa, M.; Wu, G.; Guan, N.; Li, L.; Xie, Z.; Hunger, M. *ACS Catal.* **2015**, *5*, 317–326.
(36) Hwang, A.; Prieto-Centurion, D.; Bhan, A. *J. Catal.* **2016**, *337*, 52–56.
(37) Olsbye, U.; Bjørgen, M.; Svelle, S.; Lillerud, K.-P.; Kolboe, S. *Catal. Today* **2005**, *106*, 108–111.
(38) Ilias, S.; Bhan, A. *ACS Catal.* **2013**, *3*, 18–31.
(39) Svelle, S.; Joensen, F.; Nerlov, J.; Olsbye, U.; Lillerud, K.-P.; Kolboe, S.; Bjørgen, M. *J. Am. Chem. Soc.* **2006**, *128*, 14770–14771.
(40) Svelle, S.; Olsbye, U.; Joensen, F.; Bjørgen, M. *J. Phys. Chem. C* **2007**, *111*, 17981–17984.
(41) Chang, C. D.; Chu, C. T.-W.; Socha, R. F. *J. Catal.* **1984**, *86*, 289–296.
(42) Chang, C. D.; Lang, W. H.; Smith, R. L. *J. Catal.* **1979**, *56*, 169–173.
(43) Hwang, A.; Kumar, M.; Rimer, J. D.; Bhan, A. *J. Catal.* **2017**, *346*, 154–160.
(44) Marchi, A. J.; Froment, G. F. *Appl. Catal.* **1991**, *71*, 139–152.
(45) Khare, R.; Arora, S. S.; Bhan, A. *ACS Catal.* **2016**, *6*, 2314–2331.

(46) Chen, Z.; Ni, Y.; Zhi, Y.; Wen, F.; Zhou, Z.; Wei, Y.; Zhu, W.; Liu, Z. *Angew. Chem. Int. Ed.* **2018**, *57*, 12549–12553.
(47) Khare, R.; Millar, D.; Bhan, A. *J. Catal.* **2015**, *321*, 23–31.
(48) Khare, R.; Bhan, A. *J. Catal.* **2015**, *329*, 218–228.
(49) Khare, R.; Liu, Z.; Han, Y.; Bhan, A. *J. Catal.* **2017**, *348*, 300–305.
(50) Liang, T.; Chen, J.; Qin, Z.; Li, J.; Wang, P.; Wang, S.; Wang, G.; Dong, M.; Fan, W.; Wang, J. *ACS Catal.* **2016**, *6*, 7311–7325.
(51) Li, C.; Vidal-Moya, A.; Miguel, P. J.; Dedecek, J.; Boronat, M.; Corma, A. *ACS Catal.* **2018**, *8*, 7688–7697.
(52) Schmidt, F.; Paasch, S.; Brunner, E.; Kaskel, S. *Microporous Mesoporous Mater.* **2012**, *164*, 214–221.
(53) Mei, C.; Wen, P.; Liu, Z.; Liu, H.; Wang, Y.; Yang, W.; Xie, Z.; Hua, W.; Gao, Z. *J. Catal.* **2008**, *258*, 243–249.
(54) Losch, P.; Boltz, M.; Bernardon, C.; Louis, B.; Palčić, A.; Valtchev, V. *Appl. Catal. A Gen.* **2016**, *509*, 30–37.
(55) Bij, H. E. V. D.; Weckhuysen, B. M. *Chem. Soc. Rev.* **2015**, *44*, 7406–7428.
(56) P.Magnoux; P.Roger; C.Canaff; V.Fouche; N.S.Gnep; M.Guisnet *Stud. Surf. Sci. Catal.* **1987**, *34*, 317–330.
(57) Fu, H.; Song, W.; Haw, J. F. *Catal. Letters* **2001**, *76*, 89–94.
(58) Marcus, D. M.; Song, W.; Ng, L. L.; Haw, J. F. *Langmuir* **2002**, *18*, 8386–8391.
(59) Goetze, J.; Meirer, F.; Yarulina, I.; Gascon, J.; Kapteijn, F.; Ruiz-Martínez, J.; Weckhuysen, B. M. *ACS Catal.* **2017**, *7*, 4033–4046.
(60) Müller, S.; Liu, Y.; Vishnuvarthan, M.; Sun, X.; van Veen, A. C.; Haller, G. L.; Sanchez-Sanchez, M.; Lercher, J. A. *J. Catal.* **2015**, *325*, 48–59.
(61) Müller, S.; Liu, Y.; Kirchberger, F. M.; Tonigold, M.; Sanchez-Sanchez, M.; Lercher, J. A. *J. Am. Chem. Soc.* **2016**, *138*, 15994–16003.
(62) Martinez-Espin, J. S.; De Wispelaere, K.; Westgård Erichsen, M.; Svelle, S.; Janssens, T. V.; Van Speybroeck, V.; Beato, P.; Olsbye, U. *J. Catal.* **2017**, *349*, 136–148.
(63) Martinez-Espin, J. S.; Mortén, M.; Janssens, T. V. W.; Svelle, S.; Beato, P.; Olsbye, U. *Catal. Sci. Technol.* **2017**, *6*, 2314–2331.
(64) Vora, B.; Marker, T.; Barger, P.; Nilsen, H.; Kvisle, S.; Fuglerud, T. *Stud. Surf. Sci. Catal.* **1997**, *107*, 87–98.
(65) Keil, F. J. *Microporous Mesoporous Mater.* **1999**, *29*, 49–66.
(66) Chen, J. Q.; Bozzano, A.; Glover, B.; Fuglerud, T.; Kvisle, S. *Catal. Today* **2005**, *106*, 103–107.
(67) Dahl, I. M.; Kolboe, S. *Catal. Letters* **1993**, *20*, 329–336.
(68) Dahl, I.; Kolboe, S. *J. Catal.* **1994**, *149*, 458–464.
(69) Dahl, I. M.; Kolboe, S. *J. Catal.* **1996**, *161*, 304–309.

(70) Goguen, P. W.; Xu, T.; Barich, D. H.; Skloss, T. W.; Song, W.; Wang, Z.; Nicholas, J. B.; Haw, J. F. *J. Am. Chem. Soc.* **1998**, *120*, 2650–2651.
(71) Arstad, B.; Kolboe, S. *J. Am. Chem. Soc.* **2001**, *123*, 8137–8138.
(72) Song, W.; Fu, H.; Haw, J. F. *J. Am. Chem. Soc.* **2001**, *123*, 4749–4754.
(73) Ilias, S.; Bhan, A. *J. Catal.* **2014**, *311*, 6–16.
(74) McCann, D. M.; Lesthaeghe, D.; Kletnieks, P. W.; Guenther, D. R.; Hayman, M. J.; Van Speybroeck, V.; Waroquier, M.; Haw, J. F. *Angew. Chem. Int. Ed.* **2008**, *47*, 5179–82.
(75) Lesthaeghe, D.; Van der Mynsbrugge, J.; Vandichel, M.; Waroquier, M.; Van Speybroeck, V. *ChemCatChem* **2011**, *3*, 208–212.
(76) Mole, T.; Whiteside, J.; Seddon, D. *J. Catal.* **1983**, *82*, 261–266.
(77) Dessau, R. *J. Catal.* **1986**, *99*, 111–116.
(78) Mikkelsen, Ø.; Rønning, P. O.; Kolboe, S. *Microporous Mesoporous Mater.* **2000**, *40*, 95–113.
(79) Wang, C.; Xu, J.; Qi, G.; Gong, Y.; Wang, W.; Gao, P.; Wang, Q.; Feng, N.; Liu, X.; Deng, F. *J. Catal.* **2015**, *332*, 127–137.
(80) Li, Y.; Zhang, M.; Wang, D.; Wei, F.; Wang, Y. *J. Catal.* **2014**, *311*, 281–287.
(81) Dehertog, W.; Froment, G. *Appl. Catal.* **1991**, *71*, 153–165.
(82) Pérez-Uriarte, P.; Ateka, A.; Gamero, M.; Aguayo, A. T.; Bilbao, J. *Ind. Eng. Chem. Res.* **2016**, *55*, 6569–6578.
(83) Schnabel, K.-H.; Fricke, R.; Girnus, I.; Jahn, E.; Löffler, E.; Parlitz, B.; Peuker, C. *J. Chem. Soc., Faraday Trans.* **1991**, *87*, 3569–3574.
(84) Yuen, L.-T.; Zones, S. I.; Harris, T. V.; Gallegos, E. J.; Auroux, A. *Microporous Mater.* **1994**, *2*, 105–117.
(85) Teketel, S.; Svelle, S.; Lillerud, K.-P.; Olsbye, U. *ChemCatChem* **2009**, *1*, 78–81.
(86) Sugimoto, M.; Katsuno, H.; Takatsu, K.; Kawata, N. *Zeolites* **1987**, *7*, 503–507.
(87) Prinz, D.; Riekert, L. *Appl. Catal.* **1988**, *37*, 139–154.
(88) Hutchings, G. J.; Gottschalk, F.; Hall, M. V. M.; Hunter, R. *J. Chem. Soc. Faraday Trans. 1 Phys. Chem. Condens. Phases* **1987**, *83*, 571.
(89) Dewaele, O.; Geers, V. L.; Froment, G. F.; Marin, G. B. *Chem. Eng. Sci.* **1999**, *54*, 4385–4395.
(90) Schulz, H. *Catal. Today* **2010**, *154*, 183–194.
(91) Wei, Z.; Chen, Y.-Y.; Li, J.; Guo, W.; Wang, S.; Dong, M.; Qin, Z.; Wang, J.; Jiao, H.; Fan, W. *J. Phys. Chem. C* **2016**, *120*, 6075–6087.
(92) Wei, Z.; Chen, Y.-Y.; Li, J.; Wang, P.; Jing, B.; He, Y.; Dong, M.; Jiao, H.; Qin, Z.; Wang, J.; Fan, W. *Catal. Sci. Technol.* **2016**, *6*, 5526–5533.
(93) Svelle, S.; Rønning, P. O.; Kolboe, S. *J. Catal.* **2004**, *224*, 115–123.
(94) Svelle, S.; Rønning, P. O.; Olsbye, U.; Kolboe, S. *J. Catal.* **2005**, *234*, 385–400.
(95) Hill, I. M.; Hashimi, S. A.; Bhan, A. *J. Catal.* **2012**, *285*, 115–123.

(96) Ilias, S.; Khare, R.; Malek, A.; Bhan, A. *J. Catal.* **2013**, *303*, 135–140.
(97) Vandichel, M.; Lesthaeghe, D.; der Mynsbrugge, J. V.; Waroquier, M.; Van Speybroeck, V. *J. Catal.* **2010**, *271*, 67–78.
(98) Baerlocher, C.; McCusker, L. B.; Olson, D., *Atlas of zeolite framework types*; Elsevier: Amsterdam, 2007.
(99) Arora, S. S.; Bhan, A. *J. Catal.* **2017**, *356*, 300–306.
(100) Cheng, K.; Zhou, W.; Kang, J.; He, S.; Shi, S.; Zhang, Q.; Pan, Y.; Wen, W.; Wang, Y. *Chem* **2017**, *3*, 334–347.
(101) Prins, R. *Chem. Rev.* **2012**, *112*, 2714–2738.
(102) Cheung, P.; Bhan, A.; Sunley, G. J.; Iglesia, E. *Angew. Chem. Int. Ed.* **2006**, *45*, 1617–1620.
(103) Fujimoto, K.; Shikada, T.; Omata, K.; Tominaga, H.-o. *Chem. Lett.* **1984**, *13*, 2047–2050.
(104) Cheung, P.; Bhan, A.; Sunley, G. J.; Law, D. J.; Iglesia, E. *J. Catal.* **2007**, *245*, 110–123.
(105) Gumidyala, A.; Sooknoi, T.; Crossley, S. *J. Catal.* **2016**, *340*, 76–84.
(106) Martinez-Espin, J. S.; De Wispelaere, K.; Janssens, T. V. W.; Svelle, S.; Lillerud, K. P.; Beato, P.; Van Speybroeck, V.; Olsbye, U. *ACS Catal.* **2017**, *7*, 5773–5780.
(107) Gayubo, A. G.; Aguayo, A. T.; Atutxa, A.; Aguado, R.; Olazar, M.; Bilbao, J. *Ind. Eng. Chem. Res.* **2004**, *43*, 2619–2626.
(108) Yang, L.; Yan, T.; Wang, C.; Dai, W.; Wu, G.; Hunger, M.; Fan, W.; Xie, Z.; Guan, N.; Li, L. *ACS Catal.* **2019**, *9*, 6491–6501.
(109) Salvapati, G. S.; Ramanamurty, K. V.; Janardanarao, M. *J. Mol. Catal.* **1989**, *54*, 9–30.
(110) Yilmaz, B.; Müller, U. *Top. Catal.* **2009**, *52*, 888–895.
(111) Nawaz, S.; Kvisle, S.; Lillerud, K.-P.; Stocker, M.; Øren, H. *Stud. Surf. Sci. Catal.* **1991**, *61*, 421–427.
(112) Meusinger, J.; Corma, A. *J. Catal.* **1995**, *152*, 189–197.
(113) Guisnet, M.; Magnoux, P. *Appl. Catal. A Gen.* **2001**, *212*, 83–96.
(114) Marcus, D. M.; Song, W.; Ng, L. L.; Haw, J. F. *Langmuir* **2002**, *18*, 8386–8391.
(115) Hereijgers, B. P.; Bleken, F.; Nilsen, M. H.; Svelle, S.; Lillerud, K.-P.; Bjørgen, M.; Weckhuysen, B. M.; Olsbye, U. *J. Catal.* **2009**, *264*, 77–87.
(116) Keil, F. J. *Microporous Mesoporous Mater.* **1999**, *29*, 49–66.
(117) Kanai, J.; Martens, J. A.; Jacobs, P. A. *J. Catal.* **1992**, *133*, 527–543.
(118) Senger, S.; Radom, L. *J. Am. Chem. Soc.* **2000**, *122*, 2613–2620.
(119) Zheng, A.; Liu, S.-B.; Deng, F. *Microporous Mesoporous Mater.* **2009**, *121*, 158–165.
(120) Gounder, R.; Iglesia, E. *J. Catal.* **2011**, *277*, 36–45.

(121) Wu, X.; Anthony, R. *Appl. Catal. A Gen.* **2001**, *218*, 241–250.
(122) Nishiyama, N.; Kawaguchi, M.; Hirota, Y.; Vu, D. V.; Egashira, Y.; Ueyama, K. *Appl. Catal. A Gen.* **2009**, *362*, 193–199.
(123) Chen, D.; Moljord, K.; Holmen, A. *Microporous Mesoporous Mater.* **2012**, *164*, 239–250.
(124) Zhu, Q.; Kondo, J. N.; Ohnuma, R.; Kubota, Y.; Yamaguchi, M.; Tatsumi, T. *Microporous Mesoporous Mater.* **2008**, *112*, 153–161.
(125) Salmasi, M.; Fatemi, S.; Najafabadi, A. T. *J. Ind. Eng. Chem.* **2011**, *17*, 755–761.
(126) Sedighi, M.; Ghasemi, M.; Jahangiri, A. *Korean J. Chem. Eng.* **2017**, *34*, 997–1003.
(127) Hwang, A.; Bhan, A. *ACS Catal.* **2017**, *7*, 4417–4422.
(128) Jiao, F. et al. *Science* **2016**, *351*, 1065–1068.
(129) Cheng, K.; Gu, B.; Liu, X.; Kang, J.; Zhang, Q.; Wang, Y. *Angew. Chem. Int. Ed.* **2016**, *55*, 4725–4728.
(130) Gao, P.; Li, S.; Bu, X.; Dang, S.; Liu, Z.; Wang, H.; Zhong, L.; Qiu, M.; Yang, C.; Cai, J.; Wei, W.; Sun, Y. *Nat. Chem.* **2017**, *9*, 1019–1024.
(131) Li, Z.; Wang, J.; Qu, Y.; Liu, H.; Tang, C.; Miao, S.; Feng, Z.; An, H.; Li, C. *ACS Catal.* **2017**, *7*, 8544–8548.
(132) Nieskens, D. L. S.; Ciftci, A.; Groenendijk, P. E.; Wielemaker, M. F.; Malek, A. *Ind. Eng. Chem. Res.* **2017**, *56*, 2722–2732.
(133) Calligaris, M.; Nardin, G.; Randaccio, L. *Zeolites* **1983**, *3*, 205–208.
(134) Treacy, M. M.; Higgins, J. B., *Collection of simulated XRD powder patterns for zeolites*; Elsevier: 2007, p 485.
(135) Pastore, H.; Coluccia, S.; Marchese, L. *Annu. Rev. Mater. Res.* **2005**, *35*, 351–395.
(136) Müller, D.; Jahn, E.; Fahlke, B.; Ladwig, G.; Haubenreisser, U. *Zeolites* **1985**, *5*, 53–56.
(137) Blackwell, C. S.; Patton, R. L. *J . Phys. Chem* **1988**, *92*, 3965–3970.
(138) Zibrowius, B.; Löffler, E.; Hunger, M. *Zeolites* **1992**, *12*, 167–174.
(139) Vomscheid, R.; Peltre, M. J.; Man, P. P.; Barthomeuf, D. *J. Phys. Chem.* **1994**, *98*, 9614–9618.
(140) Bates, S. A.; Delgass, W. N.; Ribeiro, F. H.; Miller, J. T.; Gounder, R. *J. Catal.* **2014**, *312*, 26–36.
(141) Goodman, K. J.; Brenna, J. T. *Anal. Chem. Anal. Chem. Anal. Chem.* **1994**, *6657*, 1294–1301.
(142) Woolery, G. L.; Kuehl, G. H.; Timken, H. C.; Chester, A. W.; Vartuli, J. C. *Zeolites* **1997**, *19*, 288–296.
(143) Gorte, R. *Catal. Letters* **1999**, *62*, 1–13.
(144) Martín, N.; Li, Z.; Martínez-Triguero, J.; Yu, J.; Moliner, M.; Corma, A. *Chem. Commun.* **2016**, *52*, 6072–6075.

(145) Liu, Y.; Kirchberger, F. M.; Müller, S.; Eder, M.; Tonigold, M.; Sanchez-Sanchez, M.; Lercher, J. A. *Nat. Commun.* **2019**, *10*, 1462.
(146) Adams, D. R.; Bhatnagar, S. P. *Synthesis* **1977**, *1977*, 661–672.
(147) Vasiliadou, E. S.; Gould, N. S.; Lobo, R. F. *ChemCatChem* **2017**, *9*, 4417–4425.
(148) Harris, J. W.; Cordon, M. J.; Di Iorio, J. R.; Vega-Vila, J. C.; Ribeiro, F. H.; Gounder, R. *J. Catal.* **2016**, *335*, 141–154.
(149) Selli, E.; Forni, L. *Microporous Mesoporous Mater.* **1999**, *31*, 129–140.
(150) Zhao, X.; Li, J.; Tian, P.; Wang, L.; Li, X.; Lin, S.; Guo, X.; Liu, Z. *ACS Catal.* **2019**, *9*, 3017–3025.
(151) Weisz, P.; Prater, C. *Adv. Catal.* **1954**, *6*, 143–196.
(152) Gounder, R.; Iglesia, E. *J. Am. Chem. Soc.* **2009**, *131*, 1958–1971.
(153) Bhan, A.; Gounder, R.; Macht, J.; Iglesia, E. *J. Catal.* **2008**, *253*, 221–224.
(154) Gounder, R.; Iglesia, E. *Acc. Chem. Res.* **2012**, *45*, 229–238.
(155) Sarazen, M. L.; Iglesia, E. *Proc. Natl. Acad. Sci. U. S. A.* **2017**, *114*, E3900–E3908.
(156) Crank, J., *The Mathematics of Diffusion*, 2nd; Oxford University Press: New York, 1979.
(157) Pérez-Pariente, J.; Sastre, E.; Fornés, V.; Martens, J. A.; Jacobs, P. A.; Corma, A. *Appl. Catal.* **1991**, *69*, 125–137.
(158) Ratnasamy, P.; Bhat, R. N.; Pokhriyal, S. K.; Hegde, S. G.; Kumar, R. *J. Catal.* **1989**, *119*, 65–70.
(159) Wang, I.; Tsai, T.-C.; Huang, S.-T. *Ind. Eng. Chem. Res* **1990**, *29*, 2005–2012.
(160) Corma, A.; Orchillés, A. V. *Microporous Mesoporous Mater.* **2000**, *35-36*, 21–30.
(161) Kruger, J. S.; Choudhary, V.; Nikolakis, V.; Vlachos, D. G. *ACS Catal.* **2013**, *3*, 1279–1291.
(162) Bezouhanova, C. P. *Appl. Catal. A Gen.* **2002**, *229*, 127–133.
(163) Bellussi, G.; Pazzuconi, G.; Perego, C.; Girotti, G.; Terzoni, G. *J. Catal.* **1995**, *157*, 227–234.
(164) Perego, C.; Ingallina, P. *Catal. Today* **2002**, *73*, 3–22.
(165) Weitkamp, J. *Solid State Ionics* **2000**, *131*, 175–188.
(166) Degnan, T. F. *Stud. Surf. Sci. Catal.* **2007**, *170*, 54–65.
(167) Yilmaz, B.; Müller, U. *Top. Catal.* **2009**, *52*, 888–895.
(168) Čejka, J.; Morris, R. E.; Nachtigall, P., *Zeolites in Catalysis: Properties and Applications*; The Royal Society of Chemistry: Croydon, 2017.
(169) Stanislaus, A.; Cooper, B. H. *Catal. Rev.-Sci. Eng.* **1994**, *36*, 75–123.
(170) Creyghton, E.; Downing, R. *J. Mol. Catal. A Chem.* **1998**, *134*, 47–61.
(171) Weitkamp, J.; Jacobs, P. A.; Martens, J. A. *Appl. Catal.* **1983**, *8*, 123–141.
(172) Liu, Y.; Guo, W.; Zhao, X. S.; Lian, J.; Dou, J.; Kooli, F. *J. Porous Mater.* **2006**, *13*, 359–364.

(173) Sano, T.; Hagiwara, H.; Okabe, K.; Okado, H.; Saito, K.; Takaya, H. *Sekiyu Gakkaishi* **1986**, *29*, 89–92.

(174) Sano, T.; Shoji, H.; Okabe, K.; Saito, K.; Hagiwara, H.; Hosoya, T.; Takaya, H. *Sekiyu Gakkaishi* **1986**, *29*, 257–261.

(175) Sano, T.; Okabe, K.; Hagiwara, H.; Takaya, H.; Shoji, H.; Matsuzaki, K. *J. Mol. Catal.* **1987**, *40*, 113–117.

(176) Gadalla, A. M.; Chan, T.; Anthony, R. G. *Int. J. Chem. Kinet.* **1983**, *15*, 759–774.

(177) Sano, T. *Sekiyu Gakkaishi* **1992**, *35*, 119–127.

(178) Meusinger, J.; Liers, J.; Mösch, A.; Rescheitilowski, W. *J. Catal.* **1994**, *148*, 30–35.

(179) Chan, B.; Radom, L. *J. Am. Chem. Soc.* **2008**, *130*, 9790–9799.

(180) Jansen, J. C.; Creyghton, E. J.; Njo, S. L.; Van Koningsveld, H.; Van Bekkum, H. *Catal. Today* **1997**, *38*, 205–212.

(181) Haw, J. F. *Phys. Chem. Chem. Phys.* **2002**, *4*, 5431–5441.

(182) Hoffman, R. *J. Chem. Phys.* **1964**, *40*, 2480–2488.

(183) Sapre, A. V.; Gates, B. C. *Ind. Eng. Chem. Process Des. Dev.* **1981**, *20*, 68–73.

(184) Moreau, C.; Geneste, P. In *Theor. Asp. Heterog. Catal.* Springer Netherlands: Dordrecht, 1990, pp 256–310.

(185) Roque-Malherbe, R.; Wendelbo, R.; Mifsud, A.; Corma, A. *J. Phys. Chem* **1995**, *99*, 14064–14071.

(186) Burgess, Donald R., J. In *NIST Chem. WebBook, NIST Stand. Ref. Database Number 69, Eds. P.J. Linstrom W.G. Mallard*, Gaithersburg.

(187) Thermocenter, G. In *NIST Chem. WebBook, NIST Stand. Ref. Database Number 69, Eds. P.J. Linstrom W.G. Mallard*, Gaithersburg.